5-7-2016

Authigenic Clay Formation and Diagenetic Reactions, Lake Magadi, Kenya

Elena L. Nikonova
Georgia State University

AUTHIGENIC CLAY FORMATION AND DIAGENETIC REACTIONS, LAKE MAGADI, KENYA

By

ELENA L. NIKONOVA

Under the Direction of W. Crawford Elliott, Ph.D.

ABSTRACT

The purpose of this study is to understand mineral diagenesis authigenic mineral and the effect of climate on mineral of Pleistocene-Holocene sediment deposits in the Southern Kenya Rift. Lake Magadi unique geologic settings are characterized by extreme alkalinity and high silica activities. The mineralogical analysis was achieved by X-Ray diffraction (XRD) and Scanning Electron Microscopy (SEM) applications. The bulk mineralogy (quartz, halite, calcite) is the same on all localities due to similar volcaniclastics compositions throughout the Kenya Rift Valley. The clay mineralogy significantly differ among the groups of sample localities. The differences reflect different tectonic settings and ambient climate regime. In humid climate at higher elevation detrital clay minerals are abundant (feldspars, phillipsite). At lower elevation like Lake Magadi, the clay fractions dominated by authigenic minerals (zeolites and silicate minerals found with zeolites). These results show the potential of clay minerals as terrestrial climate proxies.

INDEX WORDS: Clay mineralogy, Zeolites, Lake Magadi, Kenya, Trona, Silicates, Geochemistry, XRD, SEM-EDS, Magadiite, Okenite,

AUTHIGENIC CLAY FORMATION AND DIAGENETIC REACTIONS, LAKE MAGADI, KENYA

by

ELENA L NIKONOVA

A Thesis Submitted in Partial Fulfillment of the Requirements for the Degree of

Master of Science

In the College of Arts and Sciences

Georgia State University

2015

AUTHIGENIC CLAY FORMATION AND DIAGENETIC REACTIONS, LAKE MAGADI, KENYA

by

Elena L Nikonova

Committee Chair: W. Crawford Elliott

Committee: Daniel M. Deocampo

Robert B. Simmons

Electronic Version Approved:

Office of Graduate Studies

College of Arts and Sciences

Georgia State University

DEDICATION

I would like to dedicate this thesis to my extraordinary sister Anastasia and to my wonderful parents for their love and support throughout my life. I also, would like to thank my dear friends Sasha, Nazgul, and Marat for motivating me and helping to keep my dreams alive.

ACKNOWLEDGEMENTS

I would like to acknowledge Georgia State University and the department of Geoscience for supporting my studies and providing me with a teaching assistantship during my tenure at the University.

I would like to thank the Chair of the Geoscience department Dr. Deocampo for providing me with guidance and with the necessary research materials to complete my studies.

Much appreciation to my advisor, Dr. Elliott for dedicating so much time in assisting me in the chemical laboratory. I would like to thank you for your passion and around the clock support and motivation. Without you I would not be able to accomplish this study successfully. Thank you for your passing me your knowledge down to me, I have found a great understanding in clay mineralogy. Thank you for the opportunity of using XRD and SEM equipment to further my knowledge in research. Thank you for your professionalism and for your ability in understanding each students needs and finding special study method for each of us!

I would like to thank Dr. Simmons for providing me support and assistance with Scanning Electron Microscopy. You helped me understand the principle of this technique and its applications.

I would like to thank Nathan Rabideaux for assisting me running my samples through XRD. Without your deep understanding my results would not have looked so great. I very thankful for taking the time during the evenings and weekends for assisting me with

XRD research method and supporting in new ideas of non-scientific synthesis of silica based minerals.

TABLE OF CONTENTS

LIST OF TABLES

LIST OF FIGURES

1 INTRODUCTION

Lake Magadi is a saline-alkaline pan located in the Southern Kenya Rift. Its unique geologic settings are characterized by extreme alkalinity and high silica activities. Unique geologic settings in this field area are due to active volcanism and rift tectonics, as well as aridity of the climate regime in this area. Mineralogical analysis of modern sediment deposits in the Southern Kenya Rift were conducted to understand mineral diagenesis and authigenic mineral formation in this area we employed the mineralogical analysis of recent to modern sediment deposits in the South Kenya Rift, achieved by using both X-Ray diffraction (XRD) and Scanning Electron Microscopy (SEM) applications.

Previous studies were focused on geological structure and geochemistry of Lake Magadi, as well as many archeological and paleontological discoveries of the region (Eugster, 1980, Nielsen, 1999, Jones, et al., 1977). As Deocampo (2015) points out, elevated salinity and alkalinity in lake waters tends to produce magnesium-enriched phyllosilicate clays. By contrast, the same author postulates, "aluminum-rich clays reflect freshwater flushing of the watershed associated with the termination of arid paleoclimate phases." Hence, by measuring traces of magnesium and aluminum in clay samples, it is possible to deduce environmental change through time in paleolake basins. As a result of this observation, Deocampo proposed the Authigenic Clay Index of Aridity (ACACIA) as an alternative proxy in reconstructing fluctuating paleolimnology, when other mineral proxies cannot be used for reasons discussed by that author. However, in order to be successful, the ACACIA assumes direct causation between aridity and magnesium present in the clay minerals. In order to support this assumption, it is therefore necessary to assess whether or not other factors, besides aridity, influence the inclusion of formation of

magnesium silicates sufficiently enough to attribute it to climate. The remainder of this chapter provides general, geological information about Lake Magadi in order to provide context to the research question and hypothesis stated in the last section.

1.1 Geologic Settings

Lake Magadi is located in the East Africa Rift Valley in Kenya and is a prototype of an alkaline saline lake (Eugster, 1970). The sedimentation occurred within the rift due numerous volcanic and tectonic activities. In fact, the Rift Valley was formed in a narrow fault graben with trachyte lava formations (Baker, 1976). Thus, precursor of the saline lake at Magadi was the fresh water Lake Olorgonga (Baker et al., 1971). The Lake Magadi area contains Precambrian metamorphic rocks, Plio-Pliestocene fluvial, lacustrine, and volcanic sediments (Baker et al., 1971) and was formed at the elevated area, whereas the basement system of the lake consists of volcanic and metamorphic rocks and lacustrine sediments (Jones et al., 1977).

The detailed description of geology of stratigraphic units of the Rift Valley was published by Baker (Baker, 1958). He discovered that the original rocks of the basement of the Rift Valley area are schist, quartz sandstones and gneisses. After the tectonic movements and a series of basalt lavas, the composition of the basement underlying Lake Magadi significantly changed. The floor base was covered with basalt and alkali trachyte coming from the erupted lava. Clay-sized and silt-sized particles were deposited as Eolian sediments (Eugster, 1980). Active volcanoes and their faults provided hydrothermal alkaline brine circulation to the hot springs. Later, these formations were affected by alkali hot springs, high atmospheric temperature, precipitation and high level of evaporation. It

leaded to mud deposition during wet period and sodium carbonates and clay deposition occurred during the evaporative process. Thereby, a significant amount of evaporite series or trona has been accumulated in Lake Magadi sediments (Baker et al., 1971).

Baker et al., (1971) identified several beds on that area. First, the High Magadi Bed stretches through the basin of the lake. This bed was formed on the plateau trachyte lavas, chert and limestone rocks (Baker, 1976). Second, the Oloronga Bed is traced from the south part and north-east of the Lake Magadi and contains a certain amount of cherts beds (Eugster, 1980). Third, chert series bedrocks with unconformities in the beds are found in southwest part of lagoon are mainly composed from the chert rocks. Finally, Olorgesailie Lake beds are located in the northern part of Olorgesailie Mountain and were created by the volcanic ash layers (Eugster, 1980).

For the following research samples were collected from three areas: High Magadi Beds, Olorgesailie Beds, and the Kiserian area. Geological formations and climates characterized for these areas will be discussed in the study area section.

1.2 Geochemistry of East Africa Rift Valley

Lake Magadi is an active dry alkali saline lake with the highest brine concentration (specify concentration) located in Kenya in the East Africa. According to the Warren (2014), Lake Magadi, in comparison to another lakes of the Rift Valley in Africa, have the highest brine concentration (Eugster, 1980). Hydrothermal alkaline brine originated from active volcanoes. The hydrothermal fluids are moved via faults and occur at the surface as hot springs (Nielsen, 1999). Southern Kenya Rift has been known as a region of high

geodynamic activity expressed by recent volcanism, geothermal activity and high rate of seismicity (Deocampo and Jones, 2014).

According to Jones et al., (1977), the alkalinity of Lake Magadi is obtained from the hydrolysis of lavas and volcanic glass. That process produced high concentration of SiO_2, Na^+ and HCO_3^-. Over 1700 ppm of sulfate was detected in surface water of Lake Magadi due to its removal during the process of evaporation (Deocampo et al., 2002). Circulating ground water or hot springs and alteration of volcanic ash formed new unstable minerals as zeolites and zeolites associated minerals as phillipsite, clinoptolite, chabazite, magadiite, etc.

The physical process of evaporation is one of the common processes of salt formation for Lake Magadi. Annually, the area has 122 days of precipitation, where the amount of precipitation is approximately 1.06 cm per a day. Thus, the annual average precipitation level is equal to 400 mm or 40 cm (Eugster, 1980). Therefore, sodium chloride or salt precipitated from the lake waters due to extensive evaporation.

It is well known that the geochemistry of Lake Magadi is consistent with the presence of zeolites (phillipsite, erionite, clinoptolite) minerals associated with zeolites (magadiite, okenite, kenyaite), authigenic minerals, and evaporate minerals such as trona and salt. The presence of authigenic clays can be envisions by reactions of volcanic glasses and brines. Zeolites and minerals associated with zeolites mainly composed from reaction of saline alkaline brines and volcanic glass (McCarthy et al., 1998).

1.3 Study area

Before addressing the geochemical analysis, it is important to understand that the geochemistry of the Lake Magadi will correlate with the geological parameters, such as the locations of basins, elevation, trachyte flows, dips of beds, and other factors. Hence, the chemistry of minerals and spring water will be linked to geological and geographical settings. For instance, the volcanic bedrocks will produce bicarbonate and carbonate water and carbonate-based minerals (Eugster, 1980).

For the following study, twenty-one study representative samples of modern clay selected from the surface at three different locations: the Nairobi area, the Olorgesailie formation and the Magadi Trachyte area. Collected samples were examined at Georgia State University (GSU) Department of Geoscience. All of the assembled specimens were divided into three groups based on their location Table 1-1 indicates the number of samples and its brief description, and GPS coordinates of collected locations. Figure 1-1 represents a visualization of the different elevations of the collected samples collections and their ambient climate. It is also indicates the Group C (**Error! Reference source not found.**) samples location have higher amount of precipitation and vegetation. Therefore, Group C was collected on the boarder of Nairobi and the Kiserian area at an elevation of 1600 m above the sea level. Group B is on the Olorgesailie formation Oltepesi area at an elevation of 1200 m above sea level. Group A (Figure 2-1) was collected from the southern part of the Magadi Trachyte area at an elevation of approximately 600 m. These locations differ from each other in terms of elevation, structural faulting, fluviatile and lacustrine sedimentology, and geochemistry of depositions. Subsequent geochemical and geological characteristics for Group A, B and C will be described separately.

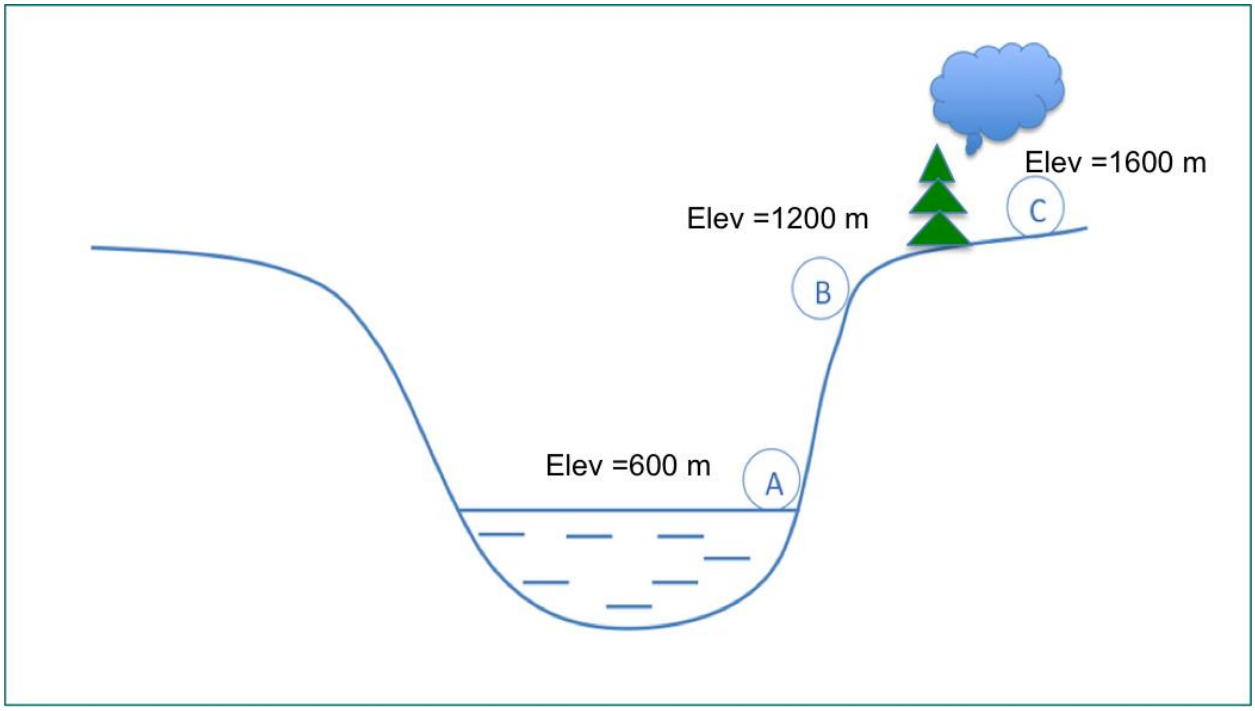

Figure 1-1. Visualization of elevation of the groups of samples. .

Table 1-1 Samples description

Group	Sample #	Sample Seaxription	GPS Coordinates
A	1	Wind Blow Sand 14 - MAG - 4	1 54' 47.76" 36°17'38.53" 680
	2	High Magadi Bed Clay Magadi - 14 - NGUN - 5	1° 58' 35.34" 36° 14' 2.85"610
	3	Saline Clay Magadi - 14 - TLB - 2	
	4	14 - MAG - 9	1° 50' 21.93" 36° 16' 15.91 "607
	5	14 - MAG - 3	1 47'21.50'' 36 16.854''612
	6	Fish Bed Clay	1° 59' 19.04" 36° 16' 9.30"610
	7	MAG - 7 - Clay Trona	1° 52' 47.85" 36° 16' 32.88"608
	8	Trona Clay (zeolite) zeolite) 14 - MAG - 6	1° 52' 45.87" 36° 16' 33.63"607
	9	MOD Colliviom Rift Scarp - NGUN - 4	1° 51' 17.87" 36° 12' 12.99"637
	10	Late Placob Debtu Fbw - CO3 cement	
	11	Key Sample 14 - MAG - 5	1°59'18.63" 36°16'09.20"609
C	12	14 - KIS - 3	1°29'53.63" 36°37'37.50"1815
	13	14 - KIS - 4	1°31'31.13" 36°36'40.50"1519
A	14	14 - NGUN - 1	1°51'17.73" 36°12'99.60"637
C	15	14 - KIS - 1	1°27'81.03" 36°39'15.30"2026
A	16	Magadite 14 - MAG - 2	1°36° 17'41.56" 36° 17'41.56"609
C	17	14 - KIS -5 (beneath lava)	1°31° '31.39" 36° 36'44.506"1551
A	18	Paleosol 14 - MAG - 3	
	19	Magadi DOP 14 - TLB - 1 Paleosol	
C	20	14 - KIS -2	1°27'28.46" 36°38'32.95"2007
B	21	Weathered Basalt Clay 14 - OLT - 1	1°33'91.46" 36°27'68.95"1014

1.3.1 Kiserian area

The eastern flanks of the Great Rift Valley were formed as a result of divergent tectonic with volcanic rocks about 2.2 Ma (Eugster, 1970). Figure 2-1 represents Kiserian area and sample collections from that area (from the right). The sedimentation is dominated by volcanic silts, carbonate deposition, and soil erosion (Dawson, 2008). Sediments and sands were formed at the contact zones or its intercalations. Weathered and fractured basalt and trachyte comprised the unconfined aquifers. McCarthy et al., (1998) observed that silica and carbonate precipitation depends on seasons. During dry periods, the salinity of ground water increases due to water evaporation. This evaporation also leads to the formation of carbonate and silica based minerals. . The evapotranspiration of silica induces from the plants' roots, but the carbonate precipitated in wetland soils (Owen et al., 2009) . During the flood cycle or precipitation period, rainwater infiltrates carbonate and silica saturated sediments. Salt precipitation will be shifted to lower elevations.

The area is located at around 1600-1800 m above the sea level and is supplied by rainfalls. Rains depositing sediments lead to high detrital sediment contents. In addition, the processes of evapotranspiration and precipitation lead to the formation of clay minerals from silicates and silt-sized alkali materials (Perchuk and Kushiro, 2013). Thus, the area is dominated by authigenic clay.

In comparison to the lower Magadi trachyte, the Kiserian area receives higher amount of annual precipitation due to its higher elevation. It was estimated by Baker (Baker, 1976) that the area consists of fresh water deposit (rains), rich minerals soil, authigenic clay and higher vegetation. For the following research five samples were collected from this area: #12, 13, 15, 17 and 20 (Figure 2-1).

1.3.2 Olorgesailie Basin

The Olorgesailie Formation was formed approximately 2.2 million years ago (Baker, 1976) and is the result of two volcanic episodes from the Olorgesailie volcano (Baker et al., 1971). The sediments consist of wetland, fluvial, and lacustrine sedimentation and formed by pedogenesis. The Olorgesailie area is characterized as basalt, sands, gravel, and volcanic silts sediments. It receives less precipitation than the Kiserian area due to its the lower altitude. Olorgesailie area was formed at an elevation of about 1000-1200 m above sea level. The soil composition shows trace of olivine basalt, carbonate and silicates, authigenic clay, and alkali trachyte, which suggest that the mineralogy of this area can be described as weathered basalt, authigenic clay or silica mineral precipitation. To determine the geochemical and mineralogical compositions of these sediments, sample #21 (Figure 2-1) was collected from this area.

1.3.3 Magadi Trachyte Area

According to Jones et al., (1977) and Baker et al., (1971), the Magadi trachyte was formed from volcanic activities about 1.4-0.7 Ma. The trachyte was developed from metamorphic rocks of Precambrian period, fluvial sediments of recent lakes and Pleistocene volcanics (Kuria et al., 2010). The lake sediments include alkali lava, silicate minerals, sodium carbonates, and volcanic ash.

The lake basin is located approximately at an elevation of 580 m above sea, thus, precipitation occurs and recharges the ground water system only two months a year: April and May. Due to the high temperature, the annual evaporation rate in the basin is very high. Most of the precipitation water is lost without reaching the ground water reservoir.

According to the Eugster (Eugster, 1980), the annual amount of trona ($(Na_2CO_3 \cdot NaHCO_3 \cdot 2H_20)$ accumulation is 0.3 cm due to the high rate of water evaporation. Thus, trona crystallization leads to the enrichment of sodium and depletion of bicarbonate in the brines (Eugster, 1970).

Sedimentology of the basin dominates by volcaniclastic minerals (chert, tuff, volcanic glass) transported during precipitation. Saline alkaline water system of Magadi characterizes as formation of sodium carbonate, cherts, zeolites, as well as zeolite-associated minerals, and authigenic clay (Jones et al., 1977). Thus, the major minerals on the basin are the interaction product of groundwater reservoir (brine dominates), particularly, alkali lava are alkali-rich and alkali-earth poor minerals. Consequently, the vegetation is limited at this area (Nielsen, 1999).

According to Eugster, 1970, the dissolved solids concentration of Lake Magadi varies from 35 to 100 mol/l based on 100 mol/l for the most concentrated springs. Thus, the northern part of Magadi is very concentrated (85-90 mol/l) with a high temperature 67-85°C. Table 1-2 indicates approximate environment conditions for each sample collected in the lower basins of Lake Magadi. This data will be used for geochemistry investigation. For the following research five samples were collected from this area: # 1-11, 14, 16, 18 and 19 (**Error! Reference source not found.**).

Table 1-2 Spring water concentration (mol/l) and temperature (° C)

Samples #	Temperature	Spring Concentration
5	81-82	90
4	50	50
7, 8	36	50
1	35	45
6,11	37	26
2	43	70
9,14	45	68
16	34	35

1.3.4 Study Purpose and Hypothesis

The following research is the derivative of research of Dr. Deocampo and the part of ACACIA (Authigenic Clay Index of Aridity) investigation. Previous studies of the Pleistocene paleoclimate in Lake Magadi in the East Africa Rift Valley focused on the correlation of paleohydrology basin and global climate change (Baker, 1958). Furthermore, Russell & Cohen, 2012 states that climate evolution of the South Kenya provided new insights of rainfall dynamics. However, the conclusion cannot be established due to the limited terrestrial records. Thus, ACACIA development will help to fill the gaps of the paleoenvironmental records of the South Kenya.

To support the research of Dr. Deocampo and ACACIA, geochemical and mineralogical analyses will be implemented to understand the evolution of basin and brine geochemistry of Lake Magadi and the associated climatic and tectonic regime for the region. The authigenic silicates or most abundant minerals in samples will be studied to understand how they were formed in relative to the climates and hydro-geochemical processes in the three regions studied. . Particularly in this study, I will focus on authigenic

formation and diagenetic reactions in East African Rift Valley in Kenya and especially at Magadi Basin. The first and the main hypothesis of that research is to investigate whether or not the authigenic mineralization increases with lower elevation and more arid climate regime. This hypothesis will be tested by geochemical and mineralogical analysis.

1.4 Methods

To provide a full geochemical and mineralogical study of authigenic and detrital clay minerals, several chemical analyses will be implemented. To prepare materials for the mineralogical study, samples were dried, labeled and separated for the archived materials and research specimens. X-Ray diffraction (XRD) bulk analysis or whole rock analysis was required for identification of chemical and structural characteristics of clay-based minerals present in clay-based rocks (Środoń, 2013). Bulk patterns indicated whether or not clay-sized materials are present on the samples. The clay-sized samples would be selected for further chemical analysis. Clay-based samples were prepared for XRD – clay analysis. Clay-based samples were prepared for XRD by Jackson's treatment to remove cementing minerals.

Jackson's treatment included several operations. To remove the cementing agent, first carbonate treatment will be implemented. To complete clay dispersion, the organic treatment 30% H_2O_2) was used. Finally, samples were treated for removal of crystalline Fe_2O_3 (iron oxide) and amorphous coating of Fe_2O_3 (Jackson, 1979).

Samples were prepared for XRD clay-based analysis to obtain a clear signal for the identification of clay minerals (Hradil et al,. 1950). The intensity and shapes of peaks, and diffraction patterns will be used to identify the individual clay minerals (Moore &

Reynolds, 1997). If required, the SEM (scanning electron microscopy) test was applied for producing electron images and chemical elements analysis of the researched material.

1.5 Expected results

The testing of the hypothesis will provide the correlation of authigenic mineralization and climate regime in East Africa Rift Valley. Accordingly, it was expected that the samples of Kiserian area with the highest (for this research) elevation (Group C) would consists of more volcanic reach soils, more alkali–earth minerals (calcium, magnesium), and more basalts due to the high amount of precipitation and vegetation. Weathered basalt clay was expected to be dominated in the regions of Olorgesailie formation. However, it was possible to state that the Olorgesailie area and Kiserian formation might have the same geochemical composition due to their location in the Nairobi area. The lower part of the Magadi trachyte consists of salt, alkali-riched minerals (salts, carbonates, sulfates) and consists of low amounts of alkali-earth elements. Authigenic clay, detrital silicates, as well as saline minerals, sodium silicates, zeolites and zeolites-associated minerals were expected to be found in the samples due to the high salinity, high springs, and pH.

2 METHODS

2.1 Sample Collection

Soil samples were collected by Dr. Deocampo and his colleagues, during the dry season in June and July 2014 by trowel and stored in clean polyethylene bags. The multiple samples were collected from select at a location in west part of the lake Magadi (S 01° E, 36°). Figure 2-1 shows the location of the mines. Samples were collected on July 24-26, 2014. The profile was derived by Deocampo and his field party. Out of collected samples, twenty-one specimens were selected for this research. Table 2-1 represents the description and the GPS coordinates of sample collection locations. For the description of research, only numbers of the samples were used. Samples were collected in four different locations selected to provide a broad range of sample diversity in terms of climate and mineral provenance.

The first station (Group A at S1° 47’ 27.38 “; E36° 54’ 81.53” ± 3 min) was a shallow area of the lake with hot springs. Microbial mats were sampled near the hot springs and significant evaporation. Mud was collected from where the lake had receded. The second station (Group B at S01° 33.914 min) was a central volcano or basalt area and sediments were sampled. The third station (Group C at S01° 27.914 min; E36° 29.068) sediments were collected from the flanks of the Kiserian area. The location and the description for each sample are in the Table 2-1.

Table 2-1: Sample location and description

Sample #	Description	Coordinates	
		Latitude	Longitude
1	Wind Blow Sand 14 - MAG - 4	S 01 54’ 47.76”	E 36˚17’38.53”680
2	High Magadi Bed Clay Magadi - 14 - NGUN - 5	S 01˚ 58’ 35.34”	E 36˚ 14’ 2.85” 610
3	Saline Clay Magadi - 14 - TLB - 2		
4	14 - MAG - 9	S 1˚ 50’ 21.93”	E 36˚ 16’ 15.91 “607
5	14 - MAG - 3	S 01 47.215"	E 36' 16.854'' 612
6	Fish Bed Clay	S 01˚ 59’ 19.04”	E 36˚ 16’ 9.30”610
7	MAG - 7 - Clay Trona	S 01˚ 52’ 47.85”	E 36˚ 16’ 32.88”607
8	Trona Clay (zeolite) zeolite) 14 - MAG – 6	S 01˚ 52’ 45.87”	E 36˚ 16’ 33.63”607
9	MOD Colliviom Rift Scarp - NGUN - 4	S 01˚ 51.177"	E 36 12.996" 637
10	Late Placob Debtu Fbw - CO_3 cement	S 01 51.177"	E 36 12.996
11	Key Sample 14 - MAG - 5	S 01˚59’18.63”	36˚16’09.20” 609
12	14 - KIS - 3	S 01 29.536"	E 36 37.375 1815
13	14 - KIS - 4	S 01 31.310"	E 36 36.400 1519
14	14 - NGUN - 1	S 01 31.310"	E 36 12.996 637
15	14 - KIS - 1	S 01 27.810"	E 36 39.153 2026
16	Magadite 14 - MAG - 2	S 01˚54’45.46”	36˚ 17’41. 56”609
17	14 - KIS -5 (beneath lava)	S 01 31.398"	E 36 36.440 1511
18	Paleosol 14 - MAG - 3	S 01 47.215"	E 36' 16.854'' 612
19	Magadi DOP 14 - TLB - 1 Paleosol		
20	14 - KIS -2	S 01˚27’28.46”	E 36˚38’32.95”2007
21	Weathered Basalt Clay 14 - OLT - 1	S 01 33.914"	E 036 27.068 1014

ArcGIS program was used to create the topographic map of samples site locations Figure 2-1.

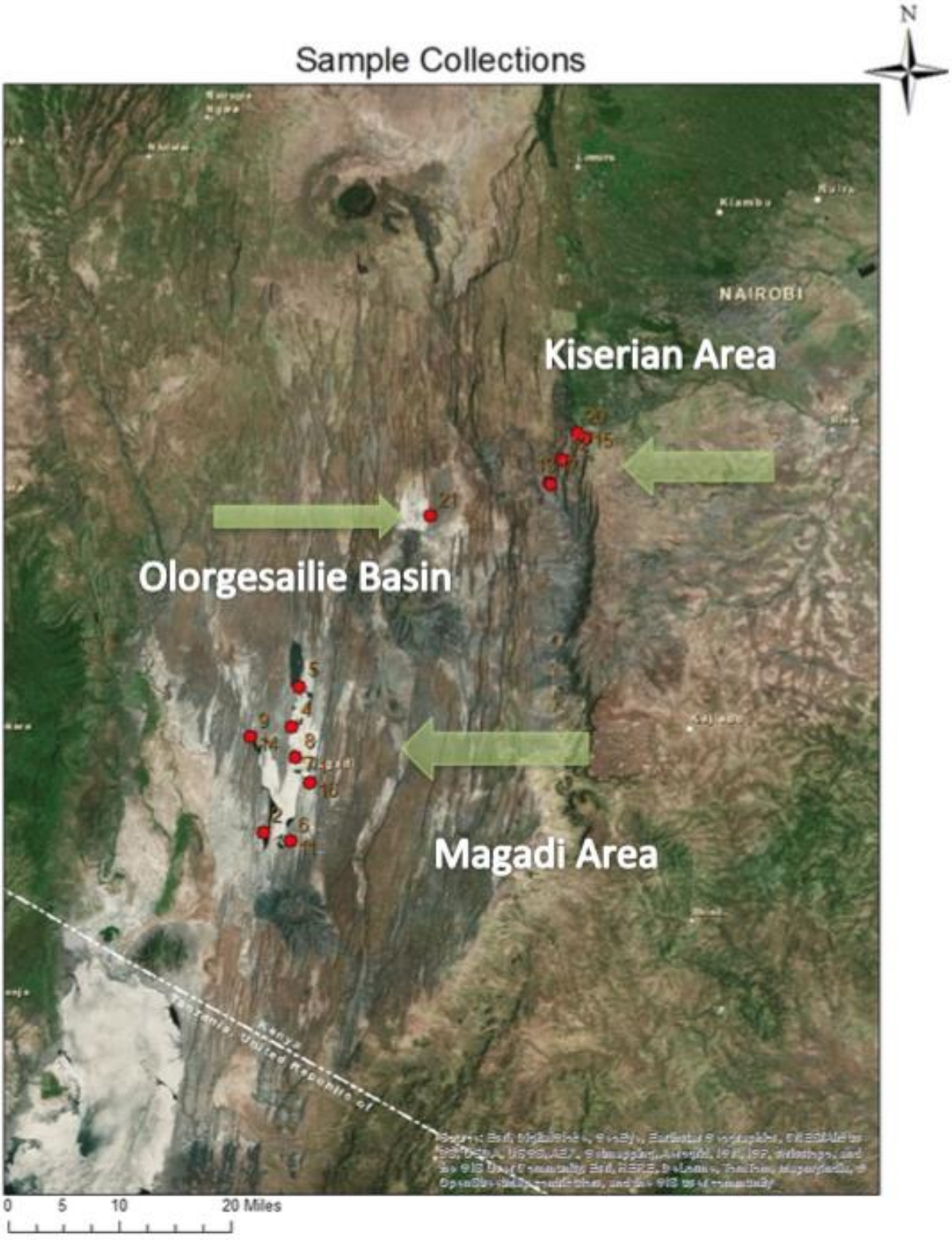

Figure 2-1 Lake Magadi sample locations

2.2 Sample Preparation

To remove moisture from the material, collected samples were dried in the oven overnight at 50°C for 24 hours. Some samples (#6, 8, 12, 16,17, and 21;) required drying for 72 hours. Dry specimens were divided into two equal amounts with a 0.25-inch sample splitter. Half of each portion was archived and another half was split into two more parts for further chemical analysis and investigation. Archived samples were labeled and stored in the Clay Laboratory, Department of Geoscience, (KH 310).

For the whole rock mineral determination, further preparation of the soil samples consisted of powdering and homogenization. To achieve the analytical acceptable particle grain size, an Impact Ball Pestle Impact Mill (Figure 2-2) was used. Approximately 25 g of sample was placed into the ceramic casket with a stainless steel ball for approximately 7 minutes to achieve homogeneity (Mahadi & Palaniandy, 2010). The powder was labeled and stored in small glass tubes. The ceramic casket was cleaned using deionized water and after rinsed in alcohol.

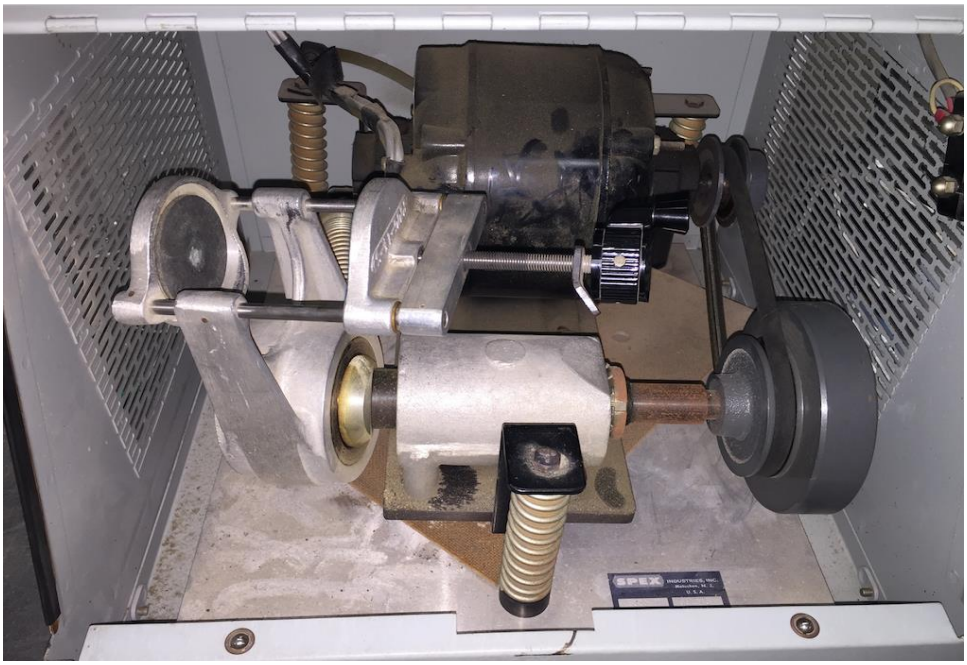

Figure 2-2 Impact Ball Pestle Impact Mill

2.2.1 Preparation for the clay analysis by using Jackson's method

To disperse the colloids of mineral soils the method of segregation of clay, silt, and sand particles was applied. Jackson's method permits separation of different series of minerals into three fraction sizes (Glenn et al., 1960) and removal of flocculents from the specimens. The Jackson's method includes three basic steps to permit disaggregation of the aluminosilicate mineral fractions from sediments and soils (Jackson, 1979): removal of carbonate cements; the removal of organic matter, and; removal of iron oxide cements. Carbonate cement removal (i.e. carbonate treatment) was used to remove carbonates and gypsum from the research material. To remove Mg and Ca carbonates and to provide effective soil dispersion, the samples were washed with 1 N sodium acetate (NaOAc) of pH 5 at 50^{o} C (acid in reaction) (Jackson, 1979)The suspension was then centrifuged for 7

minutes at 1100 rpm to settle the insoluble clay. The centrifugation was repeated with fresh buffer and centrifuged until the supernatant liquid was cleared (Jackson, 1979).

Following carbonate removal, to complete clay dispersion, the soils were treated to remove organic matter. As a result of the carbonate removal, the slight increase of pH level of the supernatant after centrifugation was noted. The increased pH is thought to be due to the presence of dissolved calcium salts. These salts retard the soil organic matter oxidation (Jackson, 1979). The organic matter removal was implemented by adding 10 ml volumes of 30% hydrogen peroxide, H_2O_2 first at room temperature then heated at 50 ^oC. (Follett, 1965). During this process, the reaction between 30% of H_2O_2 and the soil/sediment occurred. The mixture was observed closely for 5-10 minutes to prevent foaming over and, then, placed into a 50°C water bath for 4 hours for complete organic matter decomposition (Jackson, 1979). To insure complete removal of organic matter and colloidal fractions, the process was repeated three times for each sample. For complete analysis, the soil was washed with absolute methanol (CH_3OH) and centrifuged (Iannicelli-Zubiani et al., n.d.).

The iron (III) oxide (Fe_2O_3) treatment was necessary for the removal of the crystalline iron (III) oxide and amorphous iron oxide coating from the samples. In other words, during this treatment, successful separation of colloidal aluminosilicate can now occur (Jackson, 1979) and clean aluminosilicate appears, which is necessary for the X-Ray diffraction procedure. To remove iron oxide, the samples were treated with 0.3M Na-citrate ($Na_3C_6H_5O_7$) and 1M Na-bicarbonate ($NaHCO_3$) and heated in a water bath at 50°C for 15 minutes. One gram of sodium dithionite (sodium hyposulfite) was added to the mixture and the specimen was stirred vigorously for 60 seconds and heated for four more minutes. The process was repeated three more times until the red or brown color disappeared. The

solution was then centrifuged twice using sodium acetate-acetic acid buffer and once with 2-3 ml of absolute methanol (CH_3OH).

The timed settling - decantation method (Jackson 1979) was used for the separation of sand, silt and clay separation with the sizes of >50 , 20 -50 μm and <2 μm respectively. The calculation was based on the height of the sample suspension in the 500-ml such as every 10 cm of specimen in the samples is equal to 8 hours of waiting time. Another words, sample should stayed undisturbed for 8 hours for each 10 cm to obtain the < 2 μm fraction. Table 2-2 provides the calculation for each sample to be undisturbed.

Using the pipette method, the clay fraction of size <2 μm was collected from the beaker. After collection, the clay was placed on a microscopic slide and dried at room temperature for 24 hours. This method aligns the clay particle surface perpendicularly with c-axis of the phyllosilicate crystals (Jackson, 1974).

Table 2-2 Sample Preparation

Sample, N	Height, cm	Time, h
6	5	6.25
7	5	6.25
8	4.5	5.62
10	5	6.25
11	5	6.25
14	4.5	5.62
15	5	5
16	4.6	4.6
17	4.8	4.8
18	4.7	5.88
21	5	6.25

2.2.2 Preparation for clay analysis by using physical treatment

The second independent clay mineral separation method for X-Ray diffraction

oriented mount was performed by physical treatment. For physical slide preparation, an ultrasonic probe was used for dispersion. According to Ashman, et al (2009), ultrasound vibration can separate different size of particles and the size fractions obtained by this method can be used for further chemical and physical analysis without prior chemical treatments. To prepare samples, 20 g of powdered specimen was initially placed inside a beaker and 40 ml of distilled water was added (Firoozi et al., 2015) . The beaker was placed on a vibrational stable surface in the ultrasonic bath (**Figure 2-3**) to disaggregate the soil for 80 to 120 seconds (Fristensky and Grismer, 2008).

An ultrasonic processor (Sonics Inc.) with resonance frequency of 20 kHz was used for this method. After the ultrasound treatment, samples were washed in a 50-ml plastic bottle using by centrifuge (Mikhail, 1978) at 8400 rpm for 1 hour. After centrifugation, a thin layer believed to be the clay layer (< 2 μm) is observed at the top of the centrifuged sediment. An upper layer <2-μm of the clay grout was transferred mechanically using a small spatula or knife from the beaker to a microscope slide for oriented mounting for XRD analysis.

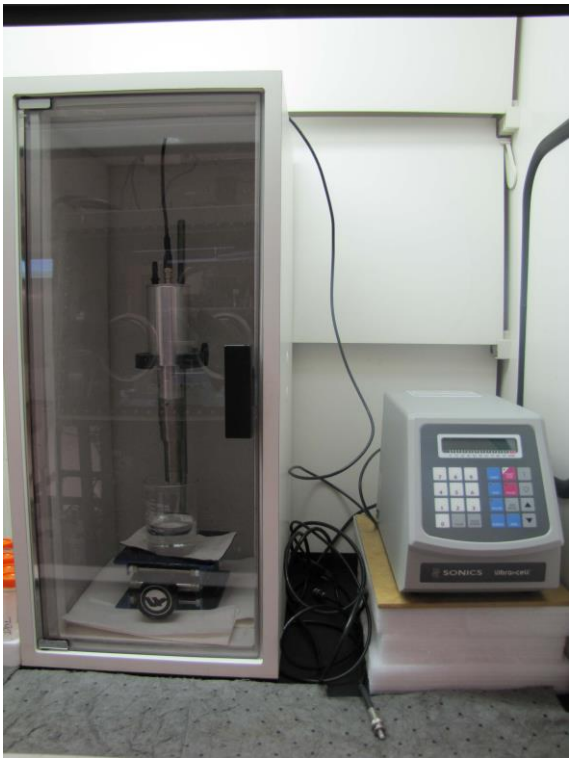

Figure 2-3 Ultrasonic Processor (GLENN et al. 1960)

2.3 X-Ray diffraction Bulk analysis

The Panalytical XRD diffraction data were scanned from 2-32 ° 2θ intervals, counting for 0.02° 2θ, and 1°2θ/min scanning speed (**Figure 2-5**). Oriented mounts were produced following the methods of Moore and Reynolds (1997). Bulk powers were loaded into circular sample holders to produce random oriented mounts (Figure 2-4). To filter $CuK_{ß}$ radiation, a graphite monochromator or Ni filter was used. Twenty-one bulk powder samples were prepared for this analysis by placing the samples powders into the circular sample holders using a scratched glass to keep grains undirected. These random mounts were examined using 5-70° scan angle range for 30 minutes under the room conditions. The diffraction patterns oriented mount for each sample was analyzed by HighScore Plus software of the X-Pert Panaltyical XRD whose error is estimated conservatively at 10%.

The sample patterns were interpreted with identification database ICDD (Moore & Reynolds, 1997).

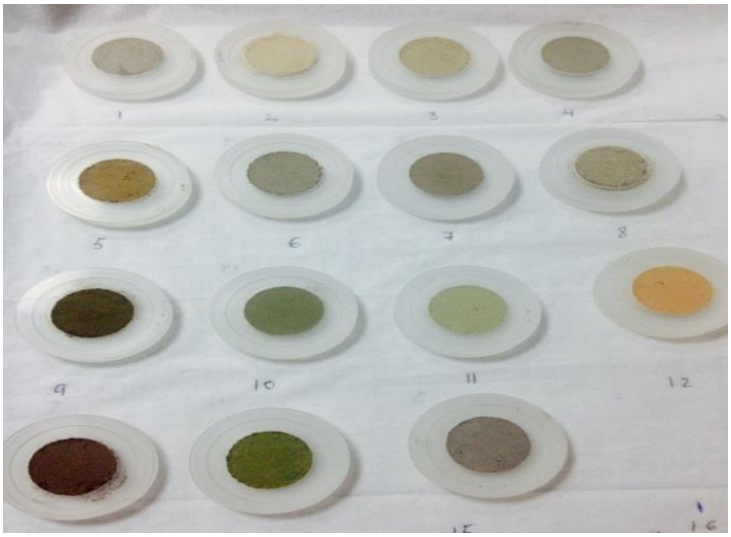

Figure 2-4 XRD Sample preparations for Bulk Analysis

2.4 X-Ray diffraction of the clay fractions

After the detailed analysis of the bulk fractions by XRD was analyzed, twelve samples were selected for clay analysis based on present of illite, smectite, and kaolinite seen in the analyses of the bulk samples. These minerals were identified using their 001 reflection. Test material was prepared by two methods: chemical treatment and physical treatment described in previous sections. Approximately 2 ml of the test material <2 μm specimen was extracted from the sample and placed into the petrographic (23 by 46 mm) glass slide using a pipette. The slides were left to dry at the room temperature overnight. After the samples were dried, the slides were analyzed on XRD from 3-32°, 2θ. Five slides were selected for 24 hours for ethylene glycol solvation to verify swelling clays within the test specimen, based on the presence of smectite in the air-dried patterns (Moore and Reynolds, 1997).

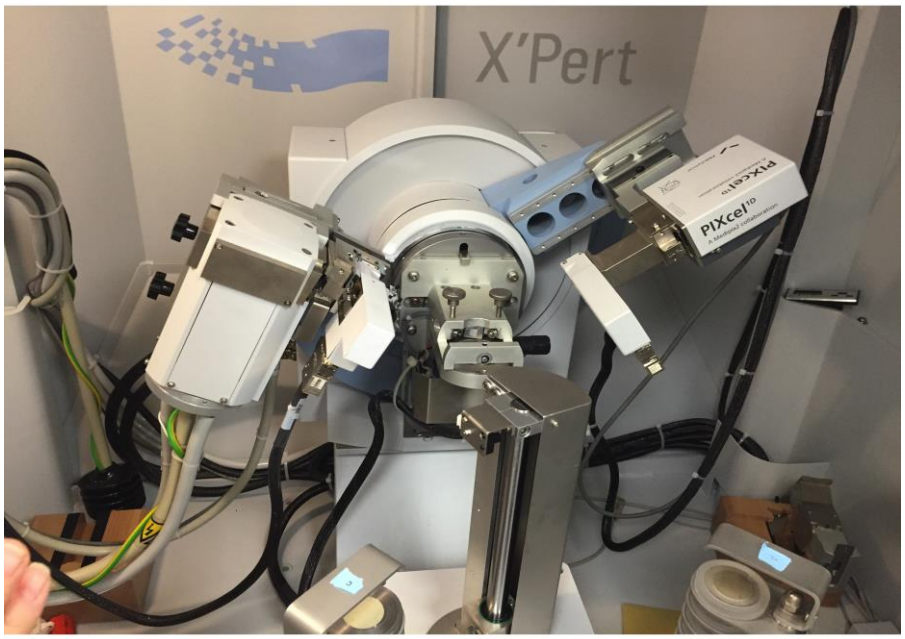

Figure 2-5 XRD PANalytical X'Pert PRO XRD

As the desirable results hadn't been achieved by Jackson's sample preparation method, the ultrasonic treatment on clay had been implemented. After the centrifugation of the samples, a thin upper level of the clay <0.25 µm to <1 µm grout was collected and placed onto petrographic glass slide and dried at room temperature for 24 hours (Firoozi, 2015). No notable mineralogical difference could be observed between 0.1 µm and 1 µm size fraction in this study. All the 12 air-dried and ethylene glycol-treated samples were analyzed at 3-32°, 2θ 30 minutes scan.

X-ray diffractometry for mineral identification is based on having a constant wavelength of radiation interacting with the unknown samples. At GSU, the X'pert Pro XRD uses a Bragg-Brentano geometry. Whereas, λ is the wavelength of the incident ray, θ is the angle between the incident rays and the surface of the crystal of the test material, d is the spacing between layers of atoms and the test material. The results can be calculated by

knowing the spacing between layers of atoms, d, for each diffracted peak and the angle between the incident rays and the surface of the crystal, θ using Bragg's Law. The d-spacing for each peak measured in Å. A summary of the methodology and theoretical development can be found in Moore and Reynolds (1989). Another words, the Bragg's Law described as: $n\lambda = 2d\sin\theta$, where d is d-spacing value in angstroms, λ is the wavelength of incident and diffracted radiation, θ is the angle between the sample mount and incident radiation.

The X-Ray are produced by heating a tungsten cathode using a >15 Ma current. These thermionic electrons are accelerated into a Cu anode at - 45 kV relative to the cathode. The collision of the thermionic electrons and the Cu block produces both white radiation and characteristic radiation. The latter is used in X-ray diffractometry. The characteristic X-Rays emitted from the Cu target in the X-ray generating tube strikes the sample at an angle θ. When diffraction occurs, the diffracted beam is emitted from the sample at an angle of 2θ relative to the incident beam. The results generated a distinctive peak for identification of the mineralogy for each sample.

2.4.1 Data Analysis using Principal Component Analysis

To analyze the data, PCO (Principal Component Analysis) and MATLAB were implemented. To find the correlation between geographical location (latitude, longitude) and mineral chemical composition MATLAB software was applied. MATLAB will generate and represent a scatter plot where each dot represents the specific sample point. This type of plot is useful to quickly visualize any correlations that may exist in the data (Ballabio, 2015). Correlation signifies that the setting of one variable has an influence on

the value of the other. Typically, one would employ principal component analysis to identify important correlations; however, the scarce amount of samples available would have been insufficient to yield a good estimator of the covariance matrix, which is required by PCA (Anjam and Valdman, 2015). Instead, it was decided to plot a line through the data using a least squares fit. This provides a visual reference to assess the amount of scatter. Hence, if a relationship exists between the quantities listed on the axes, the dots will exhibit a non-random pattern.

Cluster Analysis was used to find the correlation of scans and to distinguish difference in mineral composition. The comparison of peak and positions will be combined into clusters in a 3D model (Milcius et al., 2015). The relationships were determined automatically using HighScore Plus software.

2.4.2 The error of XRD and XRD HighScore Software measurements

The error from XRD and XRD HighScore measurements calculated from the summation of individual errors. These errors associated with HighScore Software include with peak searching and analysis, background determination, outlier correlation. The systematic errors associated with equipment involved equipment calibration, samples sensitivity, sample displacement, peak asymmetry, angular errors. It was estimated that the error is approximately $\approx 10\ \%$.

2.5 Scanning Electron Microscopy SEM –EDS

SEM produces electron images and elemental mapping. Figure 1 shows the seven primary components of an SEM (Figure 2.5): beam generation, beam manipulation, beam

interaction, signal processing, detection, vacuum, and display and record. The components of the SEM work together to ascertain the characteristics of the micrograph image, such as resolution and magnification.

The vacuum system is an essential SEM component, which initiated before any other function. The vacuum system creates a mean-free path for electrons, prevents high voltage discharge between the filament and the anode, prevents O_2 sensitive filament oxidation, and safe guards against contaminating gases from water vapor and organics (Simmons, 2013). The SEM's three stage condenser lens system is also a very important aspect of the electron beam increasing the resolution and lower the signal, the beam travels through condenser lens C2 further refining the beam spot, and then the beam goes through condenser lens C3 with controls the final focusing of the image on the viewing system as well as the depth of the focus (Russell, 1999). After the electron beam travelling at approximately 20 kV penetrates the specimen, both elastically and inelastic scattering of electrons occurs (Figure 2-6). Elastical scattering (backscattering electrons) is increased with increasing atomic weight of elements in the sample and is collected by the backscatter electron detector to reduce noise. Inelastical scattered electrons are attached through a Faraday cage and then collected by the secondary electron detector converting the electronic signal into an image on a computer monitor (Reimer, 1984).

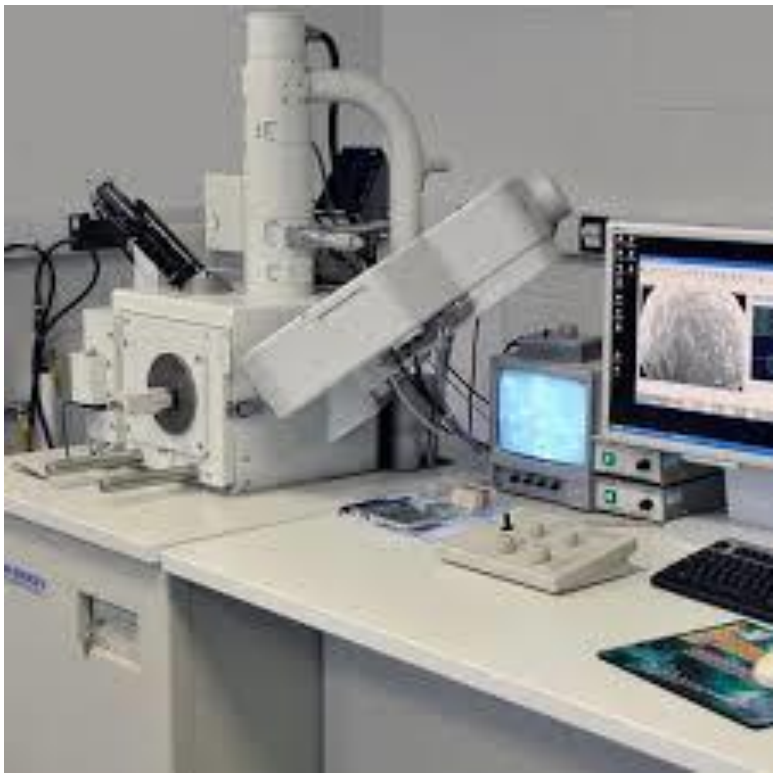

Figure 2-6 Scanning Electronic Microscope

The EDS functions of the SEM use X-Rays to provide a quantitative analysis. The electron beam (Figure 2-7) is directed to a targeted area particle on the specimen stage generating energy specific X-Ray energy, which is absorbed by a silicon crystal capable of detecting multiple wavelengths simultaneously.

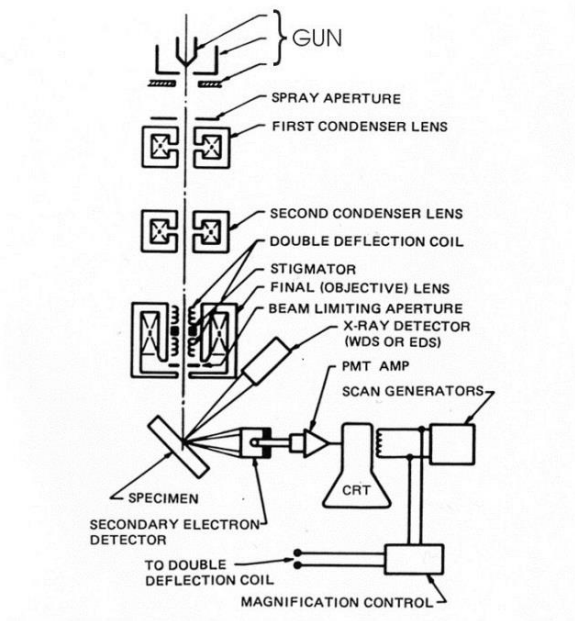

Figure 2-7 Scanning Electronic Microscope

2.5.1 SEM Samples preparation

To prepare the specimen for analysis, a grain of material approximately 5mm in diameter was mounted on double-sided carbon tape, and affixed to a metal specimen mount. The mount and sample were then placed in the vacuum evaporation system (VES), and the VES was depressurized to create a high vacuum. An electrical current was passed through a rod of graphite positioned between two conductors, vaporizing the graphite at the atomic level and causing it to adhere to the sample. This process, known as thermal deposition, increases the thermal and electrical conductivity of the sample by coating the sample in a thin layer of carbon. This electroconductive carbon layer allowed the specimen to be viewed using an electron optical system. The coated specimens were then placed on the viewing stage of the SEM, and sealed inside the vacuum chamber (Uchic et al., 2006)

2.6 Preliminary Dehydration – Rehydration Study of Na-silicate minerals

In an attempt to synthesize okenite from precursor sodium silicate mineral, we reacted dehydrated magadiite with a chalk ($CaCO_3$) and Magadi type brine solution. The solution was place into oven at 50° C for 72 hours. Another sample was prepared by adding a Calcium hydroxide saturated solution to dehydrated magadiite and left at standard room temperature and humidity for 72 hours. SEM analysis was conducted on dehydrated magadiite and the synthesized samples to identify associated mineral diagenesis seen in nature. The concentrations of solutions were not calculated. Thus, the experiment was preliminary in scope and was simply to gage whether Ca-saturated brines interacting with magadiite can produce okenite.

3 RESULTS

3.1 XRD Bulk Analysis Results

XRD bulk analysis was used to determine the complete mineralogical composition of 21 samples. These data enable the selection of samples for further XRD - clay analysis and SEM scanning.

In the first place, minerals were recognized by using the diffraction data and methods of mineral identification methods per Moore & Reynolds (1997). The method involves the identification of peaks intensity and positions at the angle of 45° 2θ or less and calculating the d-spacing per Bragg's law (Hradil et al., 1950). The determined peak values were compared with the minerals and their known diffraction characteristics.

According to the whole rock analysis using the identification tables in Moore and Reynolds (1997), the most abundant minerals in these samples by inspection of the

diffraction peaks were: quartz, calcite, illite/smectite, halite and zeolites from XRD data using powder diffraction data and by matching peaks of the observed data to known diffraction data for minerals (Moore & Reynolds, 1997). K-Feldspar, trona, magnesium calcite, kaolinite/chlorite were found in less abundance in a fewer number of samples (Moore & Reynolds, 1997). Diffraction peaks that were consistent for the following minerals were observed: for gypsum, magnesium oxide, albite, perovskite, montmorillonite, pyrochlore, plagioclase, anorthoclase, sepiolite, magadiite and portlandite were found in a fewer number of samples. The distinct diffraction peaks of calcite were detected at 3.86 Å, 3.03 Å, 1.60 Å. Diffraction peaks corresponding to quartz were discovered at 3.34 Å, 2.28 Å, 2.12 Å and 2.05 Å. The diffraction peaks belonging to mixed layer Illite/Smectite were observed at 5.61 Å, 8.58 Å, 11.16 Å, and 15.80 Å. Smectite diffraction peaks were seen at 15.51 Å, 10.4Å, and 11.20 Å.

Table 3-1 XRD bulk analysis (Moore-Reynolds)

Sample #	Quartz	Calcite	Halite	S-Feldspar	K-Feldspar	Zeolite	Magnesium Calcite	Albite	Perovskite	Trona	Kaolinite /chlorite	Illite	Smectite	Iron (III) Oxide	Anortho clase
1	✔	✔	✔	✔	✔		✔	✔			✔				
2	✔		✔	✔		✔		✔	✔	✔					
3		✔			✔	✔	✔								
4	✔	✔	✔		✔					✔	✔				
5	✔		✔		✔	✔		✔			✔				
6	✔	✔			✔	✔						✔	✔		
7	✔	✔	✔		✔					✔	✔	✔			
8	✔	✔			✔					✔	✔	✔			
9	✔				✔						✔				
10	✔				✔						✔		✔		
11		✔	✔	✔	✔	✔									✔
12	✔				✔						✔				
13	✔	✔			✔						✔				
14	✔				✔						✔				✔
15	✔	✔			✔								✔	✔	
16	✔	✔	✔		✔	✔						✔	✔		
17	✔				✔		✔				✔				
18						✔					✔	✔	✔		
19	✔										✔	✔	✔		
20	✔					✔									
21					✔										

To verify these results, all specimens were selected for detailed clay mineral identification and quantification on a bulk rock basis using the XRD HighScore Plus

Software. The software also provided the percentage of minerals in each sample or Principal Component Analysis (PCA). According to the quantitative XRD analyses using High Score Plus Software, most of the samples consist, in general, of phyllosilicate minerals, zeolites, zeolite-associated minerals, silicate minerals (albite, quartz), trona, and halite (NaCl). The phyllosilicate clay minerals found are: kaolinite/chlorite, illite, and montmorillonite. Silicate minerals, such as quartz, sanidine, albite, anorthoclase, were detected in most of the samples. Besides this, calcite was one of the most common minerals. Magadiite, a mineral found frequently at Lake Magadi, was discovered in two samples: #16 and #21. Magadiite was identified based on the observed diffraction peaks at 7.25 Å and 15.69 Å. The XRD results demonstrate that the most common investigated zeolites in these samples are phillipsite, clinoptolite, mordenite, chabazite. According to the results of bulk analysis, twelve samples with clay content were selected for further clay analysis. These samples: # 1, 2, 3, 5, 6, 7, 8, 10, 11, 12, 14, 15, 16, 17, 18, and 21. Table 3-2 shows the summary of the observed minerals on the bulk analysis; check mark indicates the presence of the mineral on the whole rock analysis.

Using HighScore, the most abundant minerals (occurring 8 or more times in these 21 samples) are sanidine, low quartz, high albite, anorthoclase and erionite. XRD analysis indicates high albite as albite which stable at very high temperatures above 800°C (Guo et al., 2015). Furthermore, HighScore was able to discriminate and quantify two kind of quartz (low and high quartz). The less abundant minerals were detected in 4-7 samples are phillipsite, calcite, halite, and trona. The least common minerals found only in one or two research samples are zeolites (mordenite, phillipsite, chabazite); kaolinite, illite, montmorillonite, magnesium calcite, analcime, and magadiite. Table 3-2 represents the

summarizing quantitative XRD analysis. Each sample represents as 100% of different components. The sample's XRD patterns and the percentage diagrams are given in Appendix C. The discussion of results will take place on the next section.

Table 3-2 XRD bulk analysis HighScore Plus

Samples Group	Sample #	albite high, %	sanidine, %	anorthoclase, %	phillipsite, %	quartz low, %	Calcite, %	Clinoptiolite, %	Montmorillonite, %	Magadiite, %	Kaolinite, %	Halite, %	Trona, %	Erionite, %	Analcime, %	MgCa, %	Illite, %	Chabazite, %	Phillipsite, %	Mordenite, %	Virmiculite, %	Christobalite, %	Thermonatrite, %
A	**1**		22	42		2	31	3															
A	**2**			56		17						8	13	6									
A	**3**	20	29			9		4						9	2	16	11	1					
A	**4**	22		32		7						5	13	1					19				
A	**5**	20	17	18		16						2	2	24									
A	**6**		18			13	5	6	49				6	2									
A	**7**		15	57								2	25									1	
A	**8**					1						6	43	14								1	
A	**9**		56			4	40																5
A	**10**		44			2	9							43									
A	**11**		76				7													17			
A	**14**		51	33		16																	
A	**16**	12	12		36			16	11			7	6										
A	**18**		20		50													7		24			
A	**19**		58									12		30									
B	**21**								9	18	73												
C	**12**		19	37	44																		
C	**13**	12	4	14	70																		
C	**15**		28		72																		
C	**17**	51			37											10					2		
C	**20**	4			92	4																	

3.1.1 MATLAB Analysis

The measured percentages of minerals of each sample were visualized using MATLAB based on the percentage ratio of minerals in the samples calculated in HighScore Plus Software (Figure 3-2). Figure 3-1 - Figure 3-4 show Scatter plots of "latitude vs. halite," "latitude vs. quartz," "longitude vs. quartz," and "longitude vs. trona" are shown in

Figures 3-1-Figure 3-4. Each dot represents a specific sample point in these scatter plots. This type of plot is useful to quickly visualize any correlations that may exist in the data. Correlation signifies that the setting of one variable has an influence on the value of the other. Typically, one would employ principal component analysis to identify important correlations; however, the small scarce amount of samples available would have been insufficient to yield a good estimator of the covariance matrix, which is required by PCA. Instead, it was decided to plot a line through the data using a least squares fit; this correlation provides a visual reference to assess the amount of scatter. Hence, if a relationship exists between the quantities listed on the axes, the dots will exhibit a non-random pattern.

For example, it can clearly be seen in Figure 3-1 that quartz and longitude are linearly correlated. Quartz decreases as the longitude increases, suggesting that one is more likely to find quartz west of the lake than east. It turns out that the longitudes coincide with increased elevation. These data enable to test the hypothesis showing that authigenic mineralization was increases with the elevation. This correlation might mean that the high concentration of low quartz occur in the Nairobi formation with higher precipitation and more alkali-earth minerals (magnesium, calcium). Similarly, there seems to be a linear relationship between halite and latitude. Halite increases with latitude, which coincides with presence of the Magadi Trachyte area to the higher elevation and higher attitude. This correlation might mean that the halite concentration is increasing with increasing of elevation and precipitation.

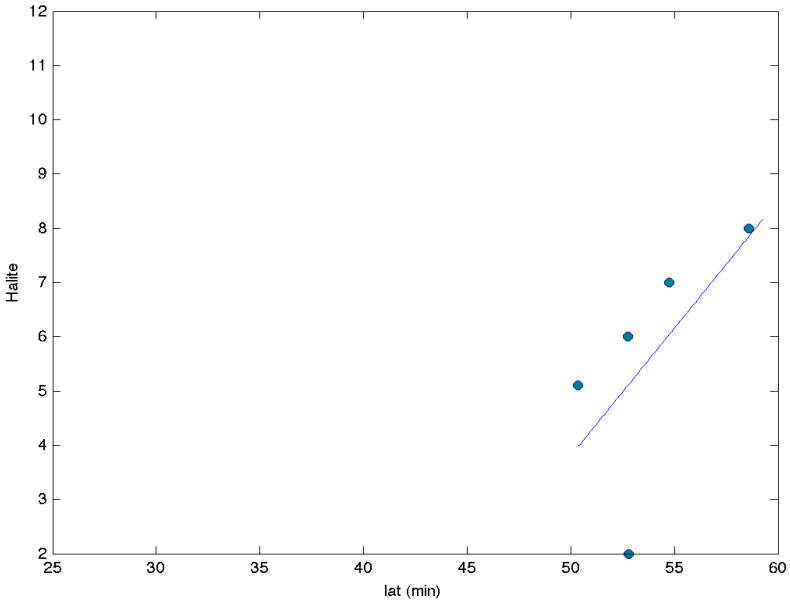

Figure 3-1 Halite vs. latitude.

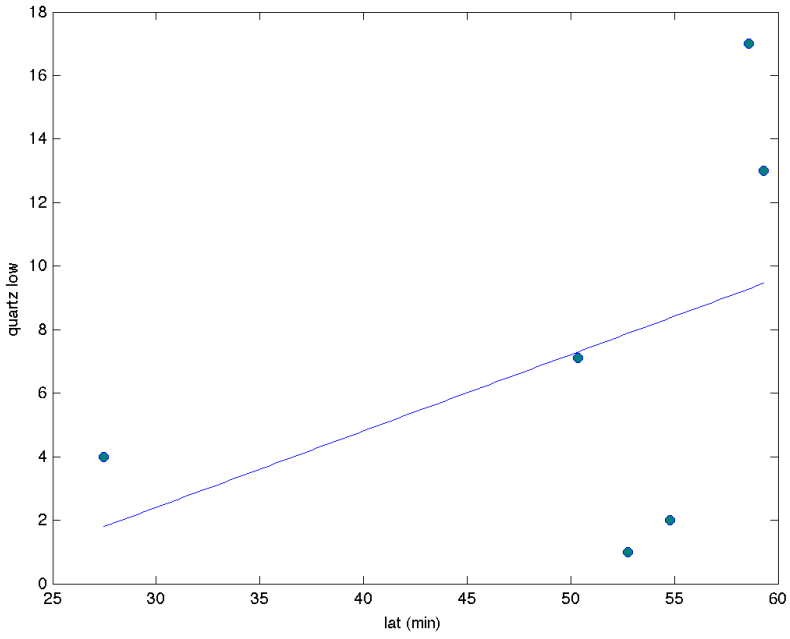

Figure 3-2 Quartz (low) vs. latitude.

For example, Figure 3-2 and Figure 3-2 demonstrate the correlation between quartz and latitude and halite and latitude. The pattern states that the abundance of illite and quartz increases with latitude. Another example of correlation between variables traced between longitude and trona and longitude and quartz. Figure 3-3 and Figure 3-4 demonstrates that the concentration of quartz decreasing with increasing of longitude. However, trona did not correlate with longitude. Trona exists throughout in the whole research area at the different longitudes. However, there is not enough data and the scatter is too large to make any conclusions about quartz concentration on different areas.

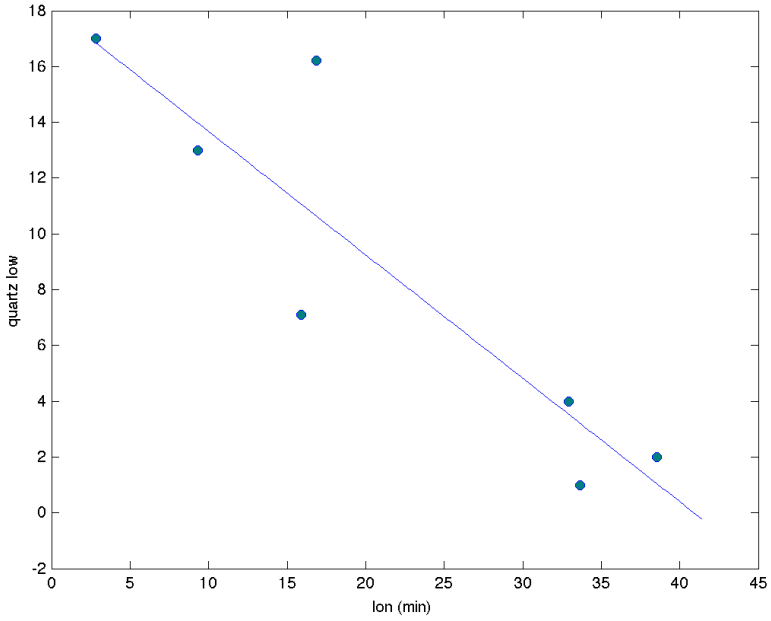

Figure 3-3 Longitude vs. quartz

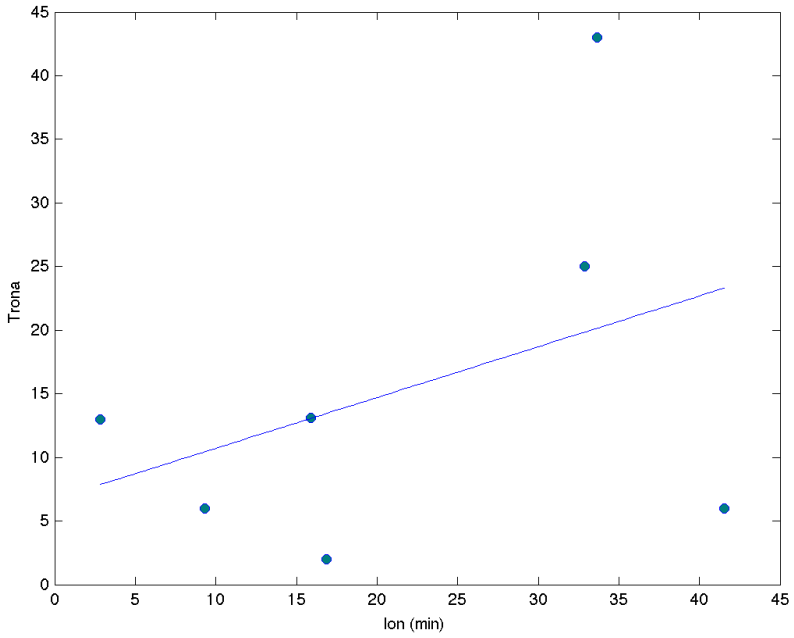

Figure 3-4 Longitude vs. trona.

3.1.2 X-Ray Diffraction Cluster Analysis

XRD cluster analysis was implied to examine the identified phases' quantification. The principle component analysis (PCA) was performed as 3D image (Cammelli et al., 2010). PCA demonstrates the possible correlation or uncorrelated variables of minerals in twenty-one research samples. Cluster analysis combined similar diffractograms attributes as peaks, cleavage and positions of crystal structure, and strengths these parameters into statistic correlation. However, the percentage ratio of all the present minerals is approximate due to lack of structural information availability.

Figure 3-5 demonstrates that all twenty-one samples could be divided into two clusters (blue and green) and established on the right corner of PCA. The outliers represented by for samples # 7, 13, 14, and 20 consist of different mineralogy or different

peaks intensity. All outlier samples were mainly located on the left side of PCA diffractograms. All outliers display a significant difference in their mineral composition, demonstrated that the mineralogy varied from sample to sample.

The largest cluster C1 (blue) consist of samples # 6, 10, 8, 9, 11, 12, 15, 16, 17, 18, and 19. The green cluster contains only 5 samples with similar chemical crystal structure: 1, 3, 4, 5 and 21. The PCA results will be discussed in the Discussion section.

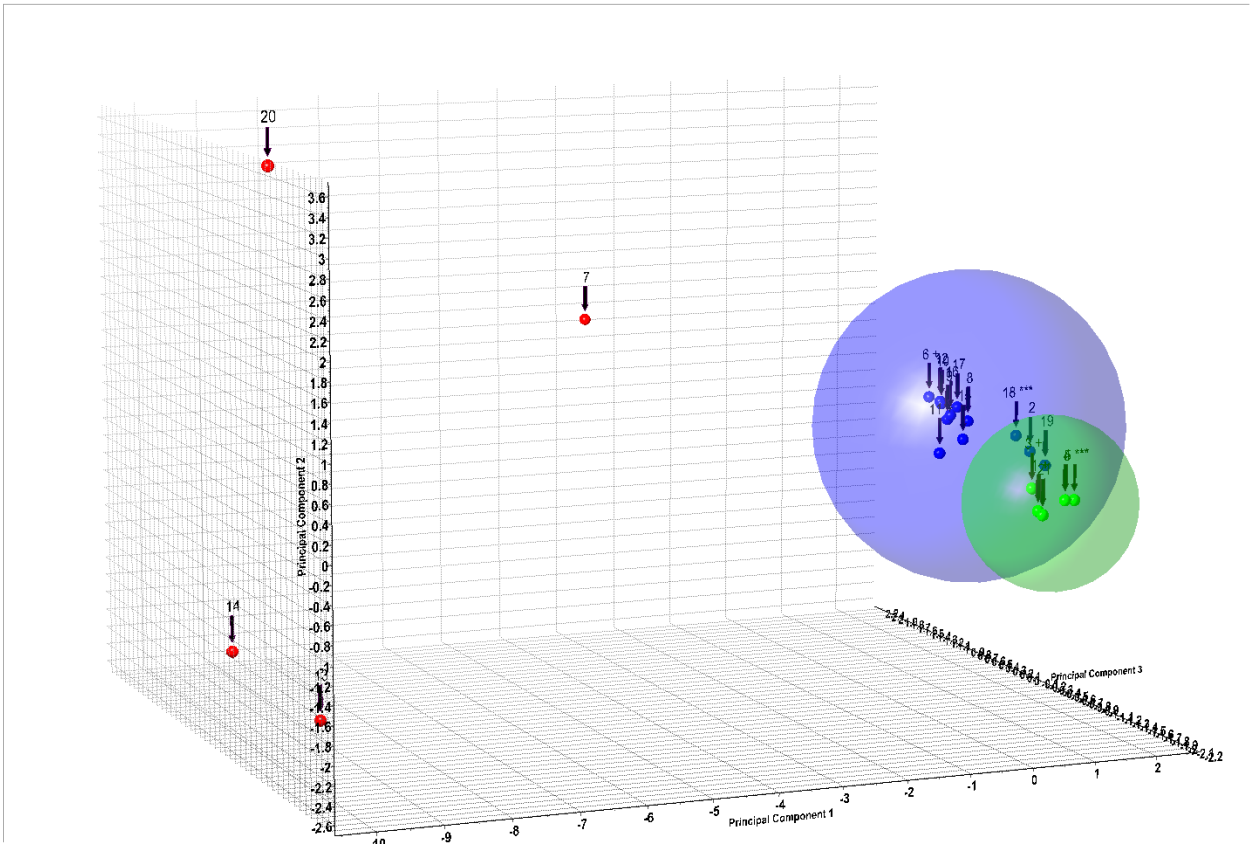

Figure 3-5 Cluster analysis of bulk samples.

3.2 XRD Clay Analysis

3.2.1 ***Chemical method of sample preparation***

After careful inspection of bulk patterns, it was determined that only 12 samples out if 21 or ~ 57% of all the specimens consist of clay-based minerals (i.e. phyllosilicates). Following samples were selected for clay analysis: sample # 6, 7, 8, 10, 11, 12, 14, 15, 16, 17, 18, and 21 (Group A – samples # 6, 7, 8, 10, 11, 16, 18; Group B - #21, Group C – 15, 17) . For the first clay-sized structural information analysis, all the samples were prepared using chemical treatment or Jackson's method (Jackson, 1979) and then, the powder sample was prepared and placed into a microscope slides (Hradil et al., 1997). After performing the XRD clay analysis, we determined that samples analyzed after being processed with Jackson's treatment did not produce quality diffraction patterns. The reason is that although Jackson's treatment is useful in detrital clay analysis and it is proven less effective in analysis of authigenic zeolite type clay minerals possibly due to incompletely formed crystal structures. For example, Figure 3-6 represents the pattern of sample # 16 after Jackson's treatment, the d-spacing of peaks also indicated on the pattern.

The slide was dried using two methods: 1) at room temperature for 24 hours (red pattern), 2) the slide was stored in an ethylene glycol, solvation for vapor explosion for 24 hours (green pattern). Weak peaks of smectite, chlorite/kaolinite, and kaolinite can be observed. Also the extra noise was present on the patterns. Weak peaks and extra background noise was observed on all the received patterns that were treated using Jackson's methods

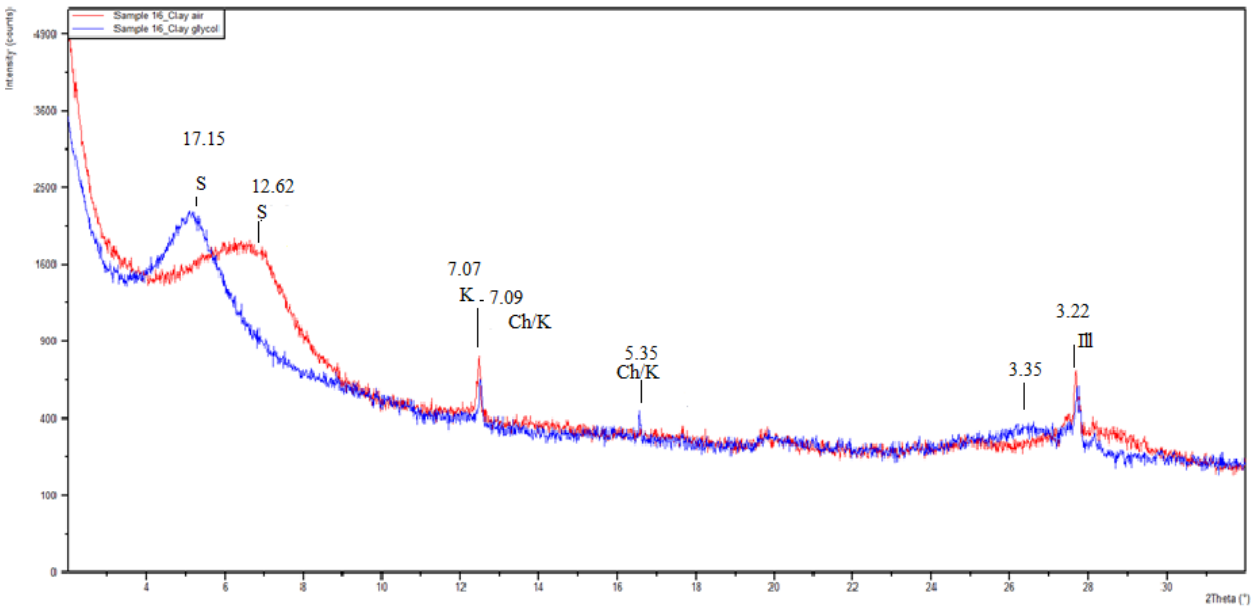

Figure 3-6 XRD clay analysis of Sample # 16 (Group A) after Jackson's treatment.

3.2.2 XRD patterns after the physical treatment

For the second XRD – clay analysis samples were treated by sonication. Clearer peaks were observed after XRD analysis. For example, Figure 3-7 demonstrates the pattern of sample # 16 after sonication treatment. In comparison, to the patterns after Jackson's treatment, sonication treatment does not destroy some minerals, which can be observed on the diffraction pattern.

According to the quantitative analysis of XRD data, low quartz, vermiculite, calcite, montmorillonite, and phillipsite were recognized as the most abundant. The peaks of low quartz were discovered at 2.45 Å, 3.34 Å, and 4.25 Å; the peaks of montmorillonite were identified at 15.03 Å, 5.01 Å, 3.77 Å and 3.02 Å. Phillipsite peaks, which were not seen in the samples treated using Jackson's methods, were seen at 17.52 Å, 12.56 Å, and 10.84 Å.

Table 3-3 indicates the abundance of minerals in researched samples. However, the percentage ratio of minerals in the samples was not calculated due to two reasons. First, the high background noise was observed in these samples. This increased background and noise and peak deviation was due to process of peeling from the slides. Peeling was observed in the samples as soon as samples started to dry. Peeling samples were # 6, 7, 10, 12, 11, 14, and 21. Another reason for high probability of deviation ratio calculation is some unidentified or questionable minerals were found in the samples. The peak at 20.71 Å was discovered but was not identified by HighScore Plus software. Furthermore, the d-spacing of some minerals is very close to each other, thus it was not clear enough which minerals some of the peaks belong to. Further investigation is required in order to verify our results.

Table 3-3 XRD Clay analysis

Sample #	Erionite	Quartz Low	Mordenite	Vermiculite	Montmoriollite	Corundum	Fluorite	Phillipsite	Cristobalite	Magadiite
6	✓							✓		
7			✓							
8	✓				✓					
10	✓			✓				✓		
11	✓									
12										
14	✓	✓	✓							
15				✓						
16		✓			✓	✓	✓	✓	✓	
17					✓					
18		✓								
21					✓					✓

A unique peak was detected in sample 16 at d-spacing of 20.71 Å (Figure 3-7). After the solvation with ethylene glycol vapor at room temperature, the following peak

shifted to 22.70 Å. To identify the mineral composition of sample # 16 the scanning electron microscopy analysis had been assigned to this sample (Section 3-3). Based on diffraction characteristics, the peak at 20.71 Å is identified as magadiite.

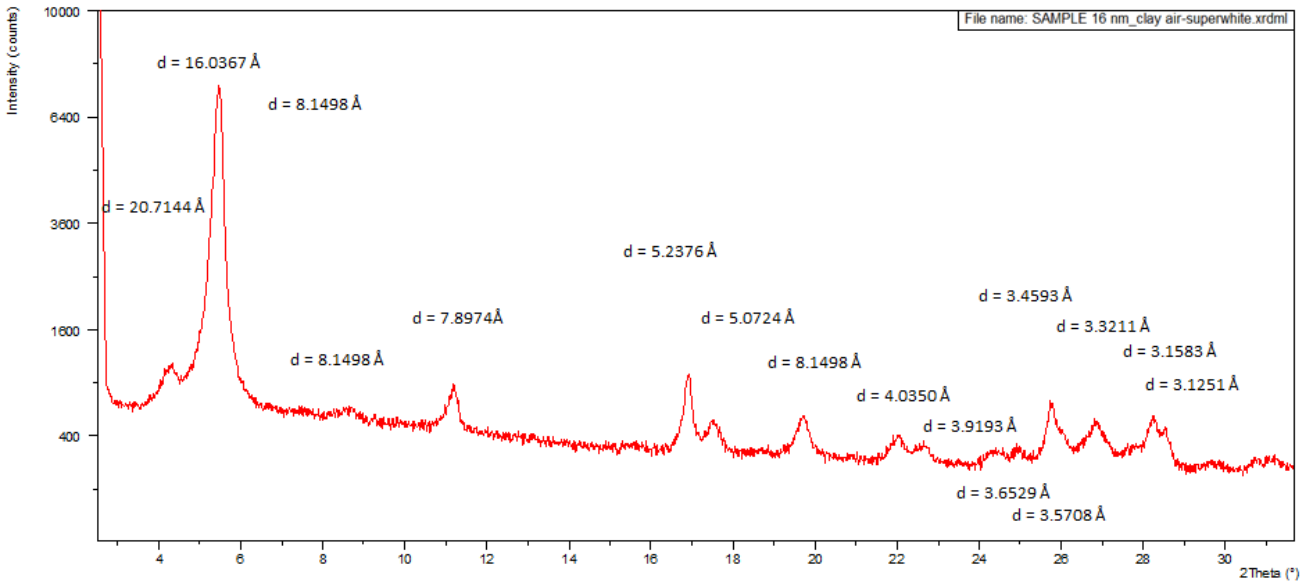

Figure 3-7 XRD Pattern of Sample #16 (Group A) after sonication.

3.3 SEM-EDS Results

The following SEM – EDS results were carried out for samples 12, 16 and 17, in order to further confirm the aforementioned presence of magadiite as well as the presence of okeonite and zeolites. Okeonite would be a possible explanation for the 20.71 Å peak observed Figure 3-7. In particular, they were used to check whether or not the okenite was present in the specimens. The findings are shown in Figures 3-10 through 3-17. The X-ray microanalysis for each sample, respectively, is shown in Figure 3-8 and Figure 3-14. The corresponding X-ray secondary electron images are shown in Figure 3-9,Figure 3-9, Figure 3-10 and Figure 3-14. All the images were taking at the cross with 15.00 kV accelerating

voltage for electron gun (beam energy), from the distance of 25 mm by SE1 as a secondary electron detector Figure 2-7.

The SEM analysis found that the most abundant elements in sample #12 of Group B (Figure 3-8) were sodium (Na), silicate (Si), iron (Fe) and potassium (K). Weak peaks of titanium could also observed in the microanalysis, but since they did not exceed the calculated background noise (grey line), no formal conclusion could be made about the presence of titanium.

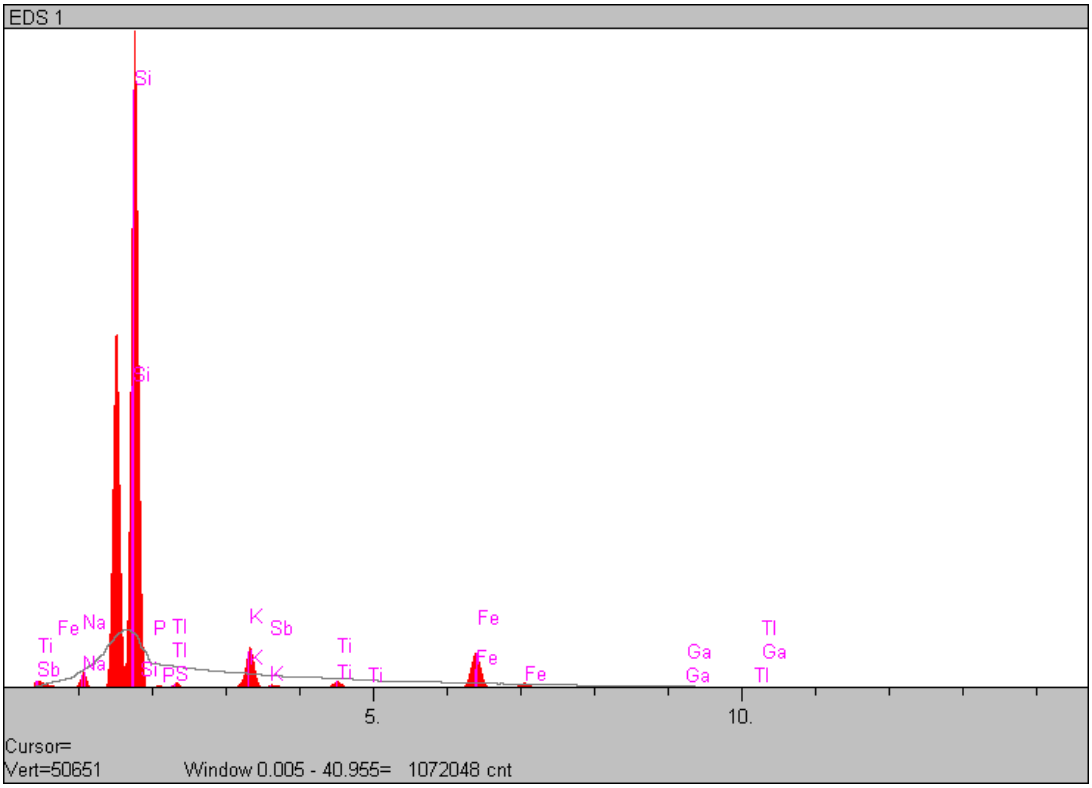

Figure 3-8 X-Ray Microanalysis of Sample #12 (Group B).

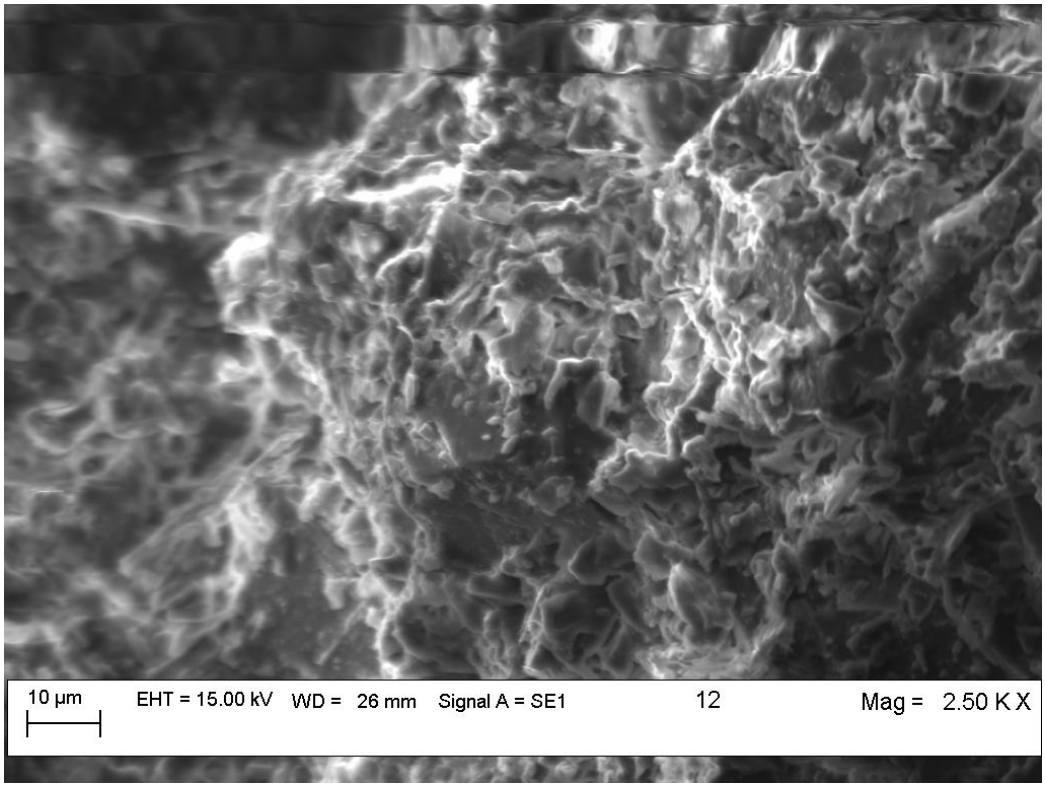

Figure 3-9 X-Ray Electron Image of Sample #12 (Group B).

Three representative secondary electron images were taken of sample #16 (Group A). Figure 3-10 demonstrates the snapshot of the sample 16. All the images of sample 16 were taken at the same parameters. The scale of the image illustrated on the picture. The other two images of sample 16 are located in the Appendix C.

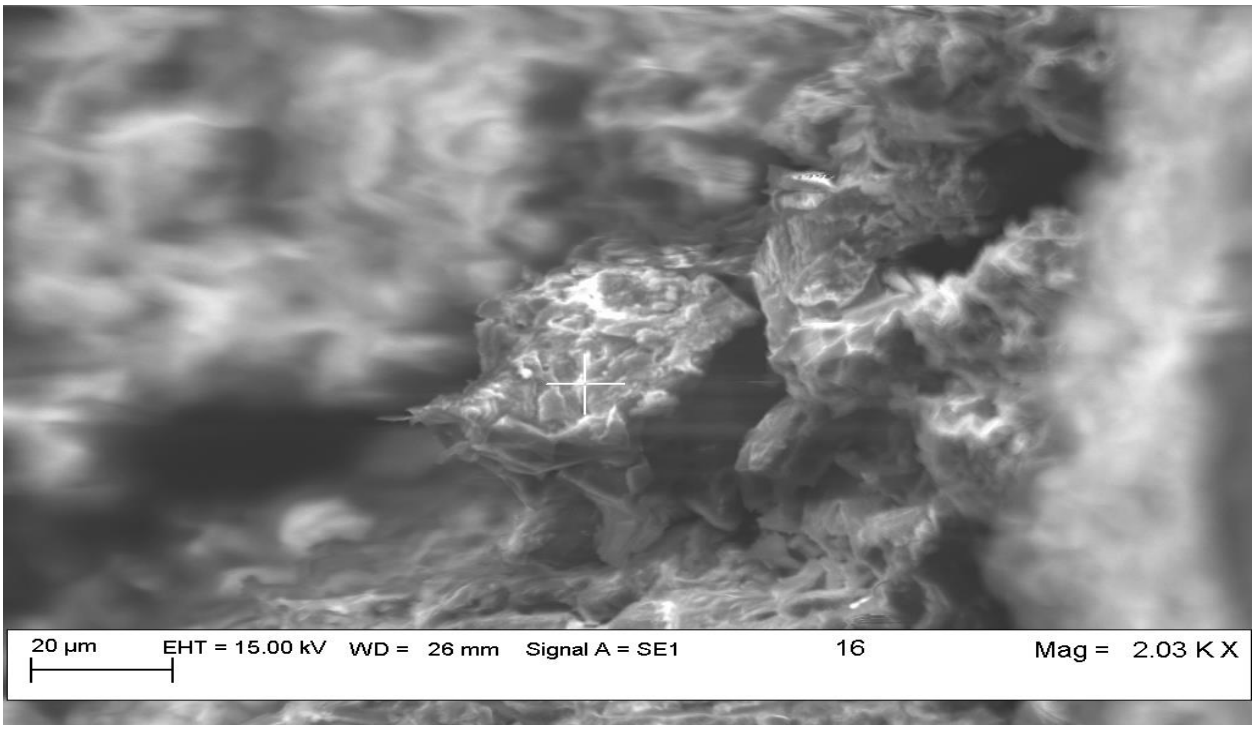

Figure 3-10 X-Ray Electron Image of Sample #16-01 (Group A).

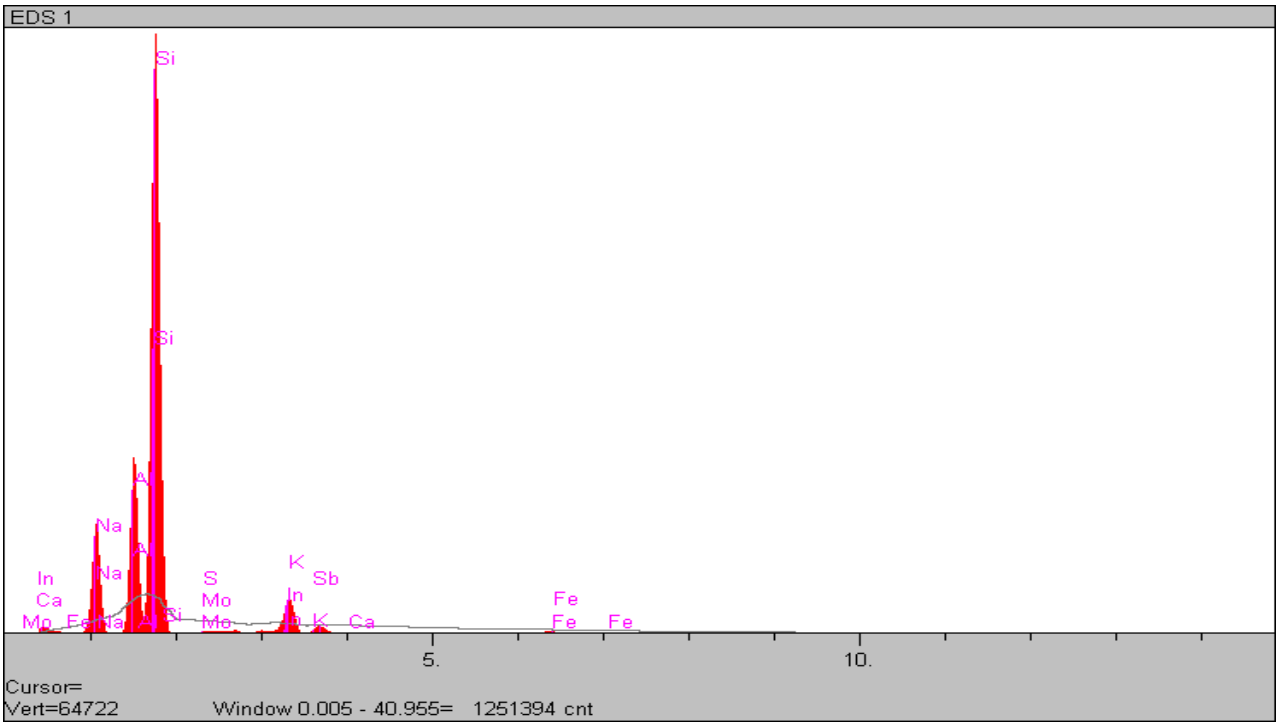

Figure 3-11 Ray Microanalysis of Sample #16-01 (Group A).

The analysis was repeated twice: once at a gun distance of 28 mm and another at a gun distance of 25 mm. The SEM analysis at 28 mm found three representative secondary electron images were taken of sample #16 (Group A). These elements are shown in Figure 3-10 and Figure 3-13. The SEM analysis at 25 mm is shown in Figure 3-12, after honing in on one of the cavities. It was found that the most abundant chemicals were sodium (Na), silicate (Si) and calcite (Ca). Aluminum (Al) and potassium (K) were not detected, even though this is the same sample, while calcite was observed at 25 mm, even though it was detected at 28 mm. The associated crystal structure is shown in Figure 3-13, where the white cotton-looking formation is believed to be fibrous crystal. The presence of a newly discovered calcite and the observed fibrous crystal structure in the cavity are indications of possible okenite. The discussion will be provided in the following section.

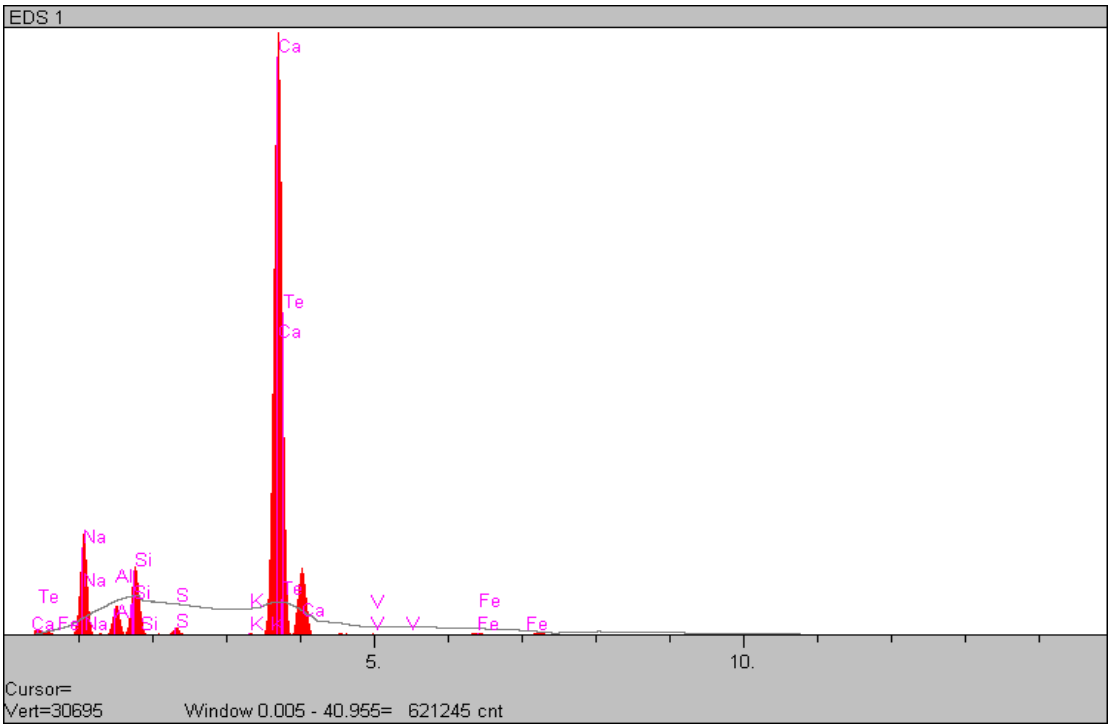

Figure 3-12 X-Ray Microanalysis of Sample #16-02 (Group A).

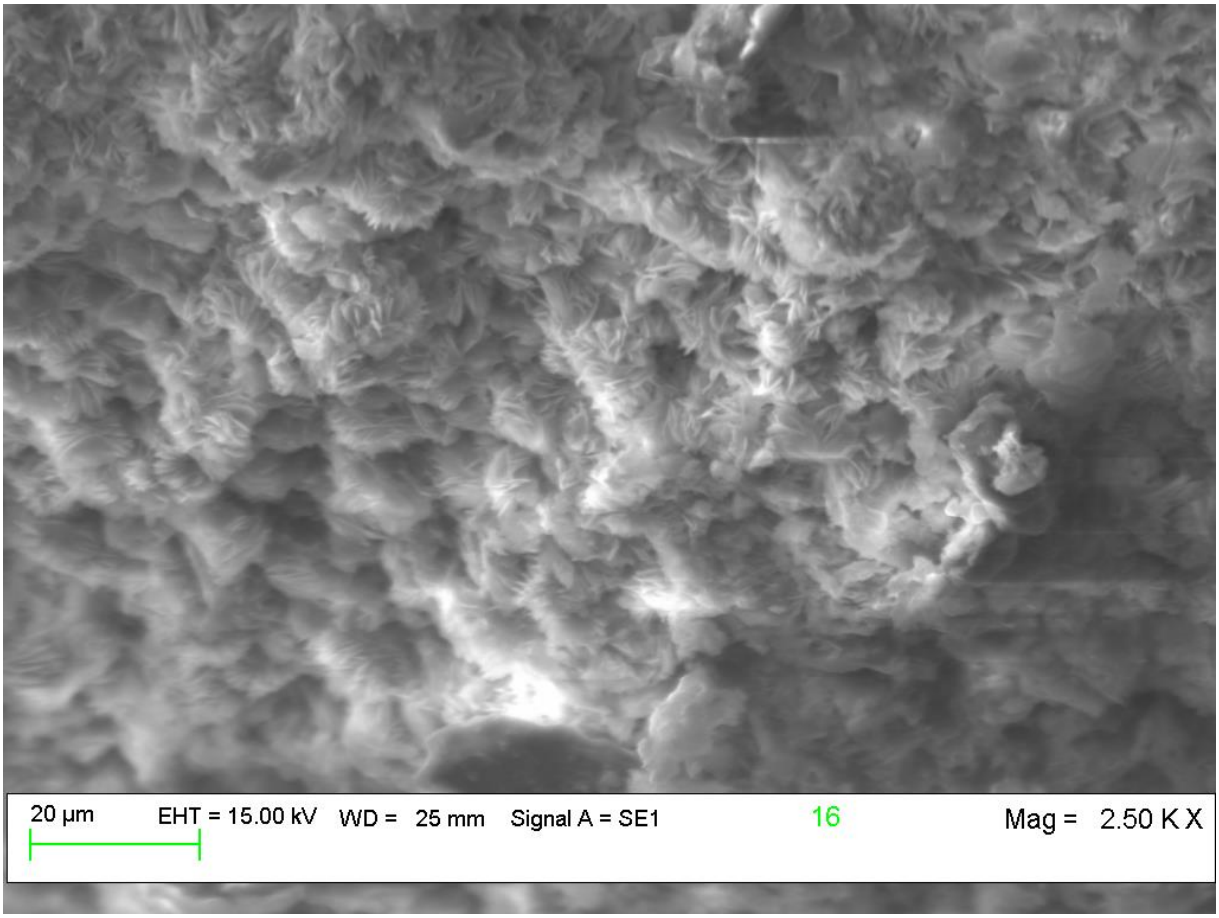

Figure 3-13 X-Ray Electron Image of Sample #16-02 (Group A).

Four sides of sample #17 (Group B) were investigated on SEM. The SEM analysis examined that the most abundant chemicals founded in the first investigated surface 17 are sodium (Na), silicate (Si), Aluminum (Al) and iron (Fe) (Figure 3-14). Seven secondary electron images were taken of sample #17. Figure 3-15 represents the snapshot of the sample with circular grains. Image was taken with 15.00 kV accelerating voltage for electron gun (beam energy), from the distance of 25 mm by SE1 as a secondary electron detector. The other two images of sample 17 are located in the Appendix D.

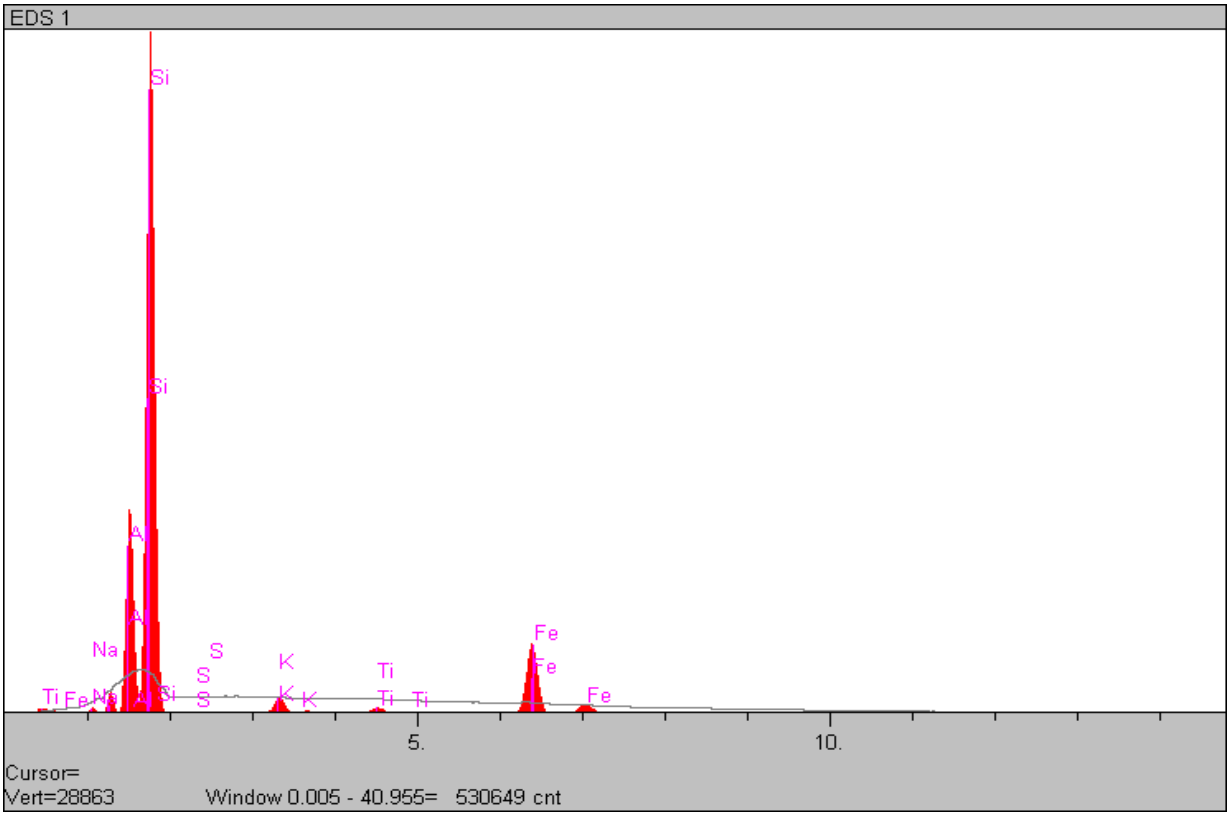

Figure 3-14 X-Ray Microanalysis of Sample #17 (Group B).

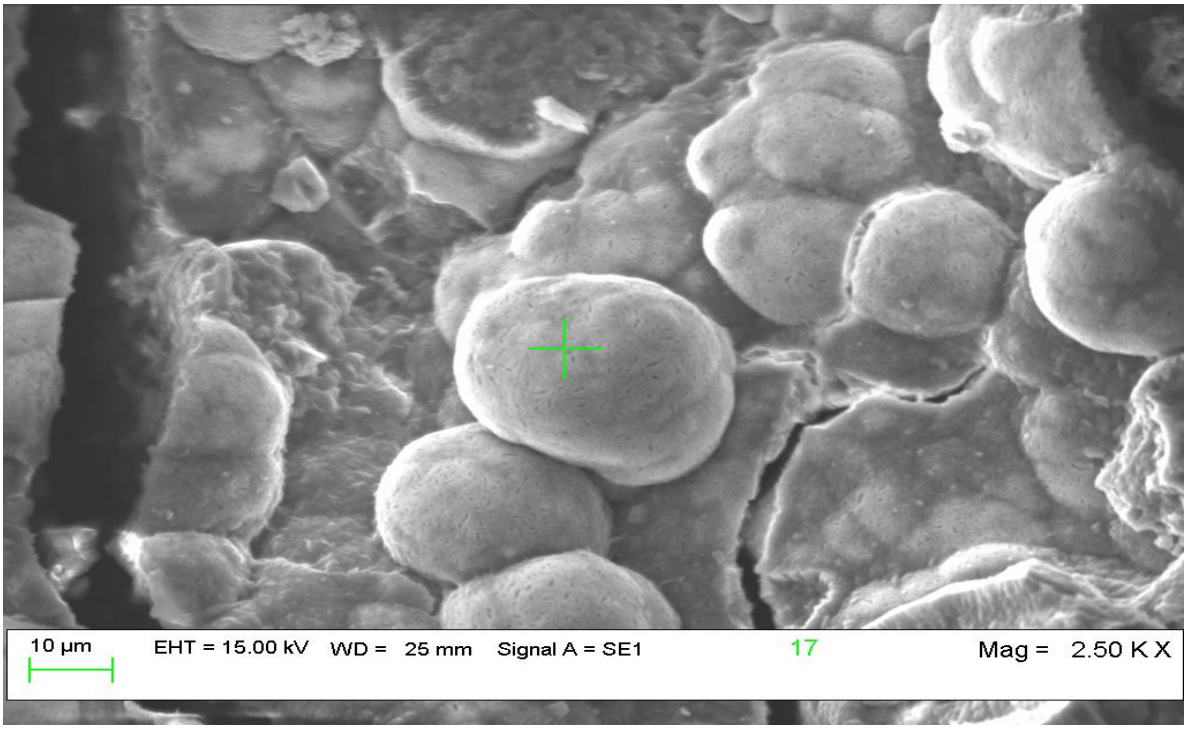

Figure 3-15 X-Ray Electron Image of Sample #17 (Group B).

4 DISCUSSION

4.1 XRD

4.1.1 Principal Component Analysis

Samples with similar patterns were combined into clusters (Figure 3-5). The blue cluster C1 includes samples # 2, 6, 8, 9, 10, 11, 12, 15, 16, 17, 18, and 19. Table 4-1 Mineralogy of C1 (blue) cluster indicates samples locations and mineralogy for each sample in the cluster (Table 4-1). All samples, with the exception of samples # 12, 15 and 17, belong to sample Group A collected at the lower bed of Magadi Trachyte area. These samples basically consist of sodium aluminum authigenic silicate minerals such as sanidine, anorthoclase, montmorillionite, cristobalite, thermonatrite. Samples include the high percentage of zeolites, i.e. clinoptolite, erionite, phillipsite, and associated zeolites minerals such as magadiite and possibly okenite. Another words, cluster C1 combined samples with alkali –rich minerals and this statement supported our hypothesis.

Samples # 12, 15 and 17 from the Group C consisted of a higher percentage of sanidine and zeolite phillipsite. It is similar in mineralogy to the mineralogy of the volcanic rich soils in the Nairobi area. Due to this similarity, the contents were combined at the same cluster with samples Group A. Thus, the correlation traced between the geographical location and authigenic mineralization. This part of analysis proves the hypothesis that at the lower elevation (580 m above sea level) the concentration of authigenic minerals is relatively high.

Table 4-1 Mineralogy of C1 (blue) cluster.

Sample #	Group	Mineralogy
6	A	Sanidine, Quartz low, Calcite, Clinoptolite, Montmorillionite, Trona
8	A	Halite, Trona, Erionite
9	A	Sanidine, Quartz low, Calcite
10	A	Sanidine, Quartz low, Calcite, Erionite
11	A	Sanidine, Calcite
12	C	Sanidine, Anorthoclase, Phillipsite
15	C	Sanidine, Phillipsite
16	A	Albite High, Sanidine, Phillipsite, Clinoptolite, Montmorillionite
17	C	Albite High, Phillipsite, Clinoptolite, Magnesium Calcite
18	A	Sanidine, Phillipsite, Mordenite, Chabazite
19	A	Sanidine, Halite, Erionite

The green cluster C2 consists samples # 1,3,4, 5 and 21. Samples 1,3,4 and 5 were collected from the Magadi area and belong to the Group A, but sample 21 (Group B) was collected from the Olorgesailie area at high elevation and was included in the same cluster. Table 4-2 demonstrates that most of the samples comprised of albite, sanidine, quartz, calcite, anorthoclase and calcite. However, sample 21 consists of montmorillionite, kaolinite and magadiite. Thus, it can be concluded that sample # 21 was included into cluster C2 because of its basic chemical composition of magnesium (Mg), sodium (Na), silicate (Si), and aluminum (Al). It was determined by HighScore software that sample #21 contains synthetic magadiite or mordenite (mordenite has the same d-spacing as synthetic pattern of magadiite. So, the HighScore software accidentally identified synthetic magadiite instead of mordenite.

Table 4-2 Mineralogy of C2 (green) cluster

Sample #	Group	Mineralogy
1	A	Sanidine, Anorthoclase, Quartz Low, Calcite, Clinoptolite
3	A	Albite High, Sanidine, Quartz Low, Illite, Magnesium Calcite, Erionite
4	A	Albite High, Anorthoclase, Quartz Low, Halite, Trona, Phillipsite
5	A	Albite High, Anorthoclase, Quartz Low, Halite, Trona, Sanidine, Halite, Erionite
21	B	Montmorillionite, Kaolinite, Magadiite

* For sample #21 magadiite should be replace for mordenite

4.1.2 Data visualization

For data visualization, MATLAB application was applied. This type of plot is useful to quickly visualize any correlations that may exist in the data. Correlation signifies that the setting of one variable has an influence on the value of the other. Typically, one would employ principal component analysis to identify important correlations of bulk analysis; however, the small amount of sample available would have been insufficient to yield a good estimator of the covariance matrix, which is required by PCA. It is reasonable to say that quartz and longitude are linearly correlated as shown in Figure 3-3. Quartz decreases as the longitude increases, suggesting that one is more likely to find quartz increases towards to the Magadi area to the east. In other words, the higher concentration of quartz is observed in the lower Magadi Trachyte area. Consequently, the Lake Magadi basin (Group A) consist of silica based minerals which were abundant with time and under the influence of hot springs, pressure and pH to zeolites, authigenic clay, and zeolites associated minerals. It turns out that the longitude coincides with decreasing elevation and increasing

of alkali-rich and alkali-earth poor minerals concentration, but decreasing of detrital minerals.

Similarly, there seems to be a linear relationship between Halite and latitude (Figure 3-1). Halite increases with latitude, which coincides with increasing of elevation. This correlation might mean that the concentration of actual clay increases with altitude. It is feasible, because the higher elevation area has more fresh water precipitation, more vegetation. Thus, the Kiserian area (Group C) consists of actual clay at the elevation of 1600 m above sea, whereas the Magadi basin has a negligible amount of poor clay. This observation supports our hypothesis.

4.2 XRD Clay Results

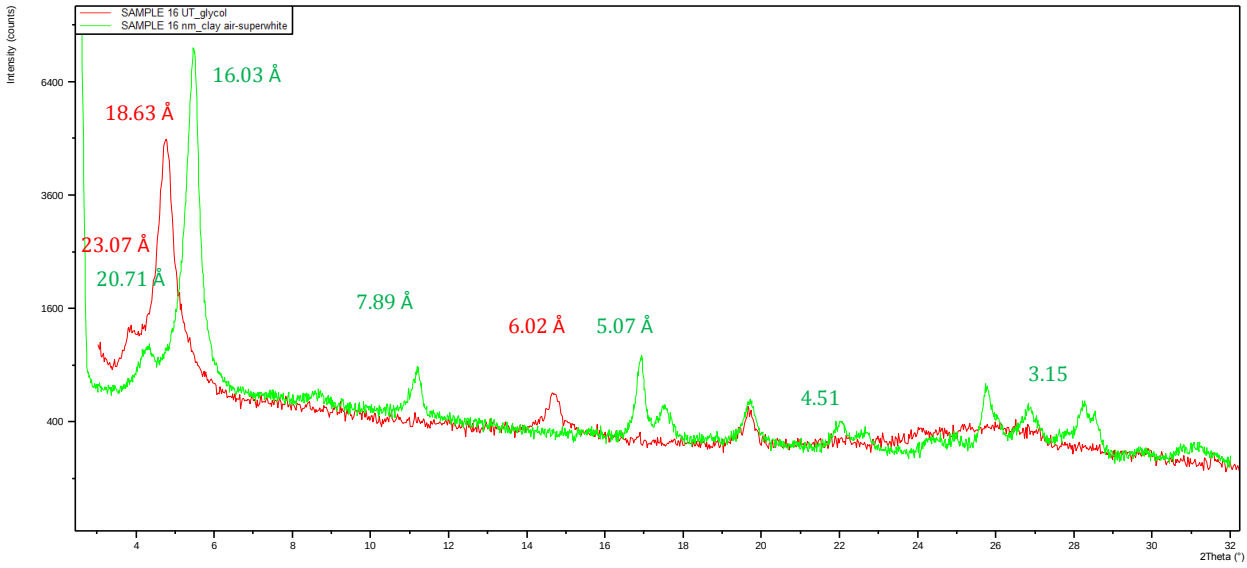

Figure 4-1 Sample #16 clay mineralogy analysis (red pattern – air dry, green pattern – ethylene glycol treatment)

4.2.1 General Analysis

According to XRD clay analysis, samples from the Magadi basin (Group A) consist of zeolites, authigenic clay, and associated zeolite minerals. Thus, phillipsite, clinoptolite, mordenite, chabazite were detected in samples. Magadiite was found only in one sample of Group A – sample # 16.

Unexpectedly, magadiite was found in sample # 21 (Group C), which was collected from the Olorgesailie area. Thus, it is reasonable to say that magadiite was formed with weathered basalt clay under certain weathering conditions in addition to being an authigenically formed silicate.

Group C was collected at the highest altitude and it was discovered that these samples contain more detrital clay and detrital based minerals such as anorthoclase, sanidine, albite, vermiculate, analcime, erionite, kaolinite, illite, montmorillionite. Therefore, the concentration of actual clay-sized silicate minerals likely resulting from pedogenic processes at the higher elevation supports the hypothesis.

4.2.2 XRD of Sample #16 (Magadiite 14 - MAG – 2 – Group A)

After the general clay analysis, attention was concentrated on sample #16 and basically at the unknown peak with d-spacing of 20.7144 Å, In order to test our hypothesis and to determine the authigenic mineral formation reaction, the further research was focused on the investigation of the unknown peak. The first assumption was that this peak belongs to the clay-based mineral. To prove this theory, the specimen was stored in the ethylene glycol tank for 24 hours. According to the Moore & Reynolds, (1997), expendable 2:1 layer phyllosilicate (smectite) clay-based mineral peaks should shift to higher d-spacing

values after the glycol solvation. Figure 4-1 demonstrates that the peak shifted to the higher d-spacing of 23.07 Å.

The literature search was implemented to identify the d-spacing of peak at 20.71 Å and at 23.07 Å. According to the Vida and Volzone (2009) and HighScore Plus software, the unknown peak can be identified as Ca - Montmorillionite. However, montmorillionite is a member of smectite group, and by definition, whose d001 d-spacing value typically cannot be shifted to d-spacings higher than 17 Å after soaking in ethylene glycol.

The next assumption was that 20 Å peak belongs to hydrosodium silicate kenyaite ($Na_2Si_{22}O_{41}(OH)_8$•6(H2O) (Kodikara et al., 2012). According to Eugster (1980), kenyaite forms at the High Magadi beds with nodules of magadiite (Warren, 2014). Thus, this possibility wase tested with scanning electron microscopy. We found that Ca was present from SEM analyses. Thus, this phase is not kenyaite.

Frost and Xi (2012) stated that the 21 Å, 3.15 Å, 3.45 Å, and 7.89 Å peaks belong to the silica based mineral okenite ($Ca_3[Si_6O_{15}]$•6(H_2O). Okenite is the mineral associated with other zeolitic minerals and magadiite (Guthrie and Carey, 2015). Previous research attributes that okenite was found with basalt and is a product of alkali-silica reactions (Peterson et al, 2006). The observed 20.71 Å of our research sample might be okenite, even though the mineral database stays that the okenite peak has 21 Å d-spacing. HighScore software has only the patterns for dehydrated peaks and does not include the information of hydrated zeolites associated minerals. SEM qualitative analyses showed the presence of Si, Ca, Na (trace), which is consistent with the presence of okenite.

Finally, we dehydrated a sample of magadiite. The d-spacings of dehydrated magadiite was similar to those d-spacings observed for sample 16 except that the

dehydrated magadiite did not have the peak at 21 Å. Thus, the scanning electron microscopy procedure was used to help identify the mineralogy of specimen #16. Likewise, samples #12 and 17 with questionable mineralogy were chosen for SEM analyses.

4.3 SEM Results

SEM results provided qualitative chemical microanalysis and high-resolution surface images. First examined sample was specimen # 12 from Nairobi area (Group A) from the Kiserian area. The microanalysis of sample #12 identifies that the most abundant elements are sodium (Na), silicate (Si), aluminum (Al), iron (Fe) and potassium (K) (Figure 3-8). These SEM results support our assumption that the Magadi Trachyte area described as detrital silicates, quartz, calcite and saline minerals.

The first representative SEM image and microanalysis was taken from the surface of sample #16 (Figure 3-11). The microanalysis reveals that the surface of the specimen comprised of sodium (Na), silicate (Si), and low percentage of potassium (K), as small peaks were observed. Chemical composition and SEM image support our evidence that montmorillonite is possibly present at this sample.

The next three images were taken from different cavities of the sample. Surprisingly, chemical analysis showed the abundance of calcium (Ca), which can be the evidence of the presence of okenite based on silicon (Si) and a peak of sodium (Na). The high peaks of calcium were the first evidence of okenite $[Ca_3[Si_6O_{15}]\bullet 6(H_2O]$ present in abundance in the cavity. Sodium is not the part of the okenite mineral structure. However Cole & Lancucki, (1983) stated that "calcium in okenite can be replaced with sodium with time". Based on the method of sample preparation for SEM where the sample is put under high vacuum, the okenite was assumed to be dehydrated and thus the crystal structure

started to transfer to dehydrated structure, and the swelling pattern of okenite was lost (Frost & Xi, 2012b).

The image of the cavity represents the white fibers (crystals) or white cotton balls (Frost & Xi, 2012a). The same description of okenite and chemical structure Frost & Xi, (2012a) provided in their research of vibration spectroscopic study of okenite. Another relevant factor is that the okenite is the reaction product of alkali silicates (Peterson et al., 2006) and possibly could be formed on our studied area. Therefore, it provides us a strong evidence of okenite formation in that area. Thus, okenite is an authigenic mineral, which was identified at the low elevation area – the hypothesis was further confirmed by finding okenite in an area composed of authigenic minerals. The identification of okenite can be further confirmed via the use of scanning transmission electron microscopy coupled with analytical elemental microscopy (Klint & Elliott, 2000)

The chemical analysis of sample #17 was taken from the same Kiserian area (Group C) as sample #12 (Figure 3-16). Microanalysis shows that sodium (Na), silicate (Si), aluminum (Al), iron (Fe) and potassium (K) are present. The common chemistry demonstrates that the minerals formed from the detrital material under the same erosion processes. Thus, our hypothesis is partially supported in that the minerals formed on the high elevation with higher vegetation and precipitations are will consist more of volcanic soils, more alkali earth minerals, and detrital minerals.

4.4 Preliminary dehydration-rehydration of Na-silicate minerals

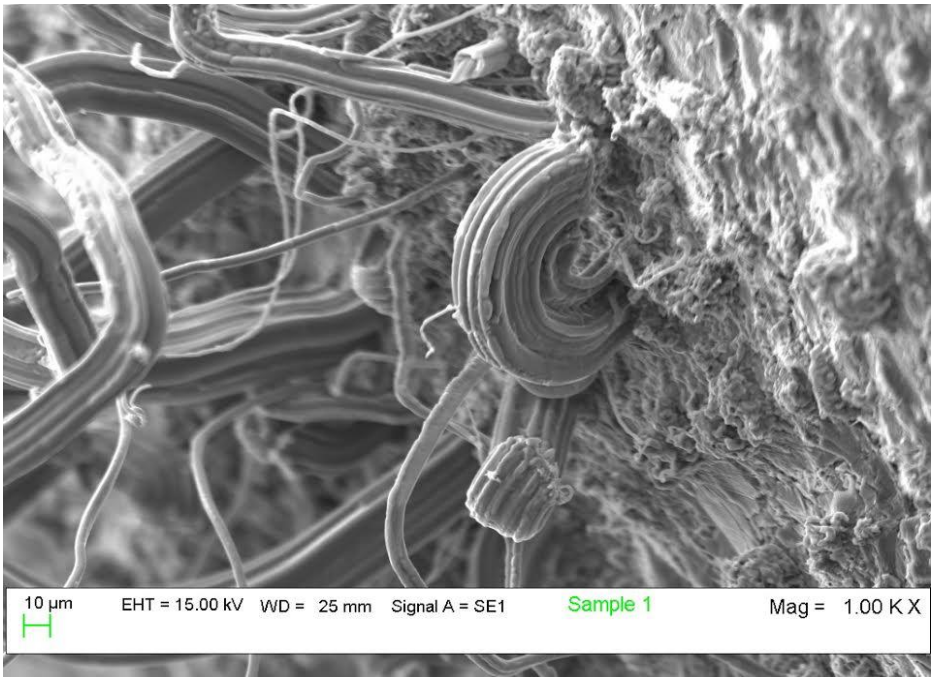

Figure 4-2. Synthesized sodium chloride.

The reaction of a solution of magadiite and the chalk produced an abnormal and novel crystal habit for (Figure 4-2) of sodium chloride on a matrix of sodium chloride silicate (magadiite). This habit is a new observed habit for NaCl, typically cubic habit. XRD data was not measured for this crystal. Elemental analyses show presence of Na and Cl. The SEM can not detected the presence of elements whose atomic number is lower than 11 (Na). Thus, elements such as C and O might be present but not detected. Another likely phase could be $NaCO_3$. The achieved result demonstrated that our theory that okenite can be formed from magadiite and brine solution was incorrect. However, the calcium carbonate was detected in addition to NaCl (Figure 4-3), but this calcite appears to be dissolved in brine by reaction with a sodium chloride matrix. Given the evaporation of saline brines at STP yield euhedral and cubic crystals of halite, the formation of this unique circular habit for NaCl or $NaCO_3$ warrants further investigation.

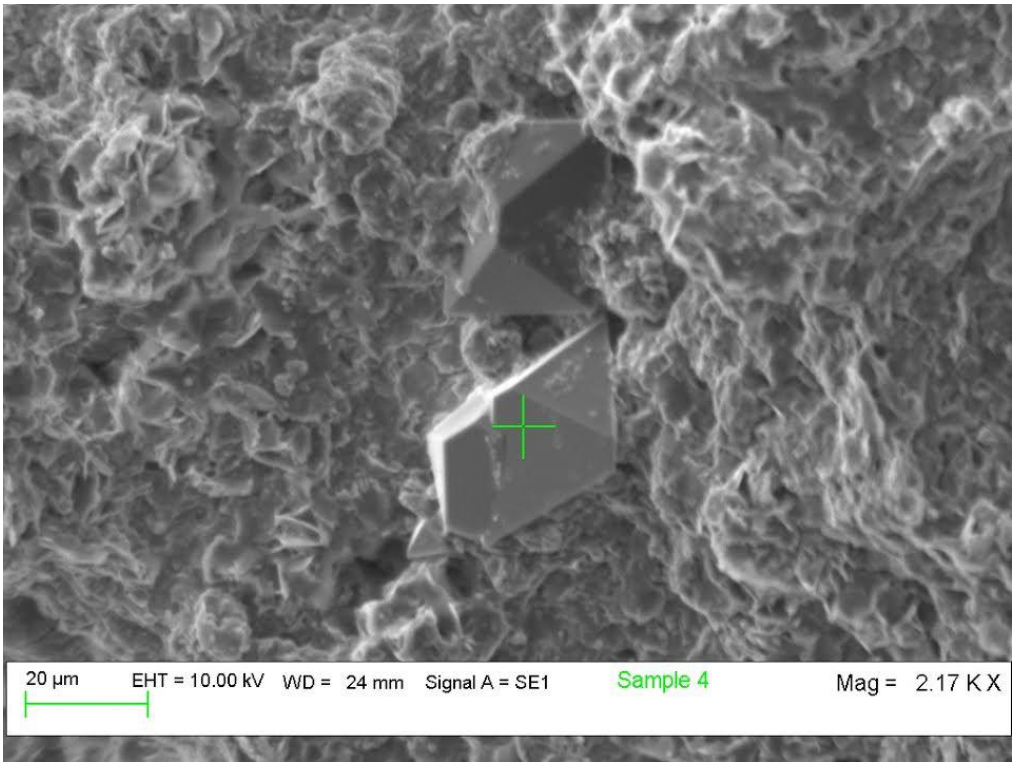

Figure 4-3 Unstable Calcium Carbonate Crystal

5 CONCLUSION

The following conclusions are derived from the research conducted on hand samples collected from the Lake Magadi South Kenya:

1) Lake Magadi (Group A) is characterized by very little authigenic clay (constitute with quartz, calcite) and more authigenic minerals (such as zeolites and zeolite-associated minerals) due to low precipitation, little vegetative cover and extreme alkalinity of ground water that recharge the lake. Bulk mineralogy is dominated by albite, sanidine, analcime, trona, halite and phillipsite. Clay analysis revealed the presence of erionite, moderite, montmorillionite, phillipsite.

2) The Olorgesailie area (Group B) is composed of weathered basalt clay and zeolites. These minerals are associated with more humid climate patterns and lake deposits. The area also can reflect changes in overall humid climate regime and might not reflect recent to modern climate patterns but reflect the Pleistocene humid period.

3) The Kiserian area (Group C) is characterized by similar bulk composition to the other sites, reflecting similar rift volcanism across the region. The mineralogy of detrital clay suggests more humid climate regime compare the other two localities. The diverse clay mineral assemblage as well as presence of kaolinite indicates intense weathering associated with more humid climate patterns.

To conclude, although the bulk mineralogy is the same on all localities due to similar volcaniclastics compositions throughout the Kenya Rift Valley, the clay mineralogy significantly differs between sample localities reflected different tectonic settings and climate regime. In humid climate at higher elevation detrital clay minerals dominate, whereas, in humid climate at higher elevation detrital clay minerals dominate. In the

transition region between higher elevation with detrital clay and lower elevation with authigenic clay, both detrital and authigenic minerals were present. The clay minerals are potentially useful as qualitative terrestrial climate proxies.

REFERENCE

Anjam, I., & Valdman, J. (2015). Fast MATLAB assembly of FEM matrices in 2D and 3D: Edge elements. *Applied Mathematics and Computation*, *267*, 252–263.

Ashman, M. R., Hallett, P. D., Brookes, P. C., & Allen, J. (2009). Evaluating soil stabilization by biological processes using step-wise aggregate fractionation. *Soil and Tillage Research*, *102*(2), 209–215.

Baker, B. H. (1976). Volcanic stratigraphy and geochronology of the Kedong-Olorgesailie area and the evolution of the South Kenya rift valley.

Baker, B. H. 1958, Geology of the Lake Magadi Area.

Baker, B. H., Williams, L. A. J., Miller, J. A., & Fitch, F. J. (1971). Sequence and geochronology of the Kenya rift volcanics. *Tectonophysics*, *11*(3), 191–215. http://doi.org/10.1016/0040-1951(71)90030-8

Ballabio, D. (2015). A MATLAB toolbox for Principal Component Analysis and unsupervised exploration of data structure. *Chemometrics and Intelligent Laboratory Systems*, *149, Part B*, 1–9. http://doi.org/10.1016/j.chemolab.2015.10.003

Bandura, L., Panek, R., Rotko, M., & Franus, W. (2016). Synthetic zeolites from fly ash for an effective trapping of BTX in gas stream. *Microporous and Mesoporous Materials*, *223*, 1–9. http://doi.org/10.1016/j.micromeso.2015.10.032

Bergaya, F., Theng, B. K. G, & Lagaly, G. (2011). *Handbook of Clay Science*. Elsevier.

Bish, D. L. (1993) Paleogeothermal and Paleohydrologic Conditions in Silicic Tuff from Yucca Mountain, Nevada. *Clays and Clay Minerals*, *41*(2), 148–161.

Blanc, P. Bourbon, X., Lassin, A., & Gaucher, E. C. (2010). Chemical model for cement-based materials: Temperature dependence of thermodynamic functions for nanocrystalline and

crystalline C–S–H phases. *Cement and Concrete Research*, *40*(6), 851–866. http://doi.org/10.1016/j.cemconres.2009.12.004

Cammelli, S., Degueldre, C., Cervellino, A., Abolhassani, S., Kuri, G., Bertsch, J., Frahm, R. (2010). Cluster formation, evolution and size distribution in Fe–Cu alloy: Analysis by XAFS, XRD and TEM. *Nuclear Instruments and Methods in Physics Research Section B: Beam Interactions with Materials and Atoms*, *268*(6), 632–637. http://doi.org/10.1016/j.nimb.2009.12.008

Cole, W. F., & Lancucki, C. J. (1983). Products formed in an aged concrete the occurrence of okenite. *Cement and Concrete Research*, *13*(5), 611–618. http://doi.org/10.1016/0008-8846(83)90049-2

Creeper, N. L., Hicks, W. S., Shand, P., & Fitzpatrick, R. W. (2015). Geochemical processes following freshwater reflooding of acidified inland acid sulfate soils: An in situ microcosm experiment. *Chemical Geology*, *411*, 200–214.

Dawson, J. B. (2008a). *The Gregory Rift Valley and Neogene-recent Volcanoes of Northern Tanzania*. Geological Society of London.

Deocampo, D. M. (2004). Hydrogeochemistry in the Ngorongoro Crater, Tanzania, and implications for land use in a World Heritage Site. *Applied Geochemistry*, *19*(5), 755–767.

Deocampo, D. M. (2015). Authigenic clay minerals in lacustrine mudstones.

Deocampo, D. M., Blumenschine, R. J., & Ashley, G. M. (2002). Wetland Diagenesis and Traces of Early Hominids, Olduvai Gorge, Tanzania. *Quaternary Research*, *57*(2), 271–281.

Deocampo, D. M., & Jones, B. F. (2014). 7.13 - Geochemistry of Saline Lakes. In H. D. H. K. Turekian (Ed.), *Treatise on Geochemistry (Second Edition)* (pp. 437–469). Oxford: Elsevier. Retrieved from

Oliveira, M. M., Fernandes, M. M., Fonseca, M. G., da Silva Filho, E. C., de Souza, A. G., Gaslain, F., & Jaber, M. (2014). Direct grafting of ethylene sulfide onto silicic acid magadiite. *Microporous and Mesoporous Materials*, *196*, 292–299. http://doi.org/10.1016/j.micromeso.2014.05.010

Eugster, H. P. (1980a). Chapter 15 Lake Magadi, Kenya, and Its Precursors1. In A. Nissenbaum (Ed.), *Developments in Sedimentology* (Vol. 28, pp. 195–232). Elsevier. Retrieved from http://www.sciencedirect.com/science/article/pii/S0070457108702395

Eugster, H. P. (1980b). Chapter 15 Lake Magadi, Kenya, and Its Precursors1. In A. Nissenbaum (Ed.), *Developments in Sedimentology* (Vol. 28, pp. 195–232). Elsevier. Retrieved from http://www.sciencedirect.com/science/article/pii/S0070457108702395

Eugster, H. P. (1986). Lake Magadi, Kenya: a model for rift valley hydrochemistry and sedimentation? *Geological Society, London, Special Publications*, *25*(1), 177–189. http://doi.org/10.1144/GSL.SP.1986.025.01.15

Firoozi, A. A., Taha, M. R., Firoozi, A. A., & Khan, T. A. (2015). Effect of ultrasonic treatment on clay microfabric evaluation by atomic force microscopy. *Measurement*, *66*, 244–252. http://doi.org/10.1016/j.measurement.2015.02.033

Follett, E. (1965). Chemical dissolution techniques in the study of soil clays*: Part I* (Vol. 1).

Fristensky, A., & Grismer, M. E. (2008). A simultaneous model for ultrasonic aggregate stability assessment. *CATENA*, *74*(2), 153–164. http://doi.org/10.1016/j.catena.2008.04.013

Frost, R. L., & Xi, Y. (2012a). Vibrational spectroscopic study of the minerals nekoite Ca3Si6O15·7H2O and okenite Ca10Si18O46·18H2O – Implications for the molecular structure. *Journal of Molecular Structure*, *1020*, 96–104.

Glenn, R. C., Jackson, M. L., Hole, F. D., & Lee, G. B. (1960). Chemical Weathering of Layer Silicate Clays in Loess-derived Tama silt loam of southwestern Wisconsin. In A. Swineford (Ed.), *Clays and Clay Minerals* (pp. 63–83). Pergamon. Retrieved from

Guo, X., Yoshino, T., & Shimojuku, A. (2015). Electrical conductivity of albite–(quartz)–water and albite–water–NaCl systems and its implication to the high conductivity anomalies in the continental crust. *Earth and Planetary Science Letters*, *412*, 1–9. http://doi.org/10.1016/j.epsl.2014.12.021

Guthrie, G. D., & Carey, J. W. (2015a). A thermodynamic and kinetic model for paste–aggregate interactions and the alkali–silica reaction. *Cement and Concrete Research*, *76*, 107–120.

Guthrie, G. D., & Carey, J. W. (2015b). A thermodynamic and kinetic model for paste–aggregate interactions and the alkali–silica reaction. *Cement and Concrete Research*, *76*, 107–120. http://doi.org/10.1016/j.cemconres.2015.05.004

Hradil, D., Bezdička, P., Hradilová, J., & Vašutová, V. (1950). Microanalysis of clay-based pigments in paintings by XRD techniques. *Microchemical Journal*. http://doi.org/10.1016/j.microc.2015.10.032

Hypersaline brines and evaporitic environments: Proceedings of the Bat Sheva Seminar on Saline Lakes and Natural Brines. (2011). Elsevier.

Iannicelli-Zubiani, E. M., Cristiani, C., Dotelli, G., Gallo Stampino, P., Pelosato, R., Mesto, E., Lacalamita, M. (2015). Use of natural clays as sorbent materials for rare earth ions:

Materials characterization and set up of the operative parameters. *Waste Management*. http://doi.org/10.1016/j.wasman.2015.09.017

Ingebritsen, S. E., Sanford, W. E., & Neuzil, C. E. (2006). *Groundwater in Geologic Processes*. Cambridge University Press.

Jackson, M. L. (1974). Clay Water Diagenesis During Burial: How Mud Becomes Gneiss. *Marine Chemistry*, *2*(4), 317.

Jackson, M. L. (1979). The Chemistry of Clay Minerals. *Marine Chemistry*, *2*(4), 317–318. http://doi.org/10.1016/0304-4203(74)90027-9

Jasiewicz, K., Cieslak, J., Kaprzyk, S., & Tobola, J. (2015). Relative crystal stability of AlxFeNiCrCo high entropy alloys from XRD analysis and formation energy calculation. *Journal of Alloys and Compounds*, *648*, 307–312. http://doi.org/10.1016/j.jallcom.2015.06.260

Jones, B. F., and Deocampo, D. M. (2003). 5.13 - Geochemistry of Saline Lakes. In H. D. H. K. Turekian (Ed.), *Treatise on Geochemistry* (pp. 393–424). Oxford: Pergamon. Retrieved from http://www.sciencedirect.com/science/article/pii/B0080437516050830

Jones, B. F., Eugster, H. P., & Rettig, S. L. (1977). Hydrochemistry of the Lake Magadi basin, Kenya. *Geochimica et Cosmochimica Acta*, *41*(1), 53–72. http://doi.org/10.1016/0016-7037(77)90186-7

Klint, S. E., & Elliott, W. (2000). Coexisting altered glass and Fe^Ni oxides at the Cretaceous Tertiary boundary (Vols. 1–182). 127-136.

Kodikara, G. R. L., Woldai, T., van Ruitenbeek, F. J. A., Kuria, Z., van der Meer, F., Shepherd, K. D., & van Hummel, G. J. (2012). Hyperspectral remote sensing of evaporate minerals and associated sediments in Lake Magadi area, Kenya. *International Journal of Applied*

Earth Observation and Geoinformation, *14*(1), 22–32. http://doi.org/10.1016/j.jag.2011.08.009

Konnerup-Madsen, J. (1979). Fluid inclusions in quartz from deep-seated granitic intrusions, south Norway. *Lithos*, *12*(1), 13–23. http://doi.org/10.1016/0024-4937(79)90058-6

Kuria, Z. N., Woldai, T., Meer, F. D. van der, & Barongo, J. O. (2010a). Active fault segments as potential earthquake sources: Inferences from integrated geophysical mapping of the Magadi fault system, southern Kenya Rift. *Journal of African Earth Sciences*, *57*(4), 345–359. http://doi.org/10.1016/j.jafrearsci.2009.11.004

Kuria, Z. N., Woldai, T., Meer, F. D. van der, & Barongo, J. O. (2010b). Active fault segments as potential earthquake sources: Inferences from integrated geophysical mapping of the Magadi fault system, southern Kenya Rift. *Journal of African Earth Sciences*, *57*(4), 345–359. http://doi.org/10.1016/j.jafrearsci.2009.11.004

Lake Magadi slowly choking. (2015a, October 11). Retrieved October 11, 2015, from http://www.nation.co.ke/lifestyle/DN2/Lake-Magadi-slowly-choking--/-/957860/2798804

Lee, R. K. L., Owen, R. B., Renaut, R. W., Behrensmeyer, A. K., Potts, R., & Sharp, W. D. (2013). Facies, geochemistry and diatoms of late Pleistocene Olorgesailie tufas, southern Kenya Rift. *Palaeogeography, Palaeoclimatology, Palaeoecology*, *374*, 197–217.

Mahadi, M. I., & Palaniandy, S. (2010). Mechanochemical effect of dolomitic talc during fine grinding process in mortar grinder. *International Journal of Mineral Processing*, *94*(3–4), 172–179.

McCarthy, D. W., Mark, J. E., Clarson, S. J., & Schaefer, D. W. (1998). Synthesis, structure, and properties of hybrid organic–inorganic composites based on polysiloxanes. II. Comparisons between poly(methylphenylsiloxane) and poly(dimethylsiloxane), and between titania and

silica. Journal of Polymer Science Part B: Polymer Physics, 36(7), 1191–1200. http://doi.org/10.1002/(SICI) 1099-0488(199805)36:7<1191::AID-POLB8>3.0.CO;2-X

Mees, F. (2010). 22 - Authigenic Silicate Minerals – Sepiolite-Palygorskite, Zeolites and Sodium Silicates. In G. Stoops, V. Marcelino, & F. Mees (Eds.), *Interpretation of Micromorphological Features of Soils and Regoliths* (pp. 497–520). Amsterdam: Elsevier.

Mikhail, E., & Briner, G. (1978). Routine particle size analysis of soils using sodium hypochlorite and ultrasonic dispersion. *Soil Research, 16*(2), 241–244.

Milcius, D., Grbović-Novaković, J., Zostautienė, R., Lelis, M., Girdzevicius, D., & Urbonavicius, M. (2015). Combined XRD and XPS analysis of ex-situ and in-situ plasma hydrogenated magnetron sputtered Mg films. *Journal of Alloys and Compounds, 647,* 790–796.

Mirwald, P. W., & Massonne, H.-J. (1980). The low-high quartz and quartz-coesite transition to 40 kbar between 600° and 1600°C and some reconnaissance data on the effect of NaAlO2 component on the low quartz-coesite transition. *Journal of Geophysical Research: Solid Earth*, *85*(B12), 6983–6990.

Moore, D., & Reynolds, R. (1997). X-Ray Diffraction and the Identification and Analysis of Clay Minerals.

Nielsen, J. M. (1999). East African Magadi (trona): fluoride concentration and mineralogical composition. *Journal of African Earth Sciences*, *29*(2), 423–428.

North, P. F. (1976). Towards an Absolute Measurement of Soil Structural Stability Using Ultrasound. Journal of Soil Science, 27(4), 451–459. http://doi.org/10.1111/j.1365-2389.1976.tb02014.x

Olapade, A. A., & Umeonuorah, U. C. (2014). Chemical and Sensory Evaluation of African Breadfruit (Treculia africana) Seeds Processed with Alum and Trona. *Nigerian Food Journal*, *32*(1), 80–88.

Owen, R. B., Renaut, R. W., Scott, J. J., Potts, R., & Behrensmeyer, A. K. (2009). Wetland sedimentation and associated diatoms in the Pleistocene Olorgesailie Basin, southern Kenya Rift Valley. *Sedimentary Geology*, *222*(1–2), 124–137.

Perchuk, L. L., & Kushiro, I. (2013). *Physical Chemistry of Magmas*. Springer Science & Business Media.

Peterson, K., Gress, D., Van Dam, T., & Sutter, L. (2006). Crystallized alkali-silica gel in concrete from the late 1890s. *Cement and Concrete Research*, *36*(8), 1523–1532.

Potter, R. M., & Rossman, G. R. (1979). The manganese- and iron-oxide mineralogy of desert varnish. *Chemical Geology*, *25*(1–2), 79–94. http://doi.org/10.1016/0009-2541(79)90085-8

Reimer, L. (1984). Transmission Electron Microscopy, Physics of Image Formation and Microanalysis, Springer Ser. Opt. Sci., Vol. 36 (Springer, Berlin, Heidelberg 1984)

Russell, J., & Cohen, A. (2012). g in the East African Rift Lakes.

Simiyu, S. M., & Randy Keller, G. (1998). Upper crustal structure in the vicinity of Lake Magadi in the Kenya Rift Valley region. *Journal of African Earth Sciences*, *27*(3–4), 359–371. http://doi.org/10.1016/S0899-5362(98)00068-2

Środoń, J. (2013). Chapter 2.2 - Identification and Quantitative Analysis of Clay Minerals. In F. B. and G. Lagaly (Ed.), *Developments in Clay Science* (Vol. 5, pp. 25–49). Elsevier. Retrieved from http://www.sciencedirect.com/science/article/pii/B9780080982595000044

Środoń, J., Drits, V. A., McCarty, D. K., Hsieh, J. C. C., & Eberl, D. D. (2001). Quantitative X-Ray Diffraction Analysis of Clay-Bearing Rocks from Random Preparations. *Clays and Clay Minerals*, *49*(6), 514–528.

Sun, K., Lu, J., Ma, L., Han, Y., Fu, Z., & Ding, J. (2015). A comparative study on the catalytic performance of different types of zeolites for biodiesel production. *Fuel*, *158*, 848–854.

Taboada, T., Rodríguez-Lado, L., Ferro-Vázquez, C., Stoops, G., & Martínez Cortizas, A. (2016). Chemical weathering in the volcanic soils of Isla Santa Cruz (Galápagos Islands, Ecuador). *Geoderma*, *261*, 160–168. http://doi.org/10.1016/j.geoderma.2015.07.019

Thirumalini, S., Ravi, R., Sekar, S. K., & Nambirajan, M. (2015). Knowing from the past – Ingredients and technology of ancient mortar used in Vadakumnathan temple, Tirussur, Kerala, India. *Journal of Building Engineering*, *4*, 101–112.

Uchic, M. D., Groeber, M. A., Dimiduk, D. M., & Simmons, J. P. (2006). 3D microstructural characterization of nickel superalloys via serial-sectioning using a dual beam FIB-SEM. *Scripta Materialia*, *55*(1), 23–28.

Vidal, N. C., & Volzone, C. (2009). Analysis of tetramethylammonium–montmorillonite and retention of toluene from aqueous solution. *Applied Clay Science*, *45*(4), 227–231.

Warren, J. K. (2014). 13.22 - Geochemistry of Evaporite Ores in an Earth-Scale Climatic and Tectonic Framework. In H. D. H. K. Turekian (Ed.), *Treatise on Geochemistry (Second Edition)* (pp. 569–593). Oxford: Elsevier. Retrieved from http://www.sciencedirect.com/science/article/pii/B9780080959757011256

X-Ray Diffraction and the Identification and Analysis of Clay Minerals. (1997) (2 edition). Oxford ; New York: Oxford University Press.

APPENDIX

Appendix A XRD Bulk Results patterns

Appendix B XRD Clay Results patterns

Appendix D SEM-EDS Results

Appendix A XRD Bulk Results

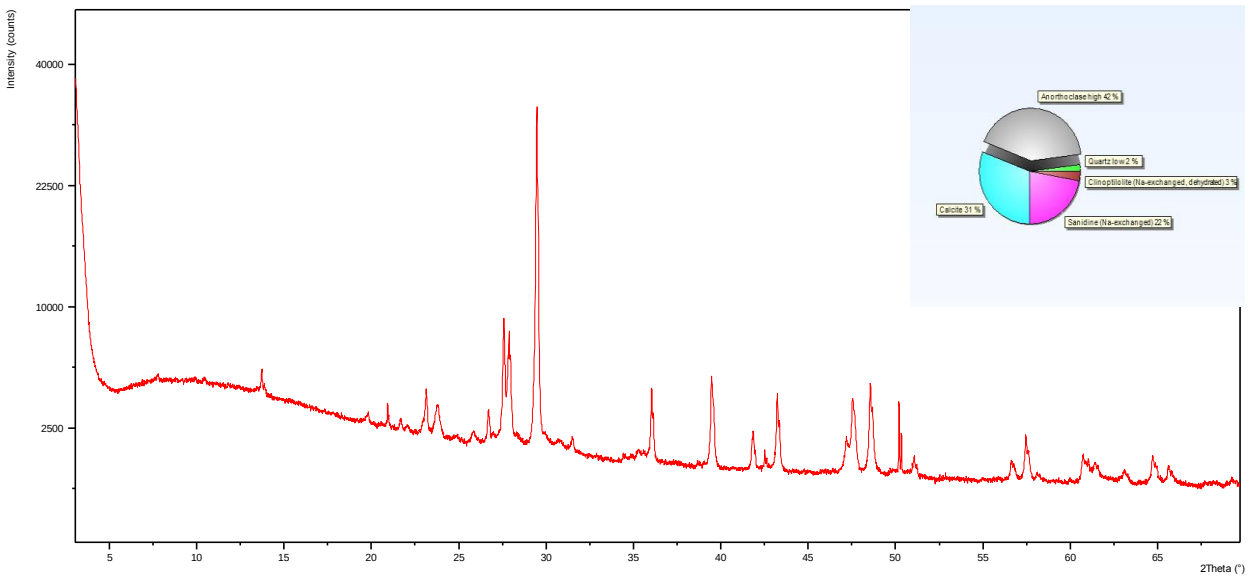

XRD Bulk Sample # 1

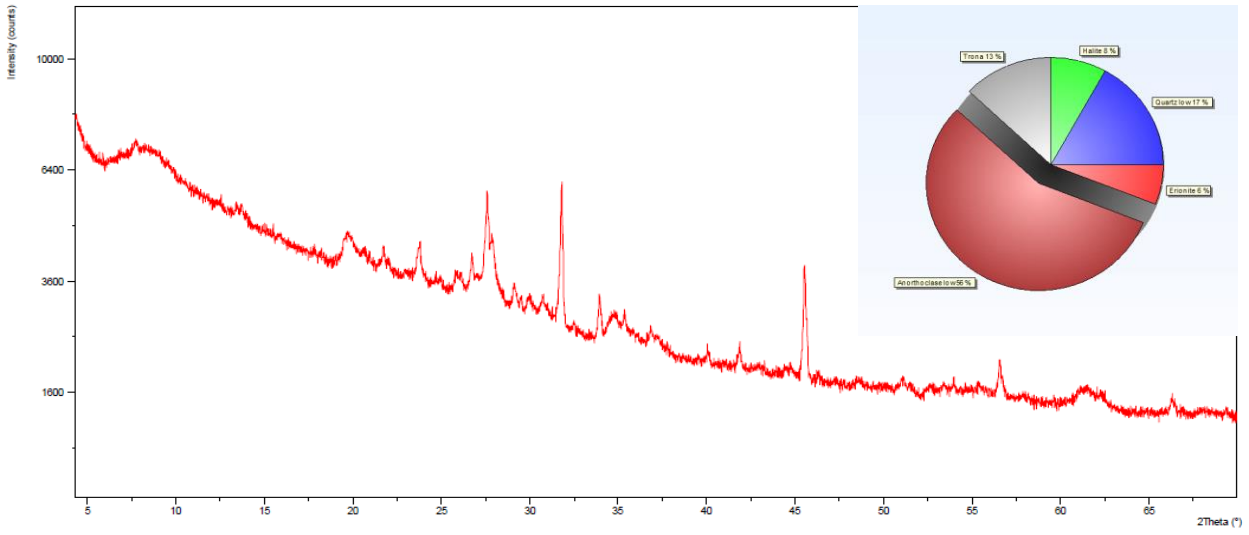

XRD Bulk Sample # 2

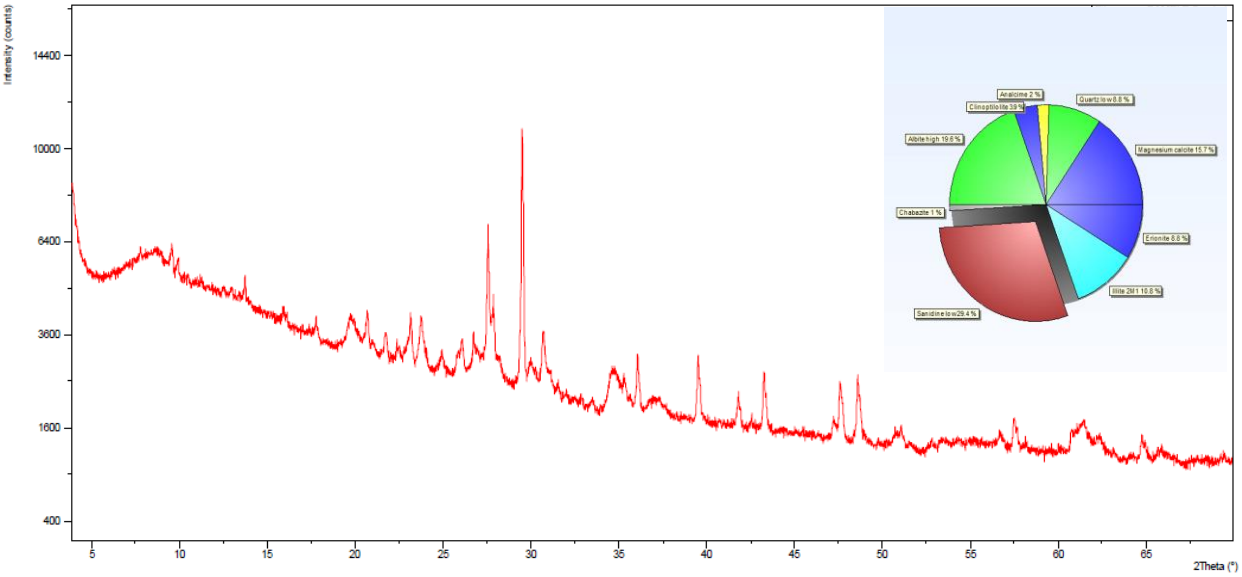

XRD Bulk Sample # 3

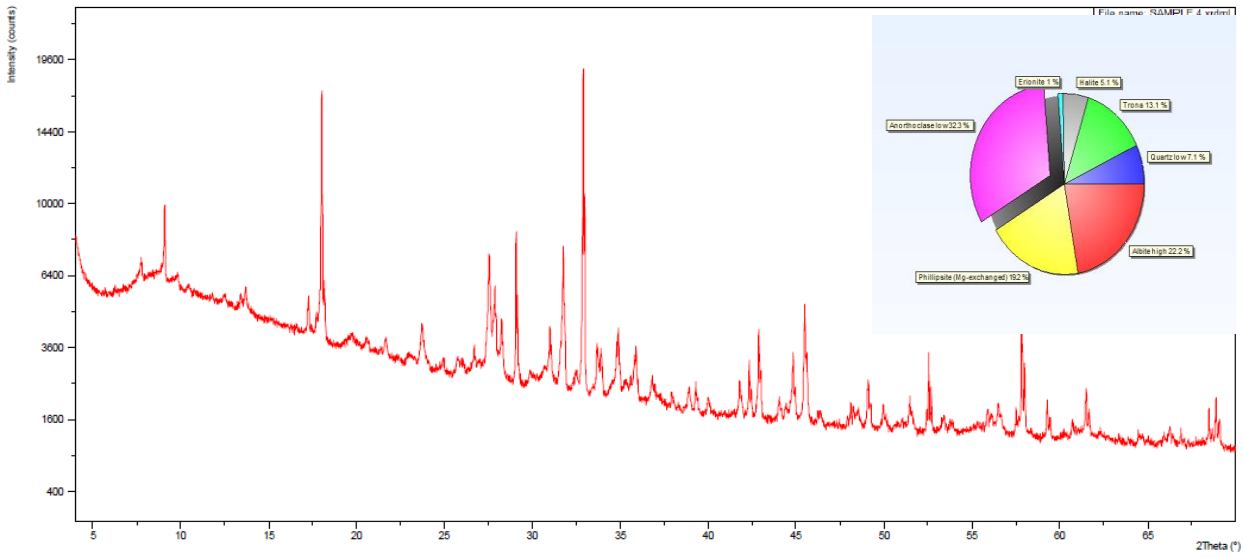

XRD Bulk Sample # 4

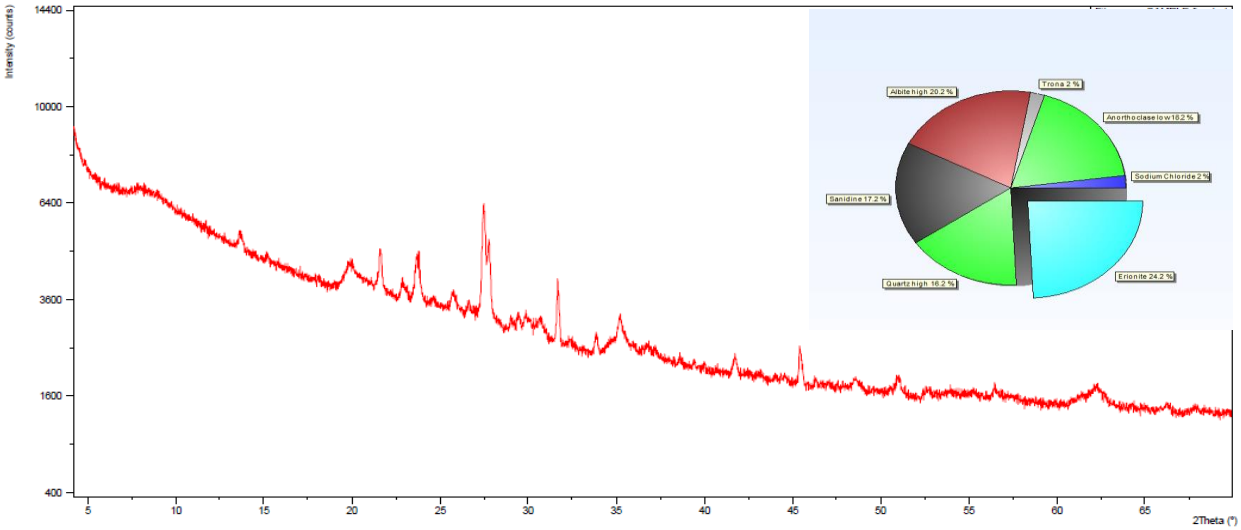

XRD Bulk Sample # 5

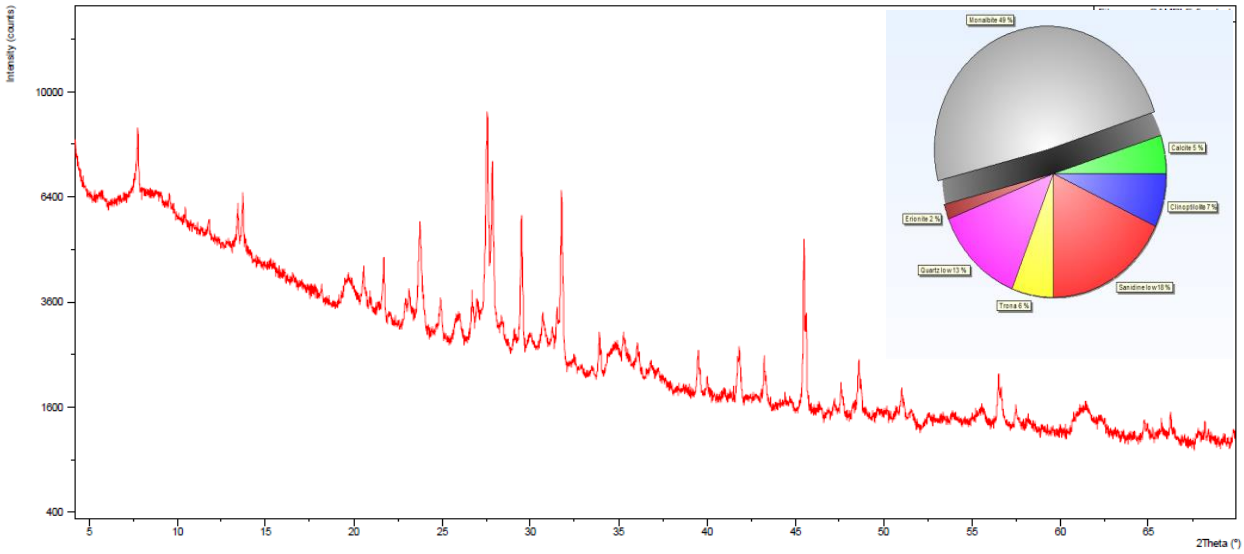

XRD Bulk Sample # 6

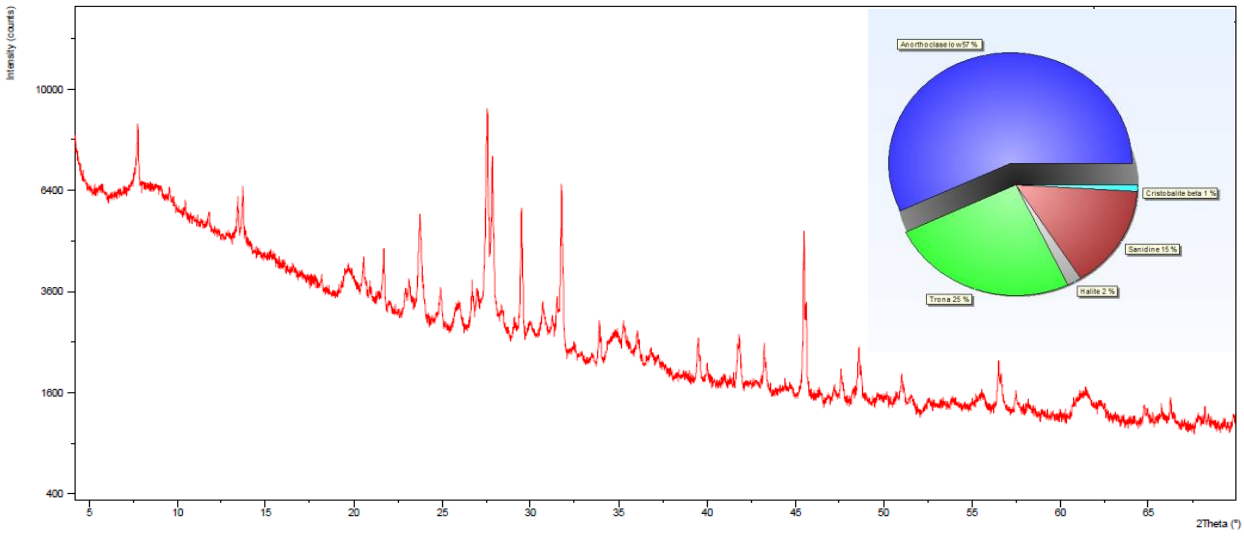

XRD Bulk Sample # 7

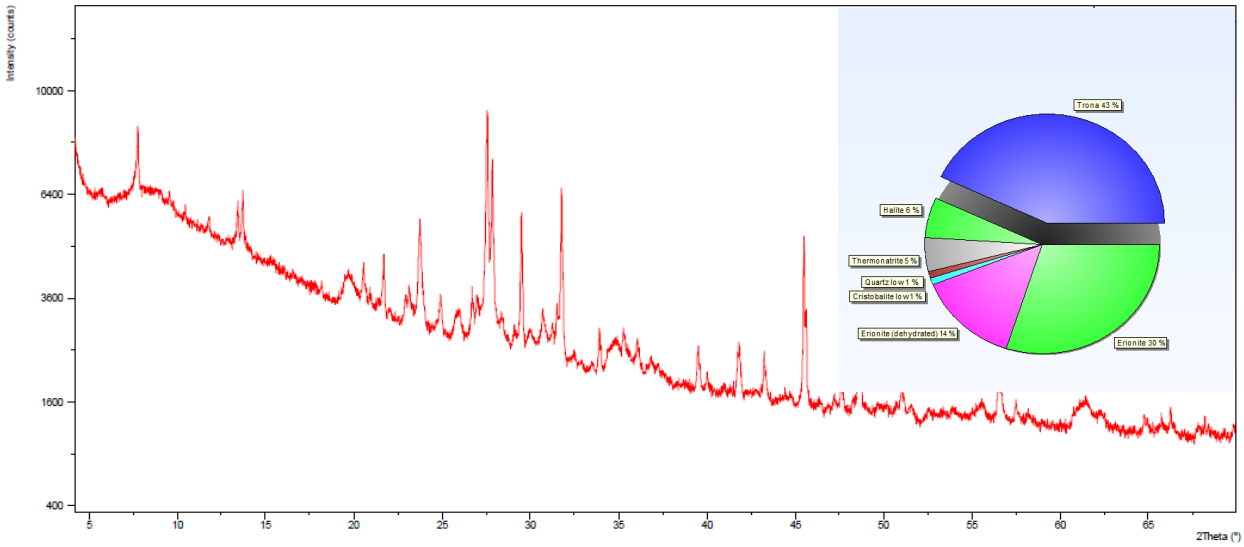

XRD Bulk Sample # 8

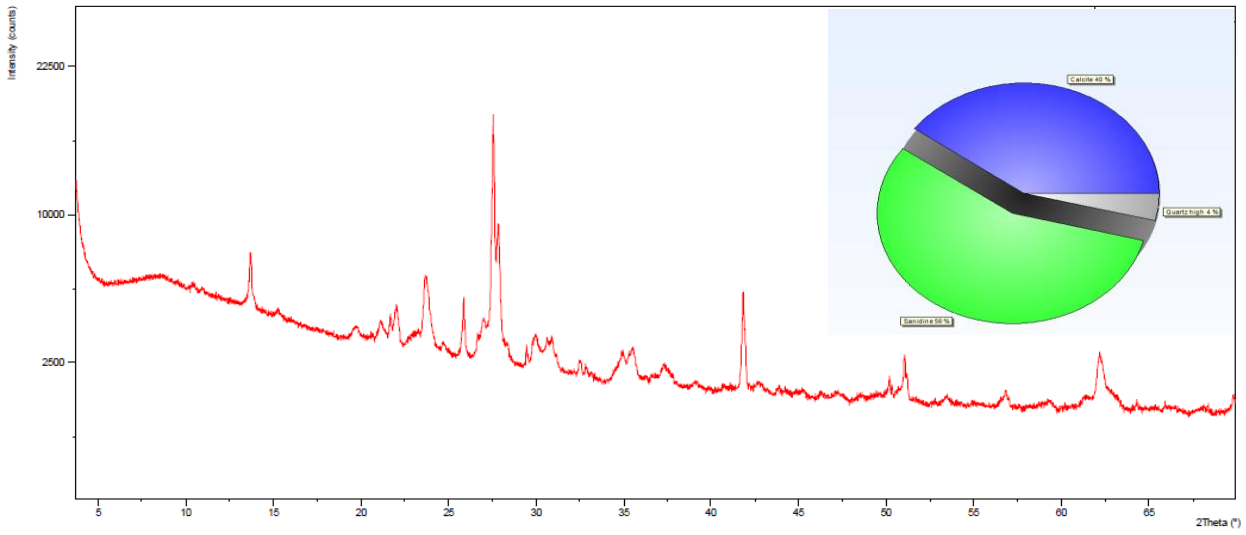

XRD Bulk Sample # 9

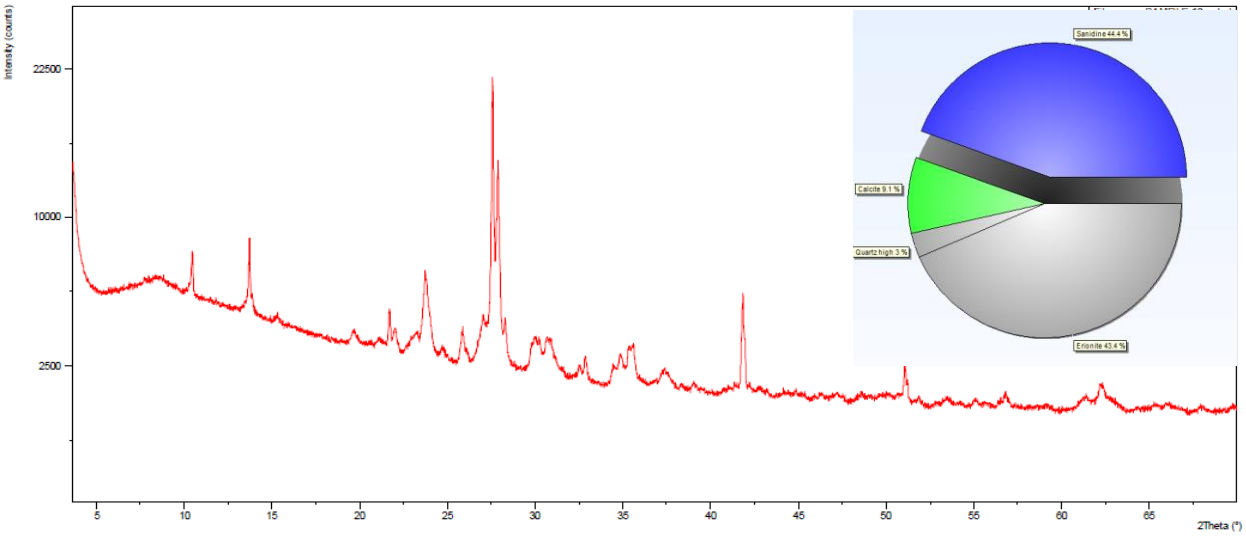

XRD Bulk Sample # 10

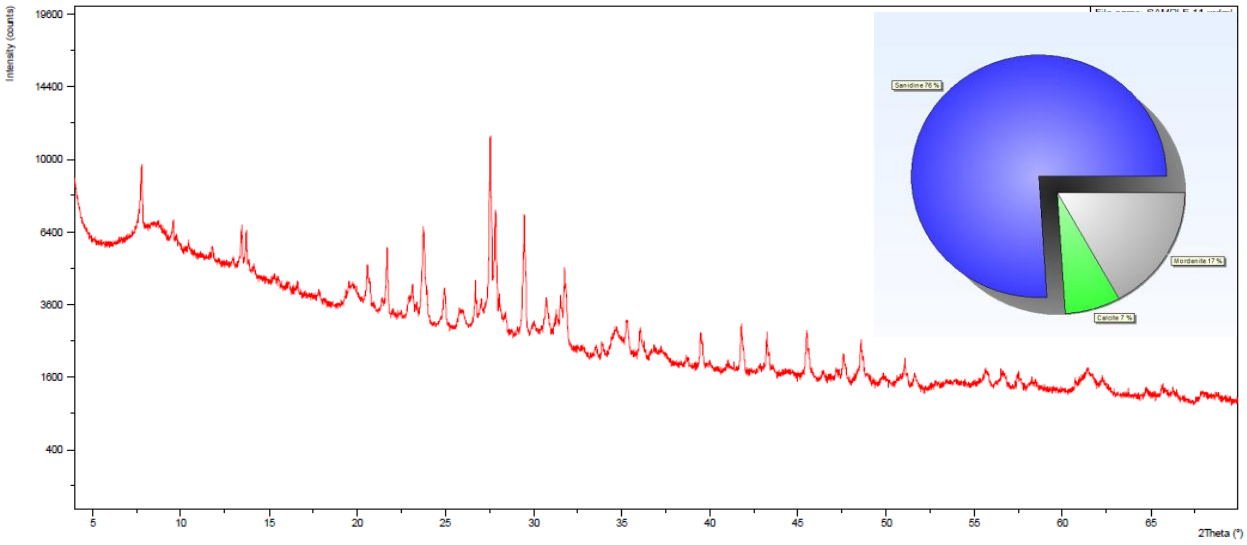

XRD Bulk Sample # 11

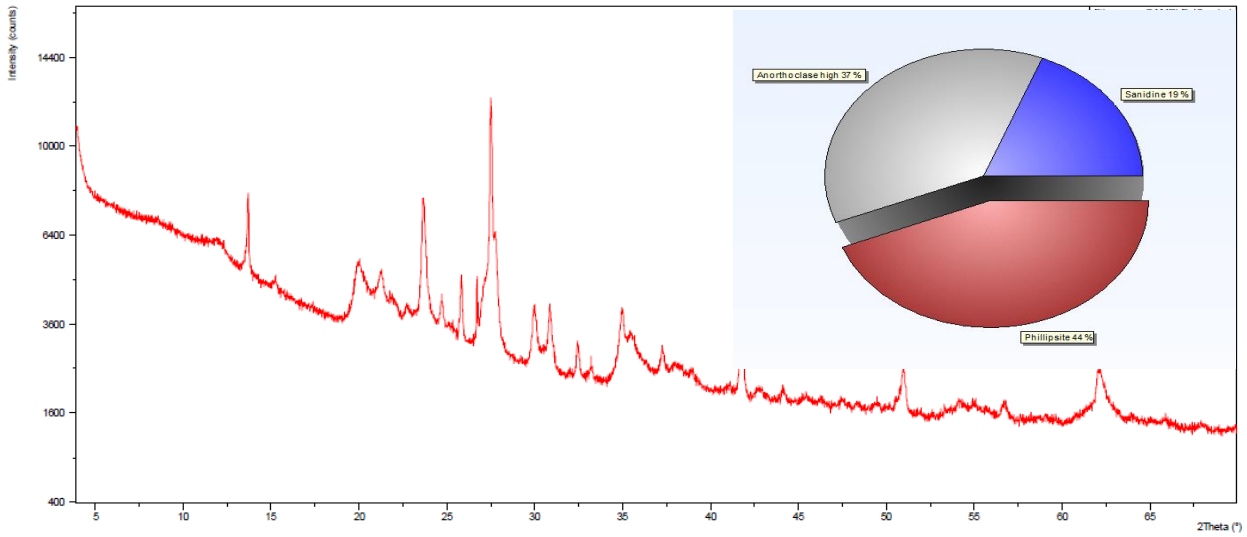

XRD Bulk Sample # 12

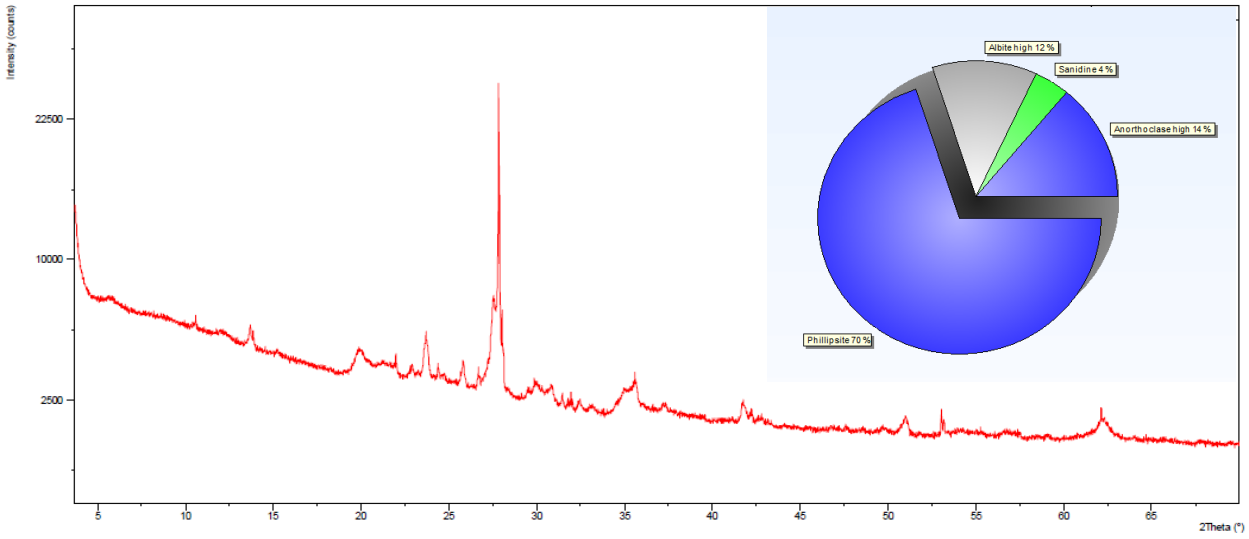

XRD Bulk Sample # 13

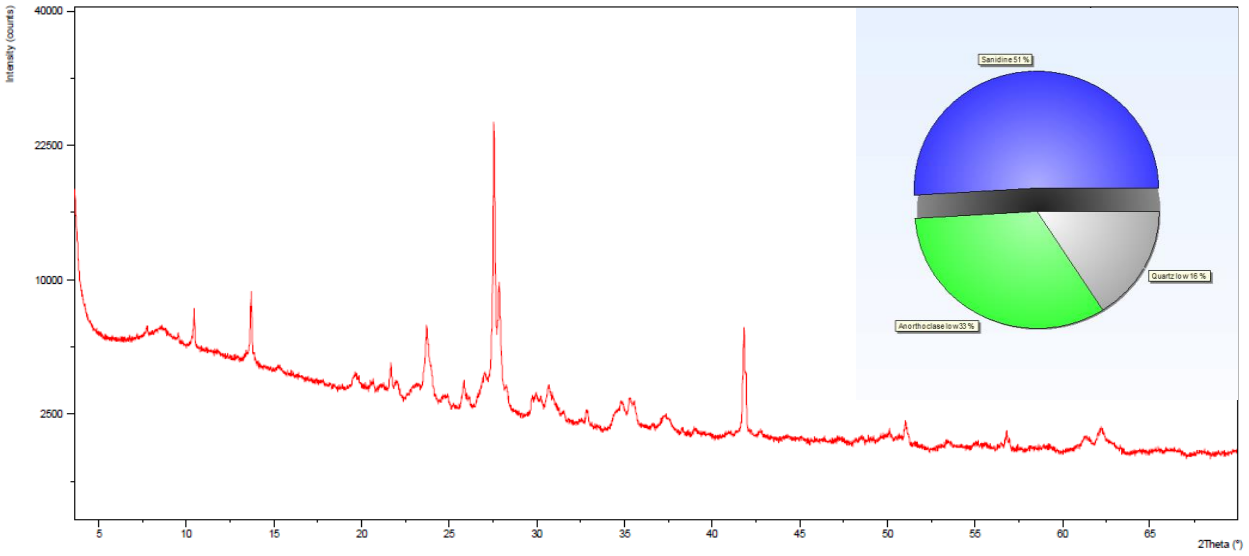

XRD Bulk Sample # 14

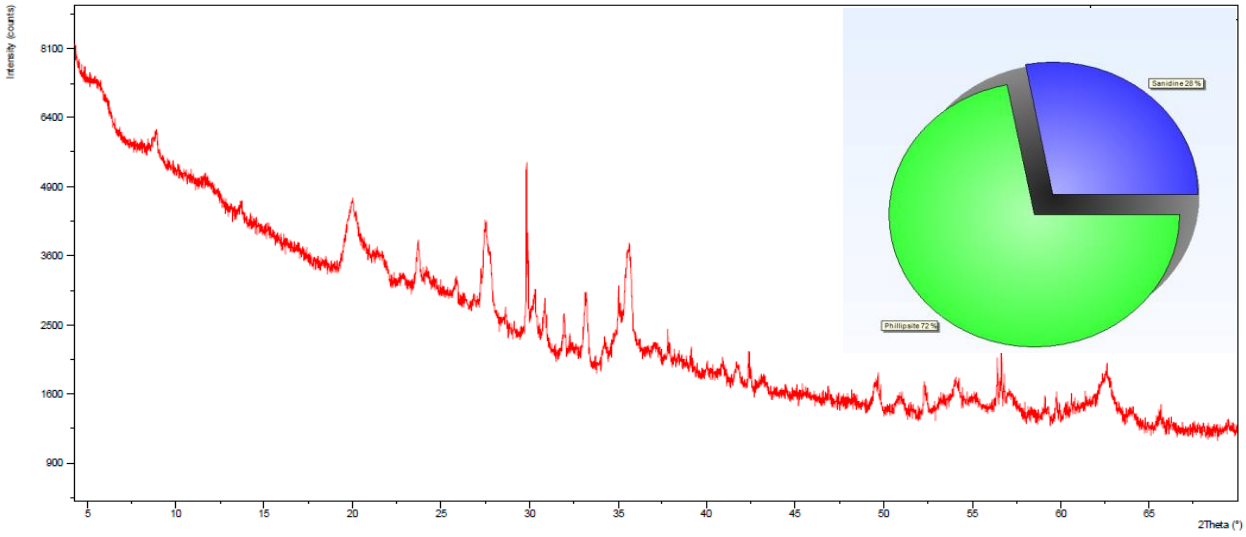

XRD Bulk Sample # 15

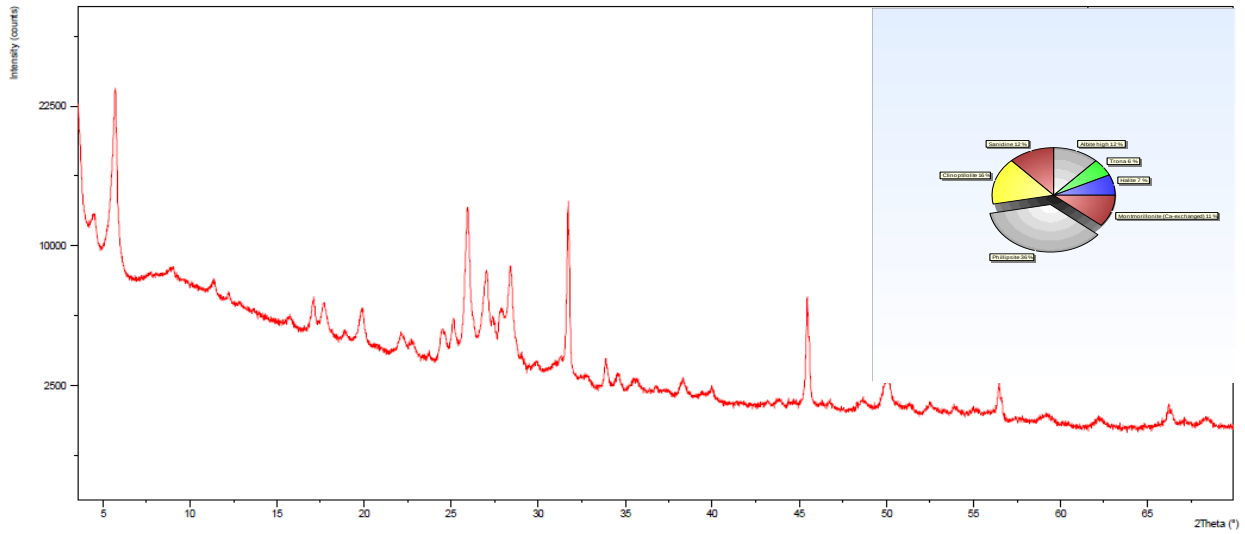

XRD Bulk Sample # 16

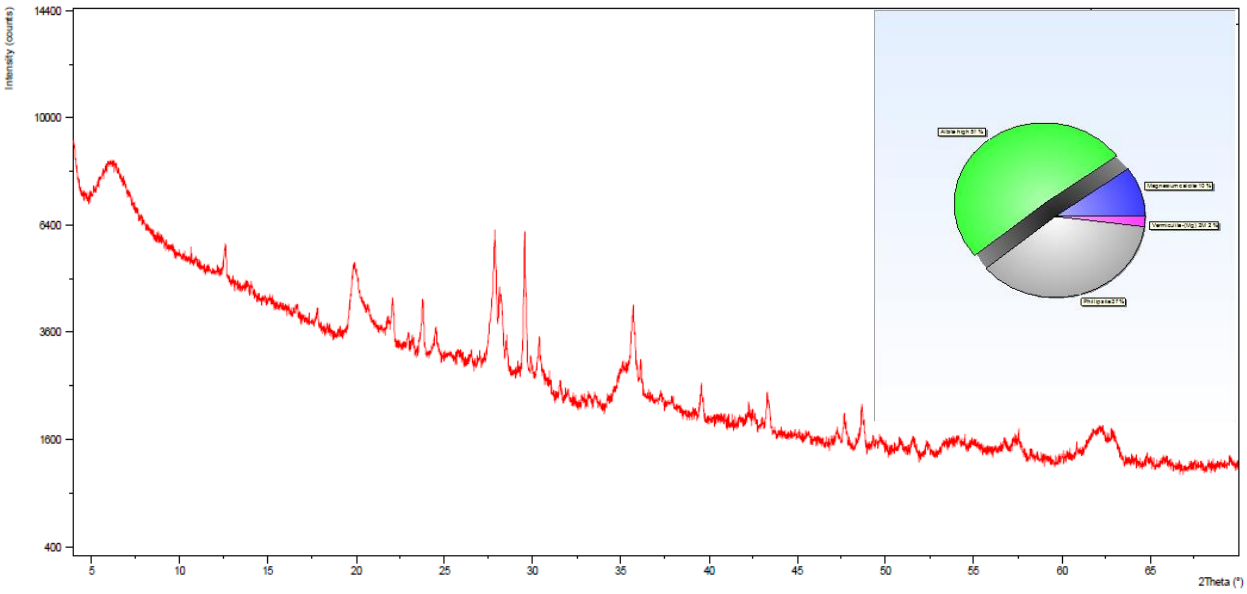

XRD Bulk Sample # 17

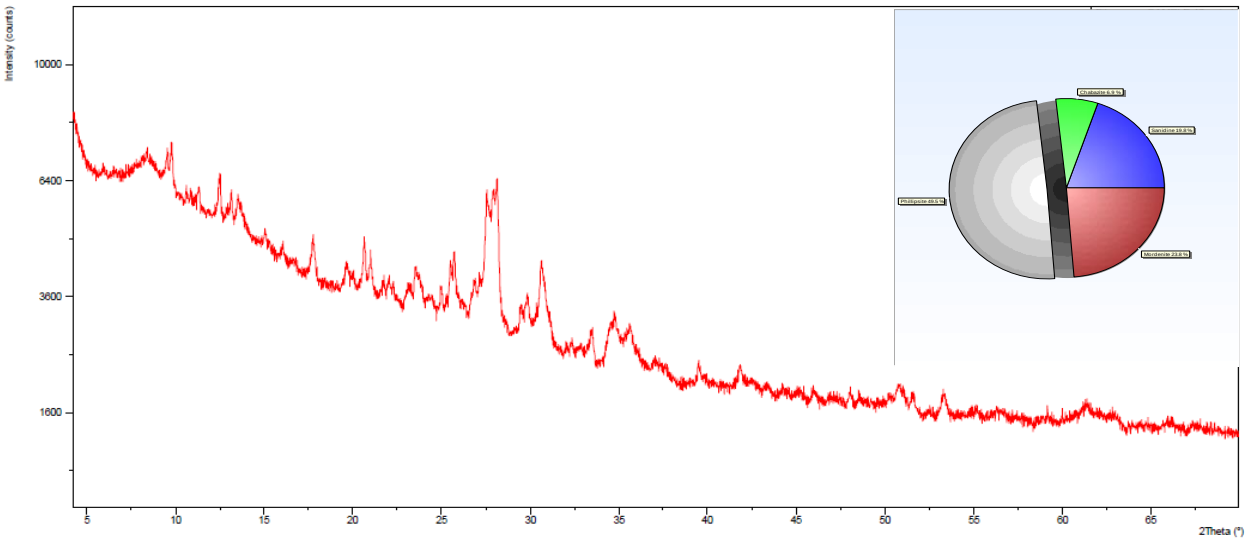

XRD Bulk Sample # 18

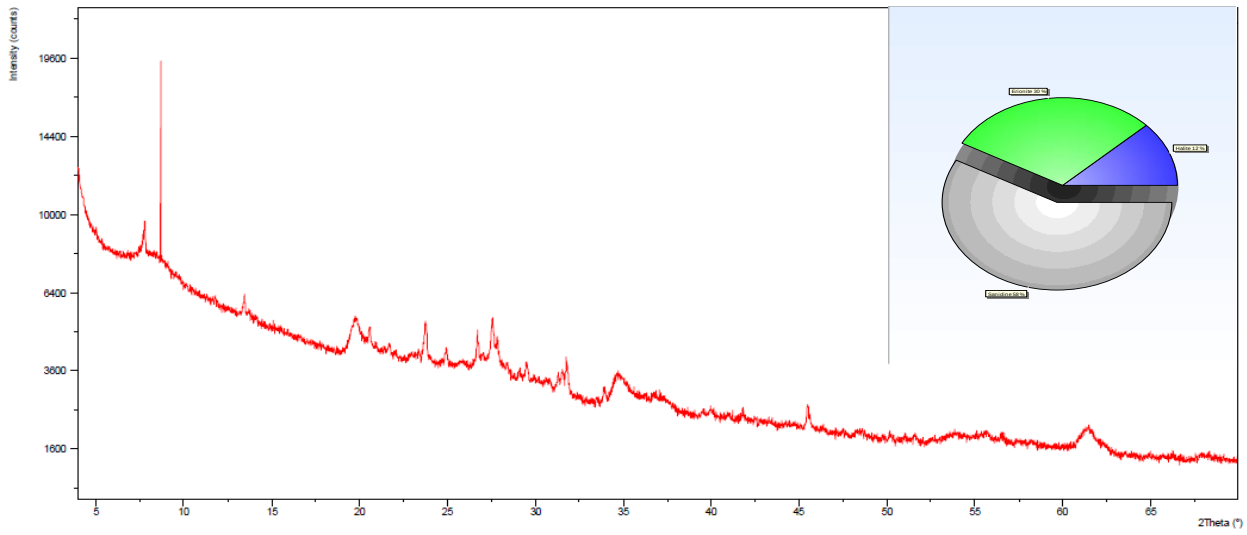

XRD Bulk Sample # 19

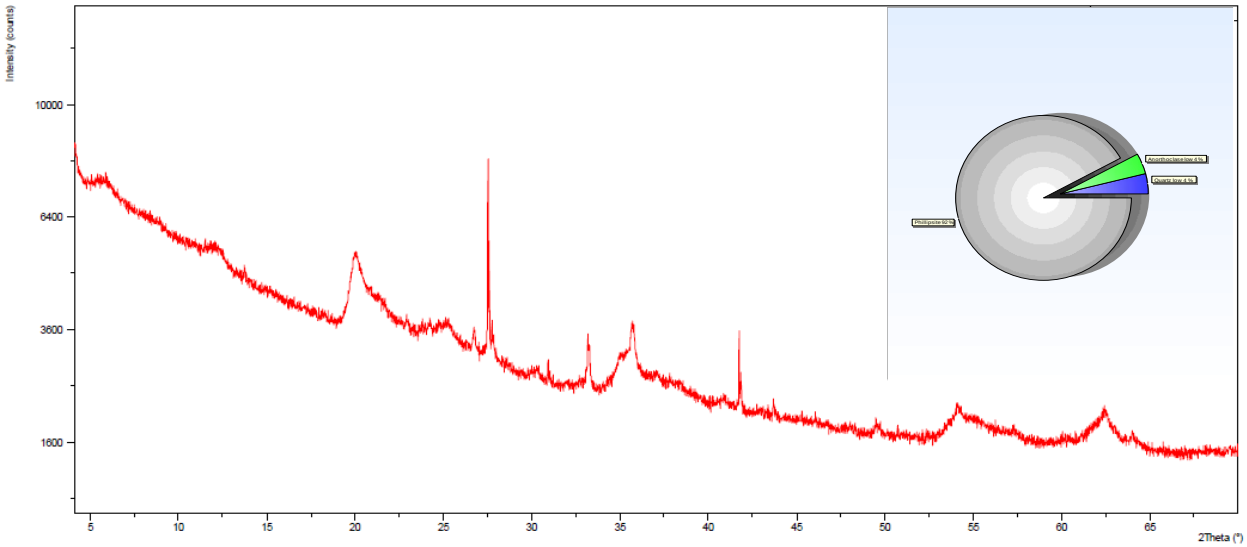

XRD Bulk Sample # 20

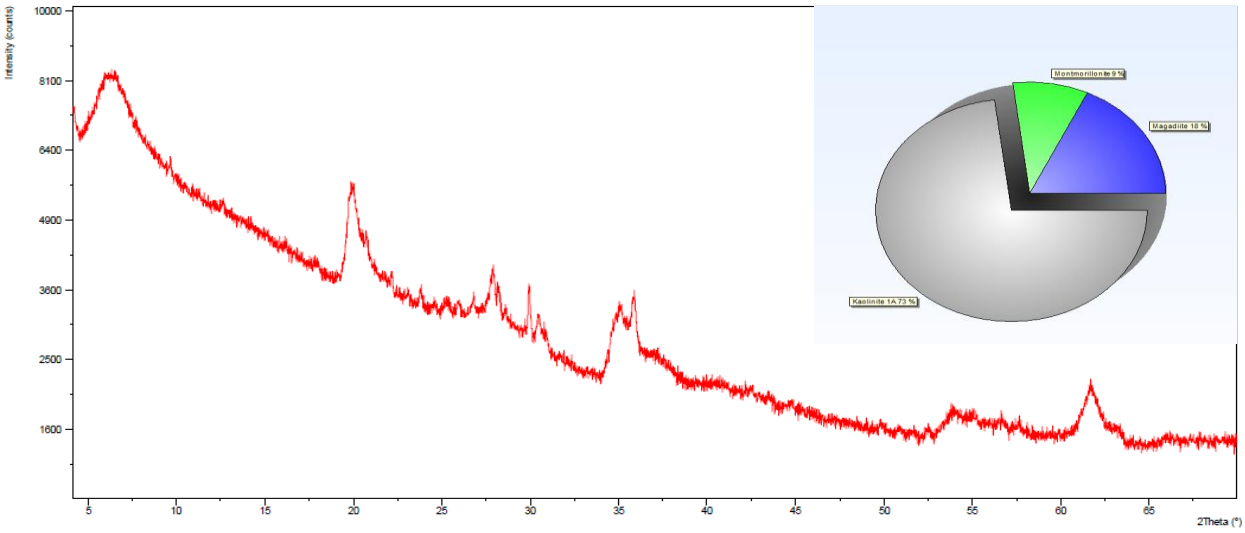

XRD Bulk Sample # 21

Appendix B XRD Clay Results

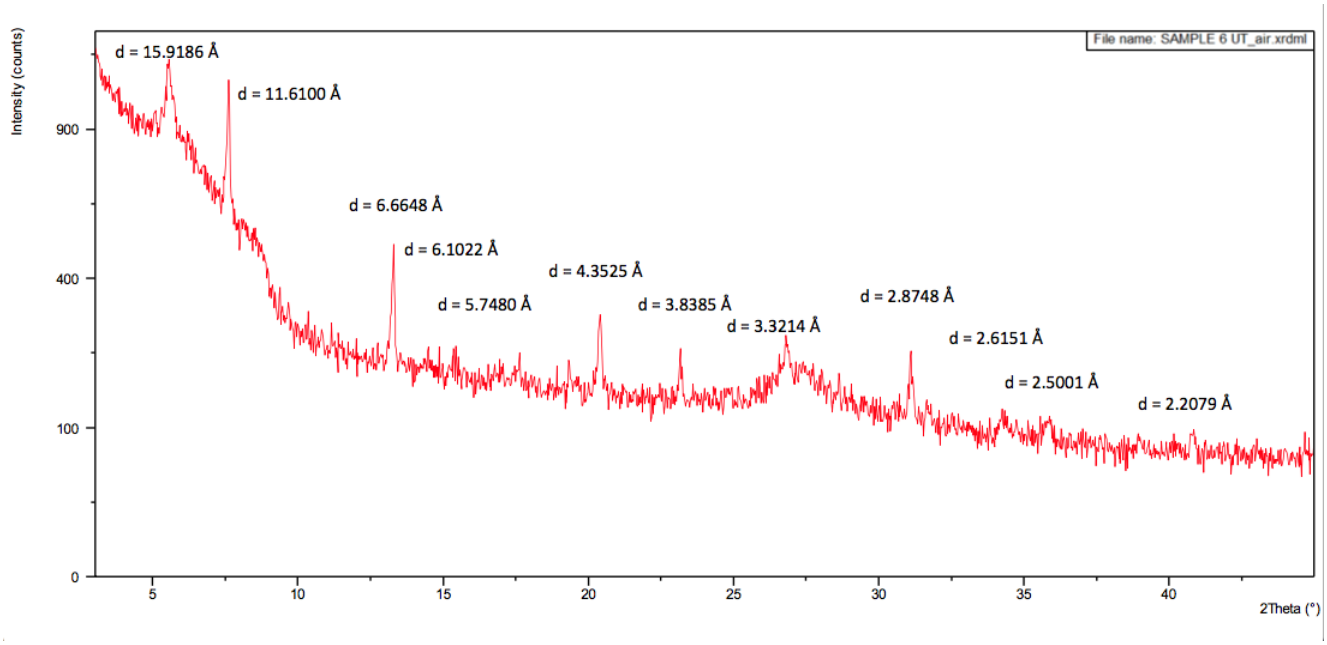

XRD Clay Results 1 Sample # 6

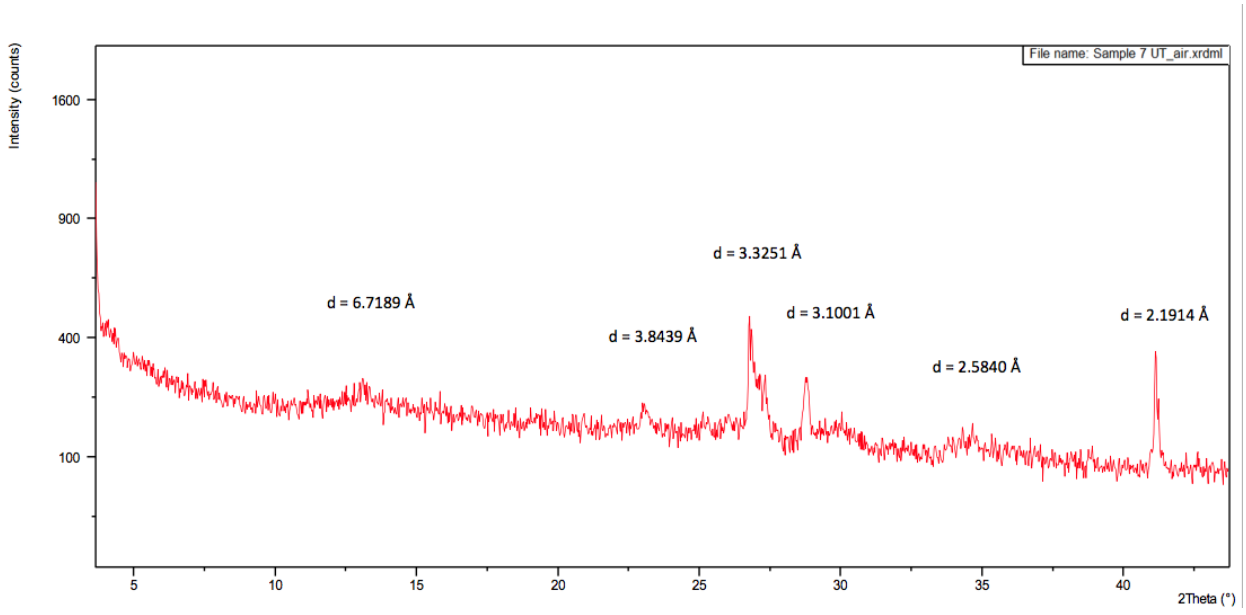

XRD Clay Results 2 Sample # 7

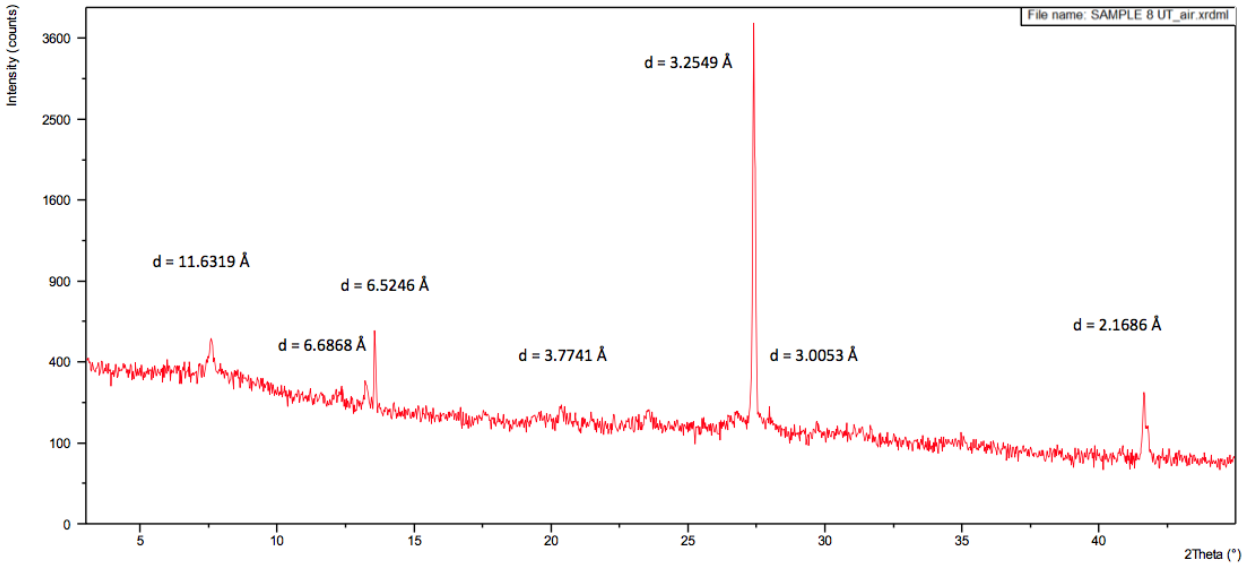

XRD Clay Results 3 Sample # 8

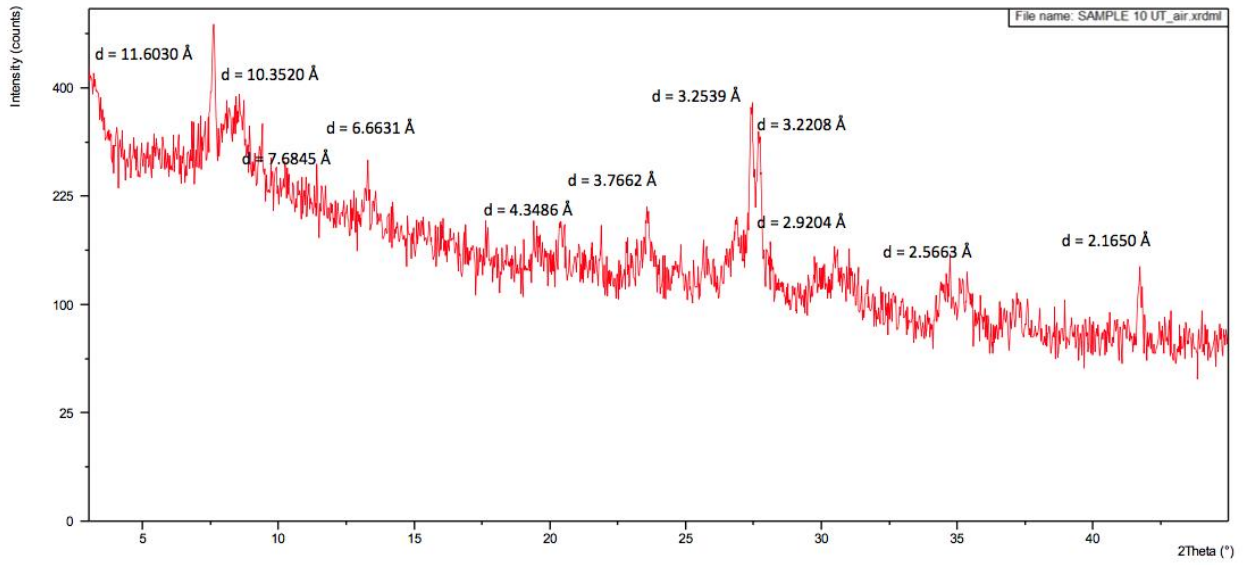

XRD Clay Results 4 Sample # 10

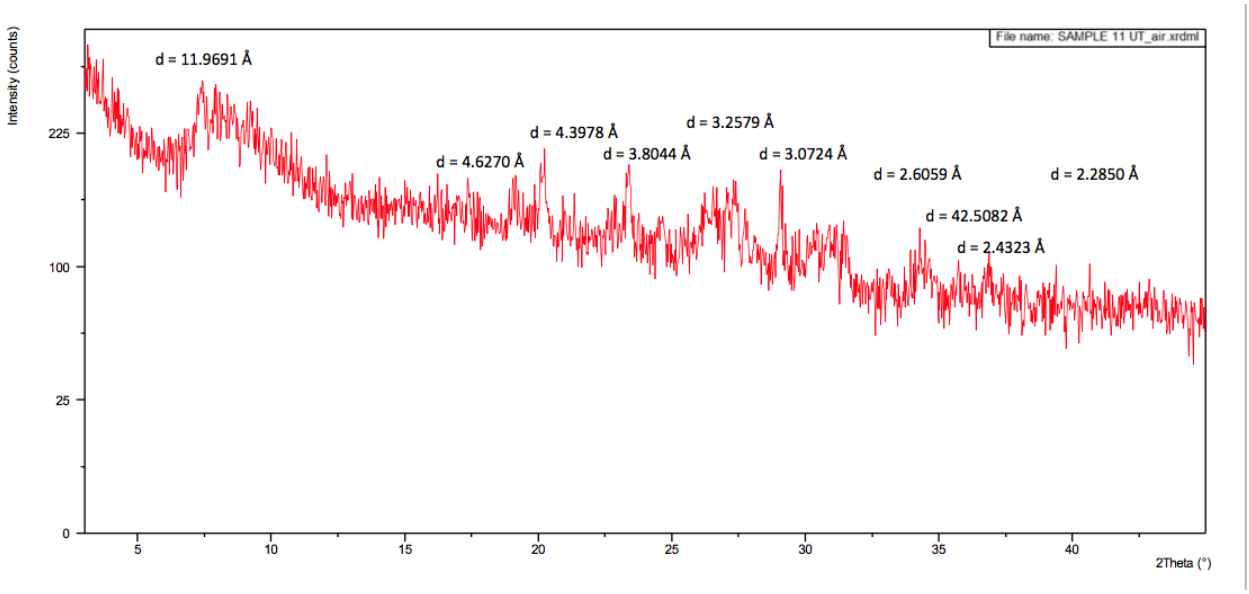

XRD Clay Results 5 Sample # 11

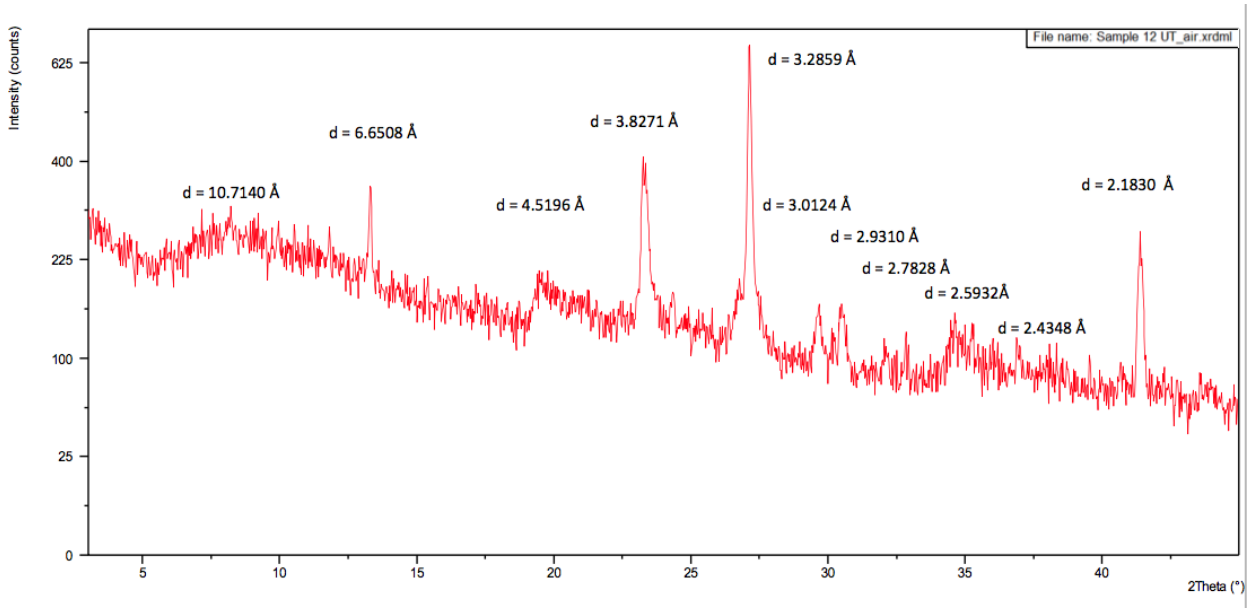

XRD Clay Results 6 Sample # 12

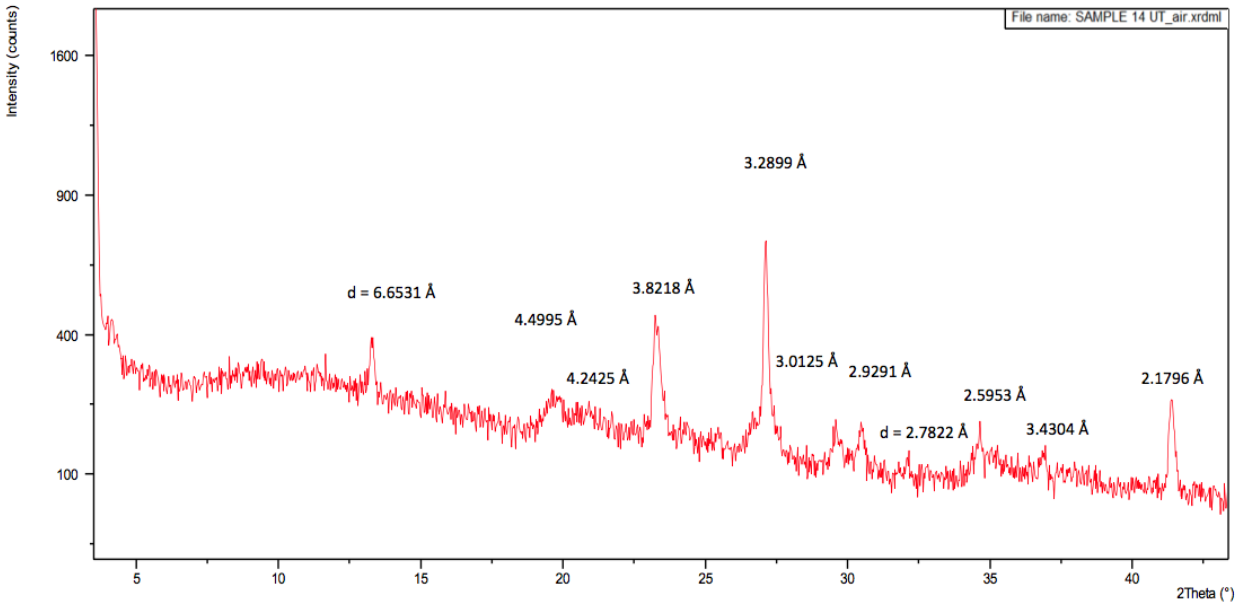

XRD Clay Results 7 Sample # 14

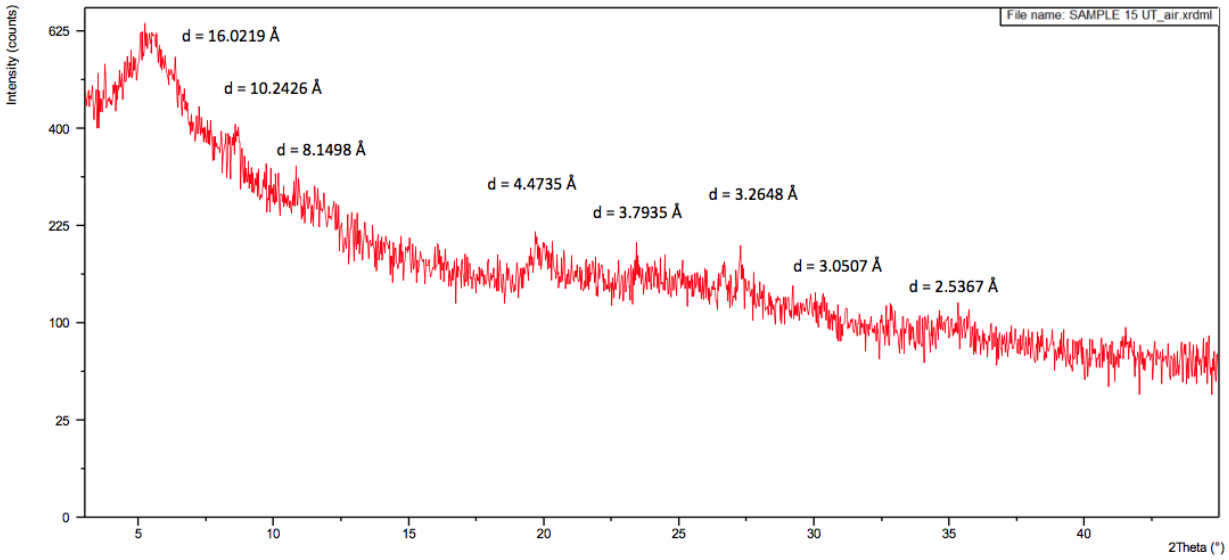

XRD Clay Results 8 Sample # 15

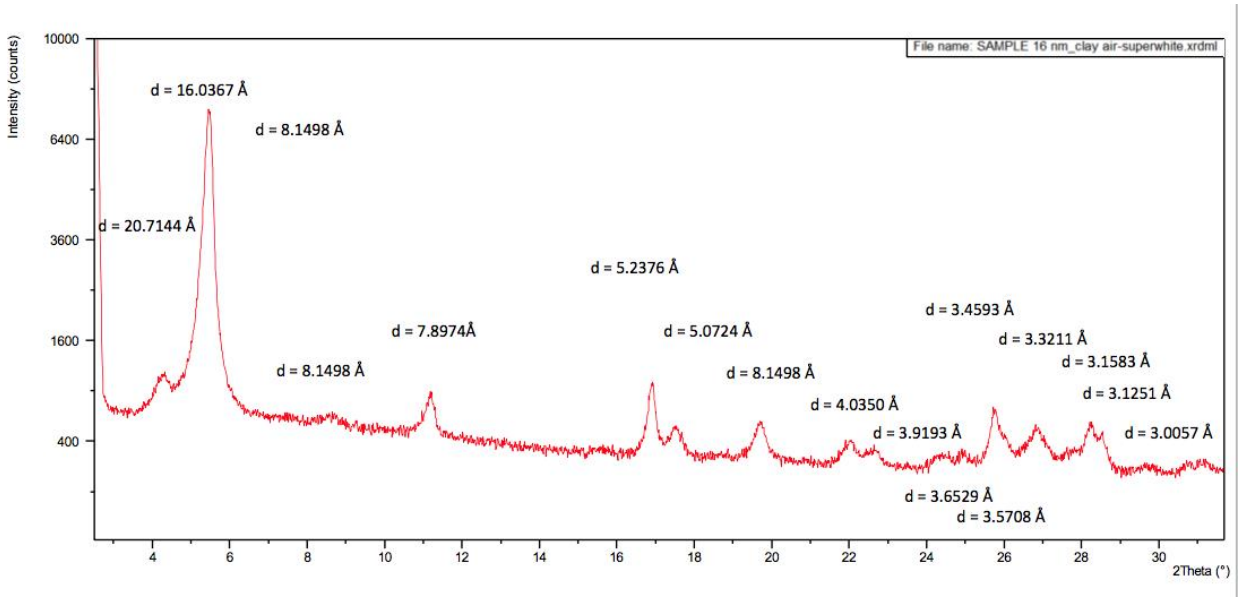

XRD Clay Results 9 Sample # 16

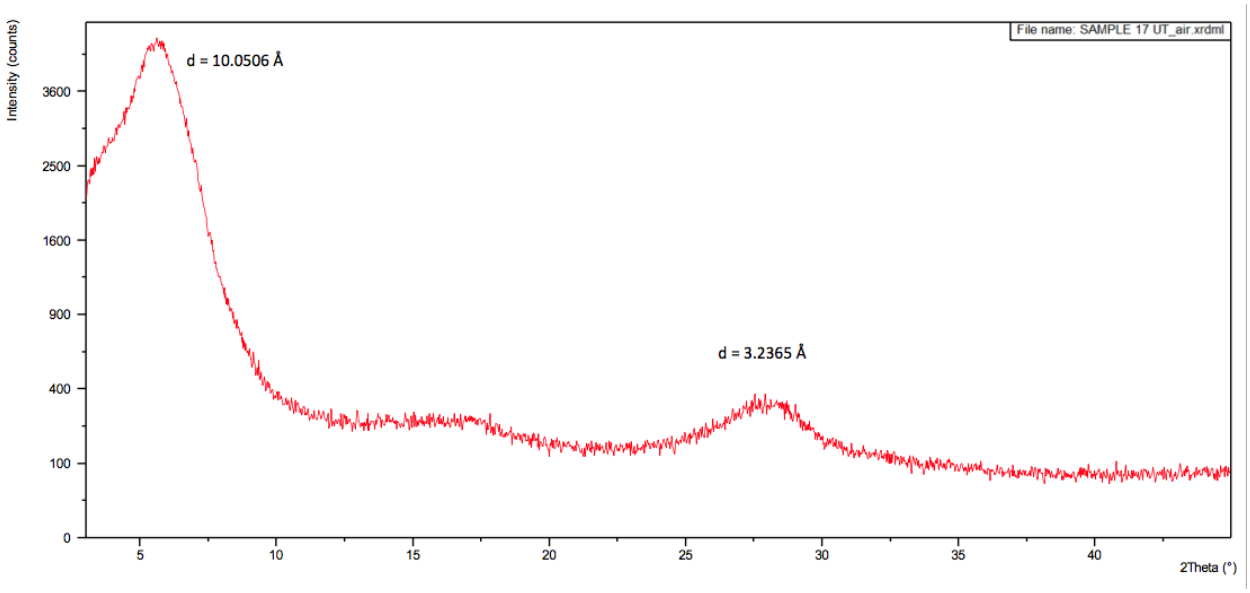

XRD Clay Results 10 Sample # 17

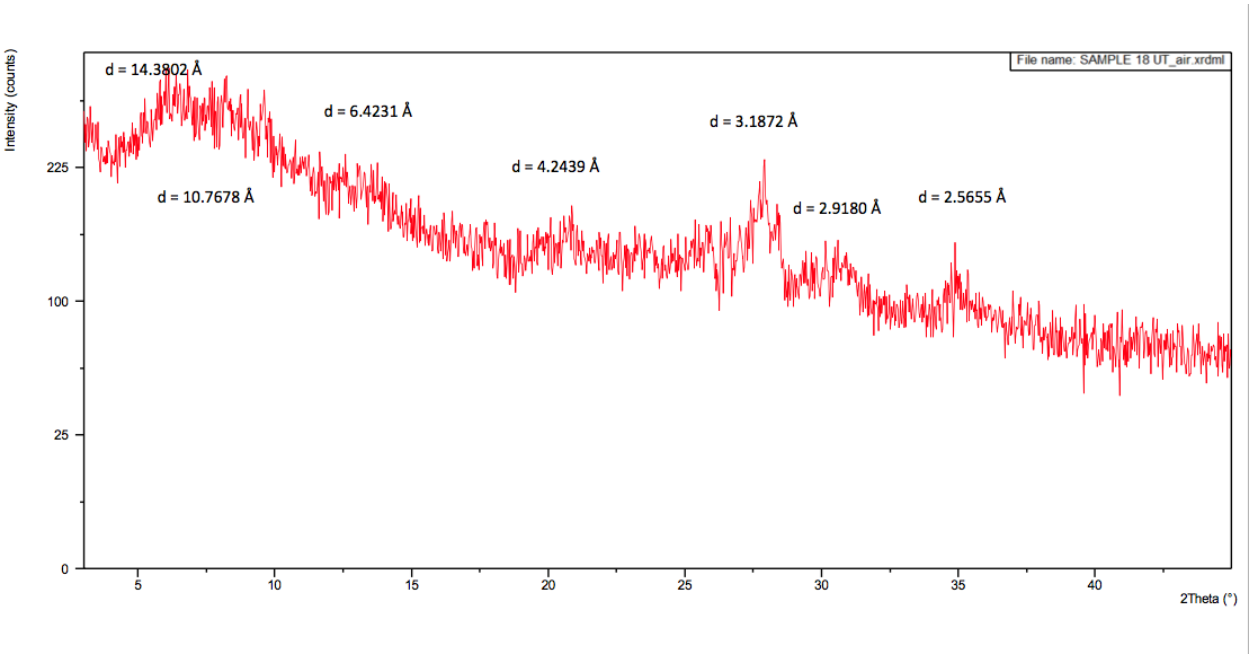

XRD Clay Results 11 Sample # 18

Appendix D SEM images and chemical analysis

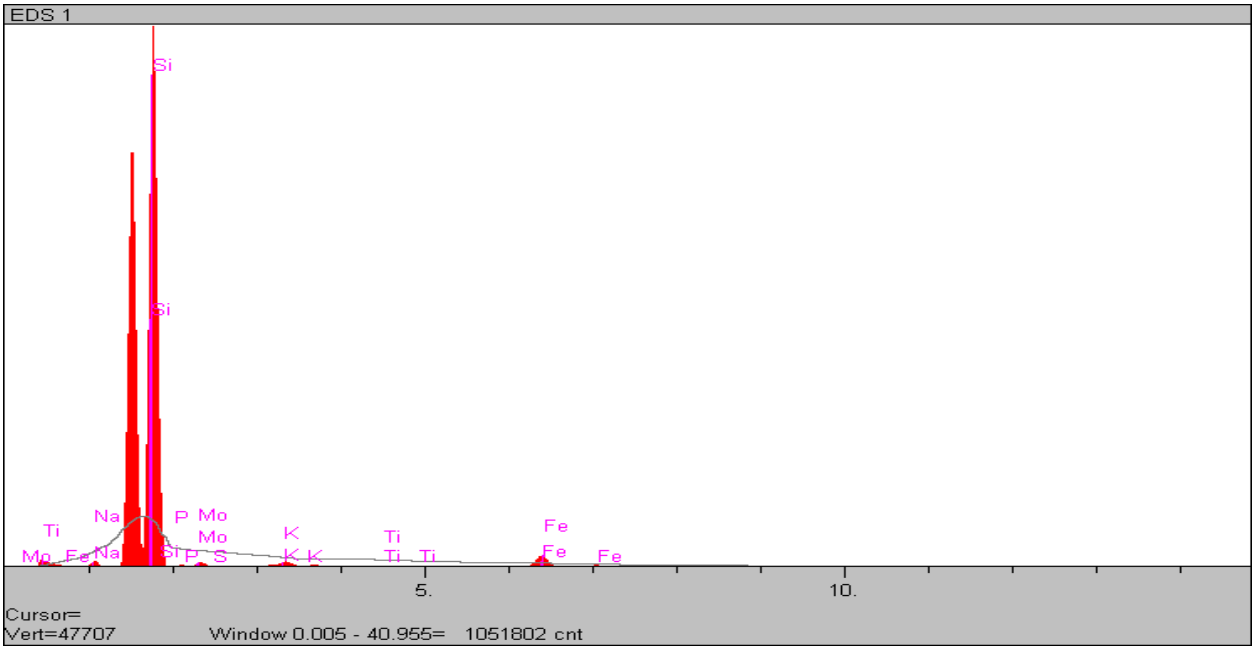

XRD Microanalysis 1 Sample #12

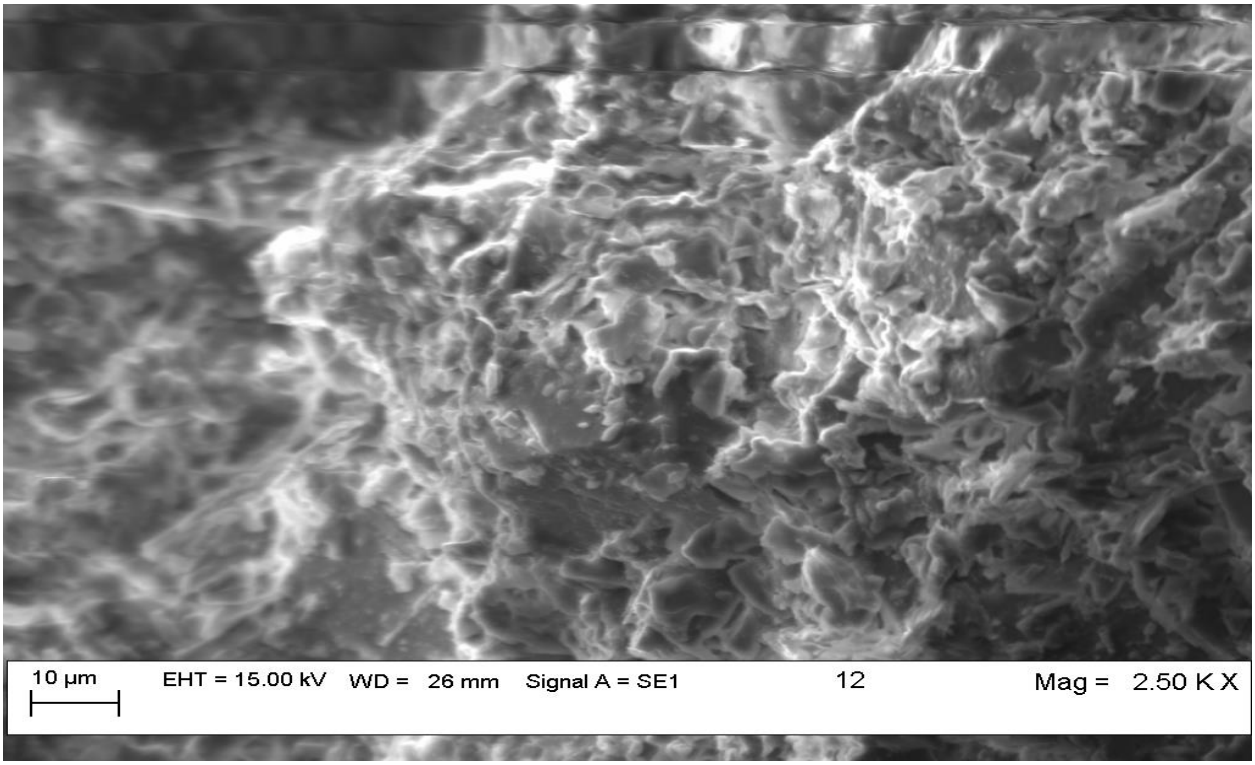

XRD Image 1 Sample # 12 – 01

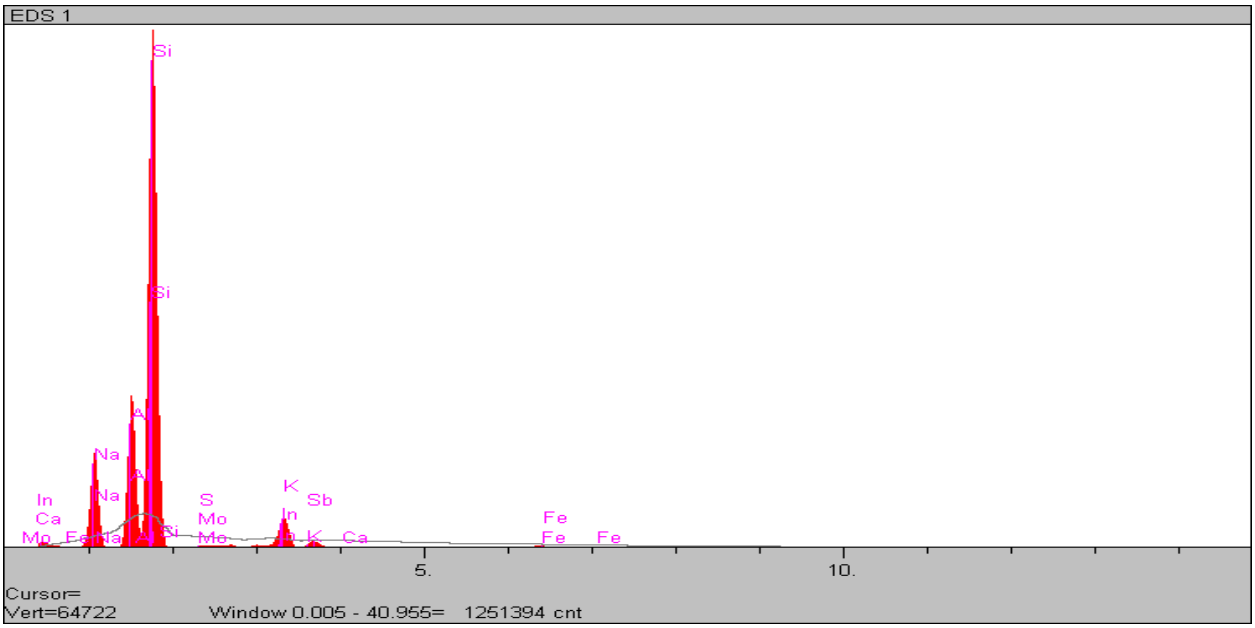

XRD Microanalysis 2 Sample # 16 – 01

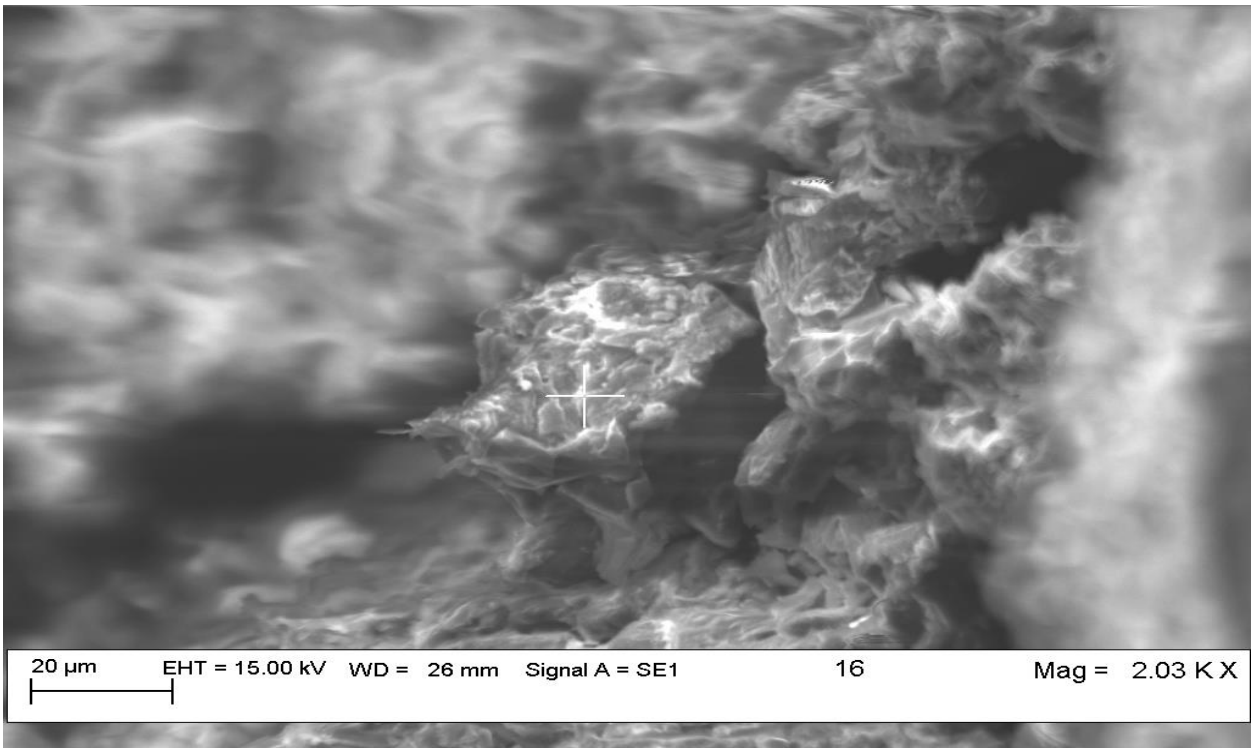

XRD Image 2 Sample 16 – 01

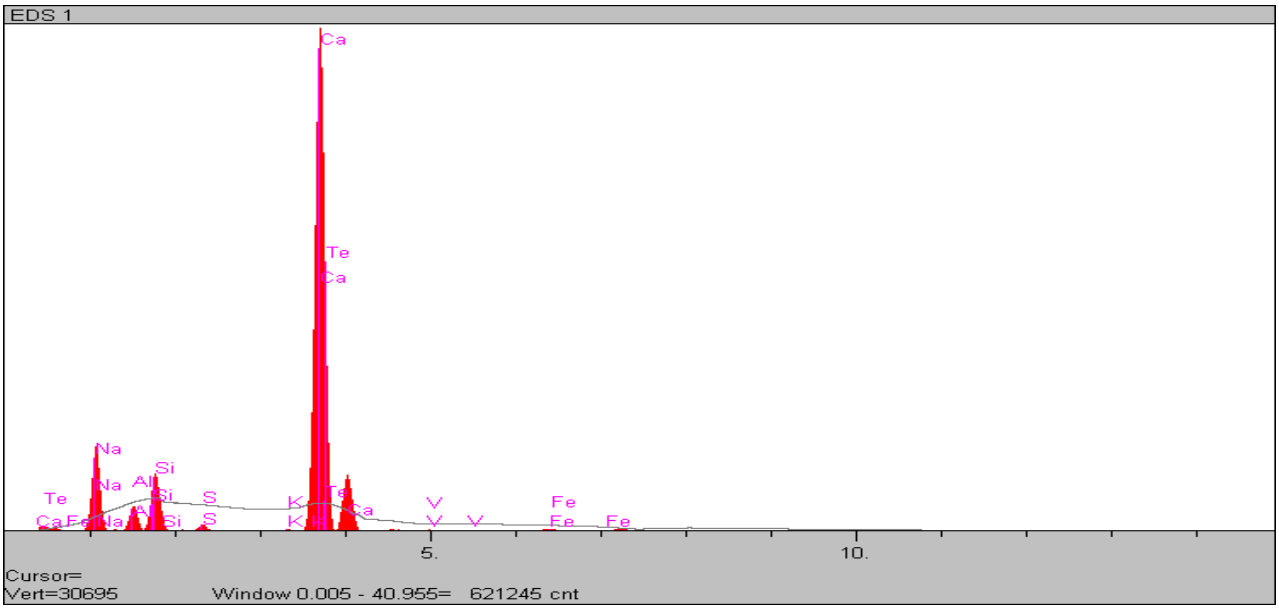

XRD Microanalysis 3 Sample # 16 – 03

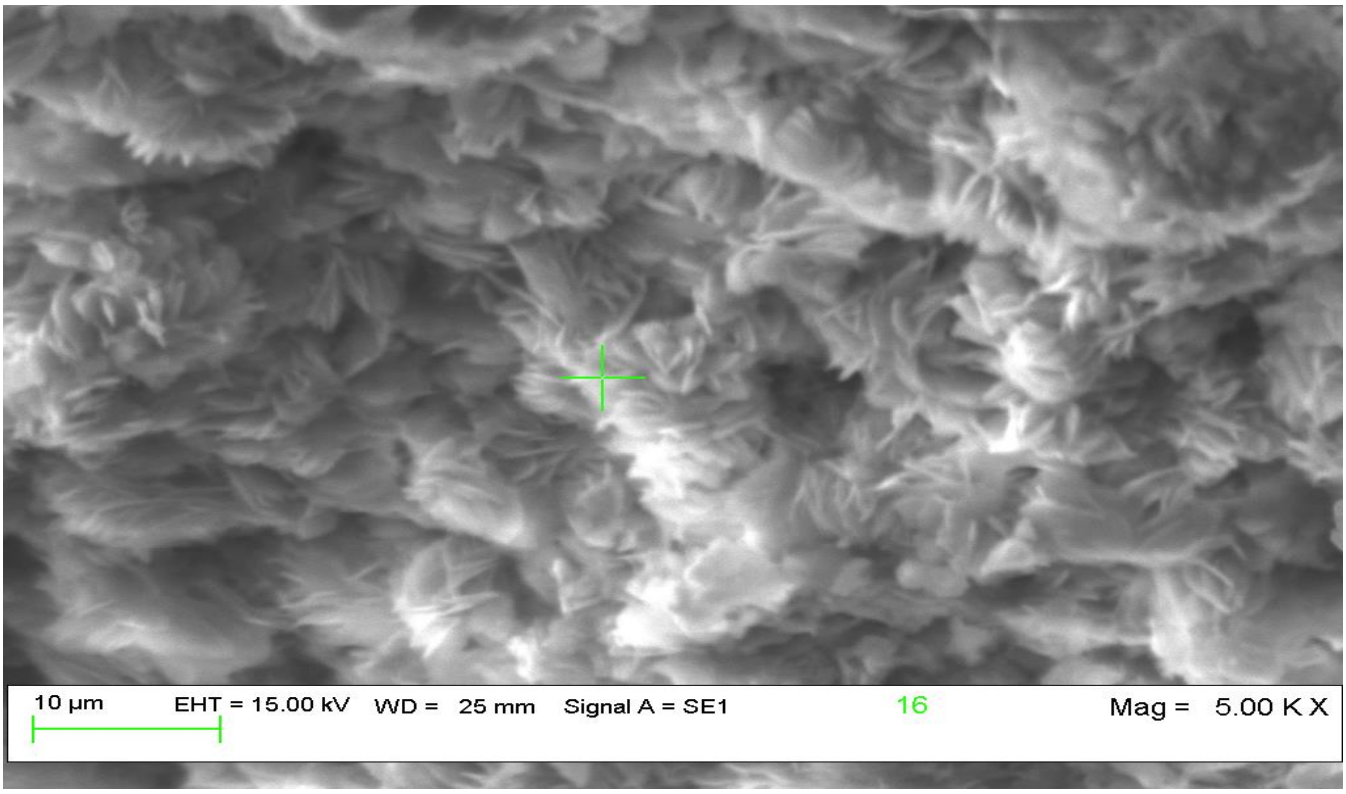

XRD Image 3 Sample # 16 – 03

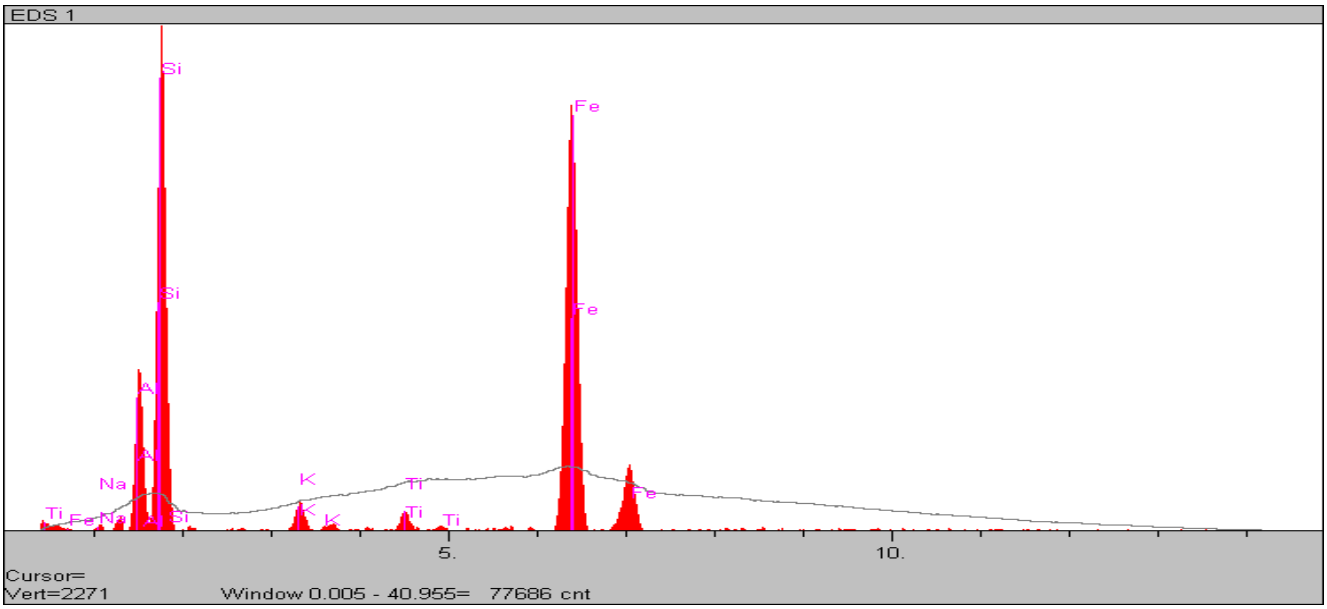

XRD Microanalysis 4 Sample # 17

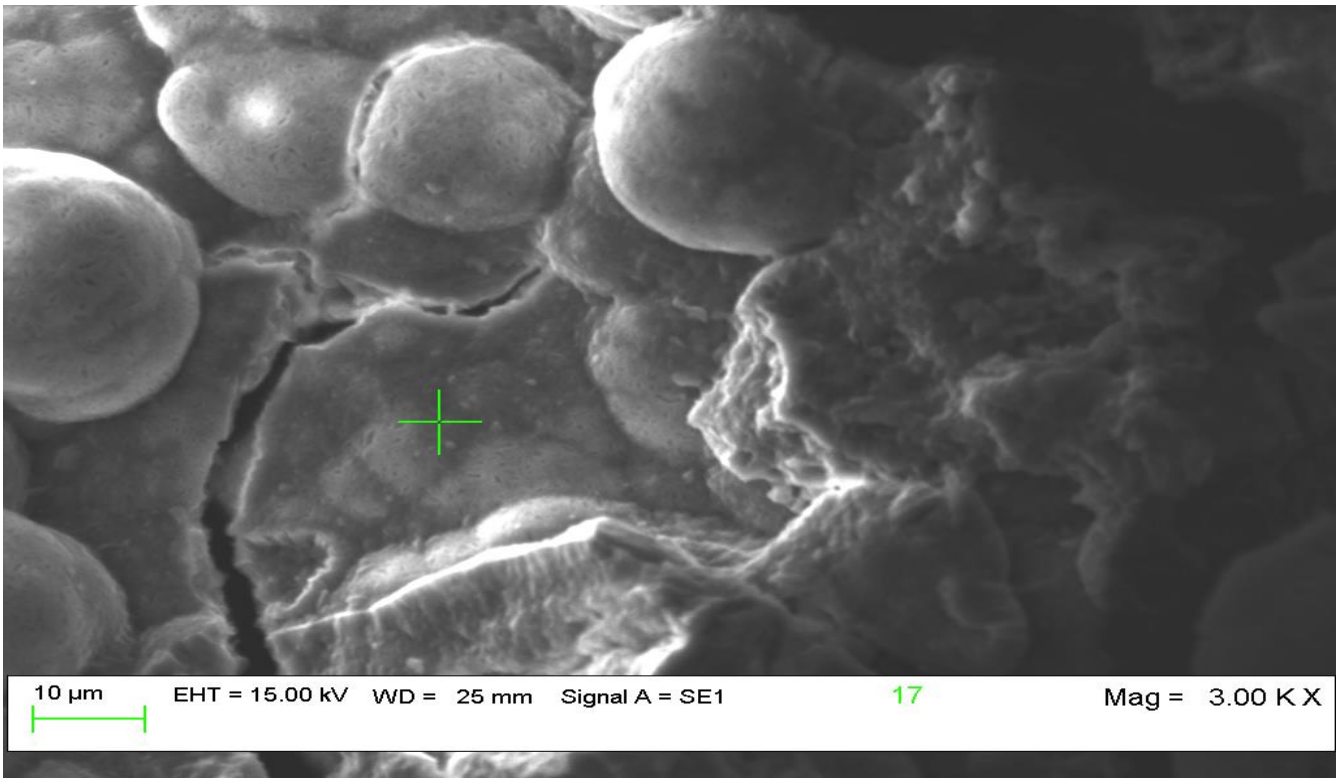

XRD Image 4 Sample # 17 – 01

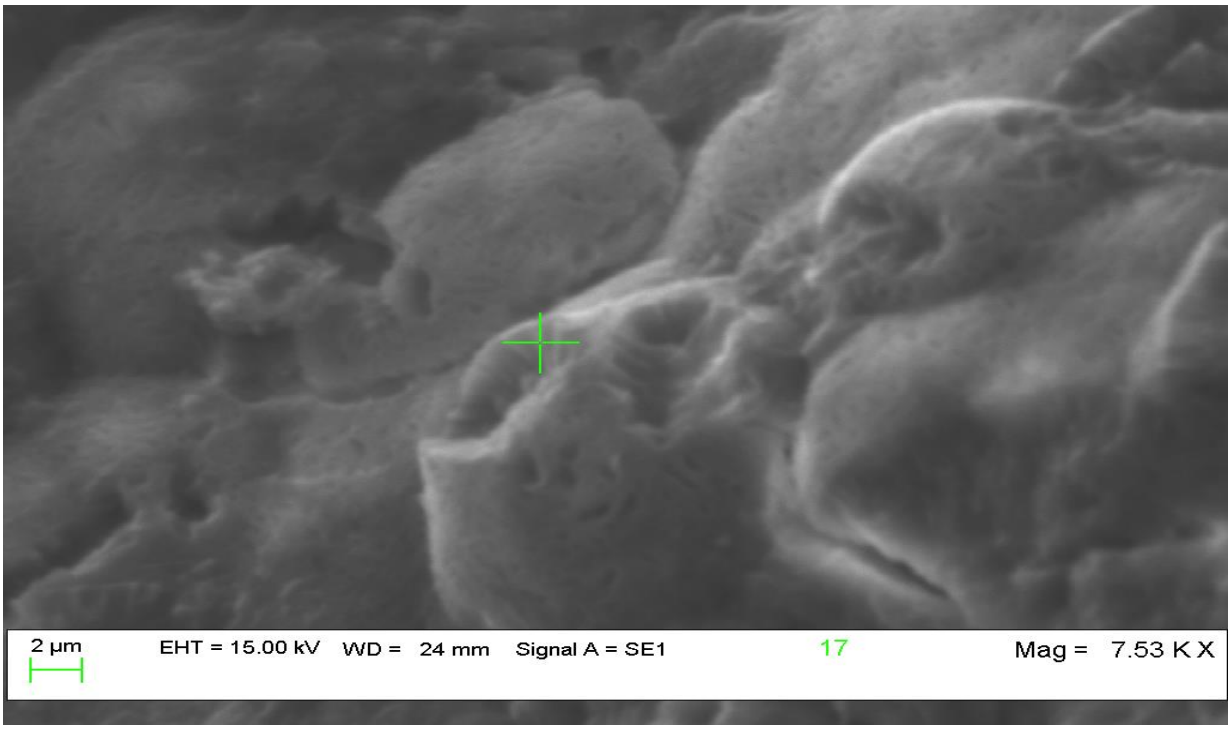

XRD Image 5 Sample # 17 – 02

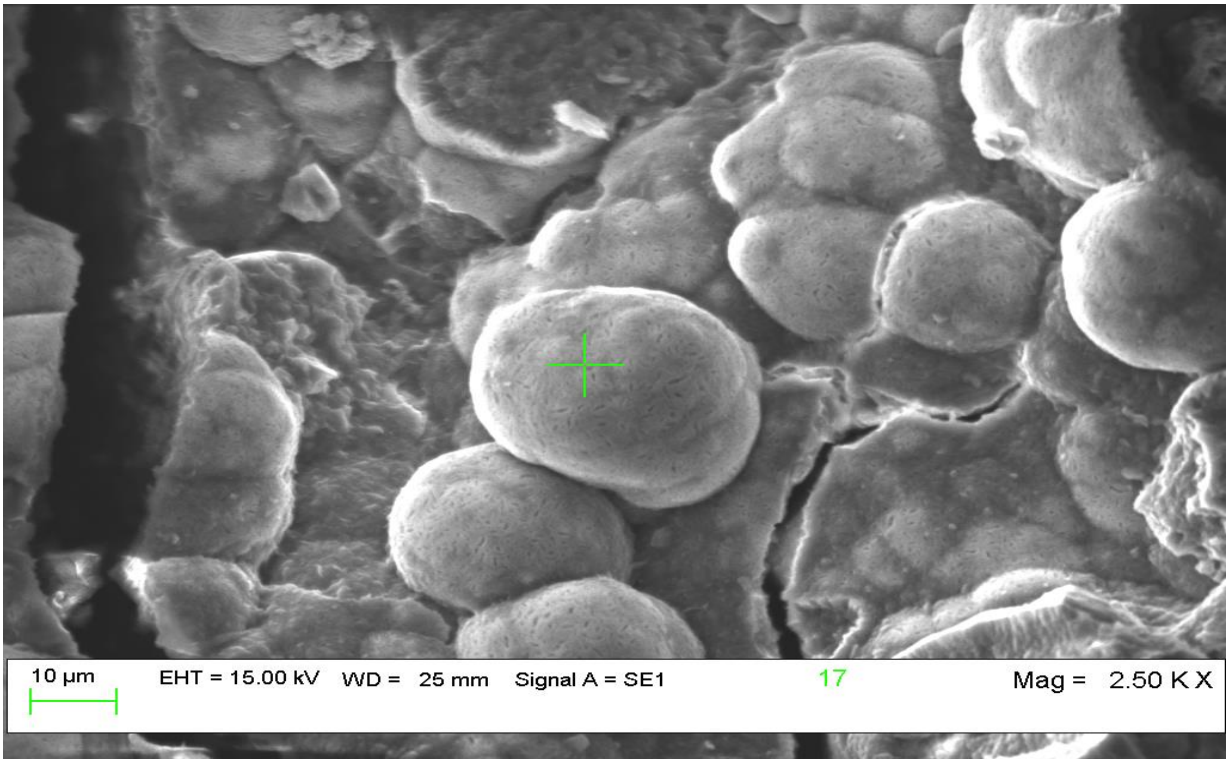

XRD Image 6 Sample # 17 – 03